Structural and Aerodynamic Mistuning in Blade Aeroelasticity

Hien Minh Phan

Linacre College

University of Oxford

A thesis submitted for the degree of

Doctor of Philosophy

Hilary 2022

Acknowledgements

My DPhil work essentially investigates the interaction between the fluid flow and the solid structures for turbomachinery applications. Thus, the term "interaction" has always occupied my thoughts and has been a guidance for my research directions. I quickly realised that "interaction" can be broadly interpreted. It is not only a fluid-structure or multi-component interaction but also the academia-industry interaction and people-to-people interaction. I am thankful for this DPhil journey, where I have had multiple opportunities to exercise those interactions.

First and foremost, I would like to thank my supervisor - Professor Li He for giving me the opportunity to pursue this doctoral degree and write this dissertation. His views and advices have opened new doors for me towards a more successful (research) career. It is difficult to express by words how much he has influenced and shaped me of today. He has guided me on writing more comprehensible research papers. He has helped me to improve the effective communication and the articulation of verbal discussion. I have built up the confidence in presenting my works to a large number of audiences and exchanging ideas with international colleagues. All these changes have made me a better person. He does not only influence me on the technical perspective but also on various aspects of life. Our weekly meetings have typically been filled with discussions on life in general. For me, he is not only an academic supervisor but also a senior friend and a role model.

I would like to send the special thanks to my loving family: my late father Phan Hoai Bao, my mother Vu Thi Thuan, my brothers Phan Minh Thien Nhan and Phan Minh Hieu Nhan. Although my late father could not have the opportunity to see I become Dr. Phan, his unconditional love in my memories has supported me going through and resiling from the hardship. Each of my family member has their own ways to support me on this journey and they are very much the reason that makes me determine to stay on this path.

I would like to send my gratitudes to all people in the EPSRC Centre for Doctoral Training in Gas Turbine Aerodynamics, the Whittle Lab, and the Osney Lab. They have given me a strong foundation in turbomachinery and nurtured a strong curiosity and commitment to the vast turbomachinery research problems. I have learned a lot from my friends. It is always amusing to talk to these talented and interesting people about both academic and life problems: Mai To, Penghao Duan, Chen Chen, Tom Hickling, Aravin Dass Naidu, Hassan Saad Ifti, and many more.

I also appreciate the opportunities to interact with Siemens people: Dr. Roger Wells, Dr. Yansheng Li, and Dr. Senthil Krishnababu. I have learned a lot from their rich industrial experiences, which definitely has contributed to a better practicality of the research directions.

I would like to thank the support staffs that made my DPhil journey smoother: Alexandria Weaving in the administration team and Craig Parsons in the IT team.

I am grateful for the travel awards granted by ASME, University of Florence, and Beihang University. These travel awards have enabled me to attend the summer schools and conferences worldwide, talk to many interesting people, expose to interesting cultural experiences, and open my horizon.

I would like to acknowledge the support from the Chair of Computational Aerothermal Engineering Bursary. Most of simulations presented in this thesis were run on the HPC facilities of the lab (REX cluster) and the university (ARC cluster - http://dx.doi.org/10.5281-/zenodo.22558).

Abstract

The blade-to-blade variations, also known as mistuning, are inevitably present in the bladerow due to manufacturing tolerances, assemble processes, as well as wear and tear. Mistuning has been known to significantly affect the aeroelastic performance of a bladerow. Mistuning can be categorised into two main groups: structural mistuning and aerodynamic mistuning. While the structural mistuning has been studied extensively in the past, the aerodynamic mistuning has recently attracted more attention. There is a lack of clear and systematic understanding of physical behaviour and mechanisms of a mistuned bladerow, particularly in the context of the aerodynamic mistuning versus the structural mistuning. In addition, most mistuning studies in the past has used some types of reduce-order modelling techniques, which can have certain loss of accuracy. In this thesis, the high-fidelity fully-coupled fluid-structure interaction simulation method is adopted to investigate the fundamental vibration mechanism of the mistuned bladerows.

The results show that the standalone structural mistuning always has a stabilising impact on the flutter stability. The standalone aerodynamic mistuning has a non-monotonic trend on the flutter stability, i.e. it has a stabilising effect with a small amount of mistuning but a destabilising effect with a large amount of mistuning. An aero-mistuning induced flutter phenomena has been observed. It has been shown that an aerodynamic mistuning can lead to flutter at a condition where the tuned cascade remains stable. The concurrent structural-aerodynamic mistuning shows a distinctive nonlinear interaction between the two types of mistuning. Particularly, the flutter stability of the unstable aero-mistuned cascade maybe improved with a small additional structural mistuning, but degraded remarkably with a larger value of additional structural mistuning. For the forced response problems, both the structural mistuning and the aerodynamic mistuning induce significant vibration amplitude amplification compared to the tuned bladerow. The concurrent structural-aerodnamic mistuning shows remarkable interaction effects on the response amplitudes, particularly with different circumferential phasing between the two types of mistuning.

Based on the fundamental understanding of the mistuned vibration mechanisms gained from high-fidelity fully-coupled simulations, an innovative design concept has been proposed. The newly introduced design variable is denoted as the mistuning

circumferential phasing. The simulation results suggest that the new design concept has a potential to leverage the bladerow's aeroelastic performance. The new mistuning design concept opens a new design space particularly in conjunction with certain intentional mistuning. The findings may also have some bearing in helping understand the inconclusiveness of previous observations related to the impact of mistuning, and thus help better understand this seemingly complex topic.

Although the fully-coupled fluid-structure simulation method is certainly useful for the design and analysis of a mistuned bladerow, it is not often used due to expensive computational resource requirements. In this thesis, a new simulation methodology is proposed that has the potential to reduce the simulation time by at least an order of magnitude while retaining the accuracy comparable to the high-fidelity simulations. The newly developed method is built upon the bases of the multi-scale approach and the influence coefficient method. This is the first time the theoretical framework of the multi-scale method has been extended to accommodate unsteady flow and grid deformation effects. The applications of the multi-scale method on aeroelasticity problems are also the first of its kind. On the other hand, the new extended formulation as well as the novel application of the influence coefficient method has also been made. Combining with the multi-scale approach, it provides an efficient way to pre-compute a limited high-fidelity simulations and later reconstruct the necessary source terms for a large amount of mistuned configurations. The new simulation methodology has been tested for various aeroelasticity problems of interest. Starting from the steady and the unsteady flow simulations of uncoupled configurations, it has gradually built up to the fully-coupled fluid-structure interaction cases.

Contents

List of Figures

List of Tables

Nomenclature

Abbreviations

CFD . . . . . . computational fluid dynamics

DOF . . . . . . degree-of-freedom

FFT . . . . . . Fast Fourier transform

FSI . . . . fluid-structure interaction

IBPA . . . . . interblade phase angle

ICM . . . . . . influence coefficient method

ND . . . . nodal diameter

PS . . . . pressure surface

PV . . . . passage vortex

SS . . . . suction surface

TLV . . . . . . tip leakage vortex

TWM . . . . . travelling wave mode (tuned)

Symbols . . . .

ΔV . . . . mesh cell volume

β_1 . . . . inlet flow angle

θ . . . . phase angle, also mistuning circumferential phasing angle

μ . . . . blade mass ratio

ξ . . . . aerodynamic damping

σ . . . . interblade phase angle, IBPA

ψ . . . . time-averaged phase angle

Am . . . . amplitude

C . . . . blade chord

C_p . . . . pressure coefficient

f . . . . nominal frequency, also modal excitation forcing

h . . . . blade height

I . . . . blade inertia

k . . . . reduced frequency

m . . . . blade index

N_θ . . . . number of spatial harmonics

N_f . . . . number of harmonics

q . . . . modal vibration response

U . . . . conservative flow variable

UST . . . . . . unsteady source term

$\overline{UST}$ . . . . . . time-averaged component of the unsteady source term

UST' . . . . . . fluctuating component of the unsteady source term

Re . . . . Reynolds number

S . . . . source term

V_{ref} . . . . exit isentropic flow velocity

W_{aero} . . . . . . aerodynamic work

Y_p . . . . total pressure loss coefficient

Subscripts . .

c . . . . coarse

f . . . . fine

$f \to c$ . . . . . . fine projected to coarse

l . . . . local

n . . . . natural

Superscripts .

$\hat{}$ . . . . amplitude

$\tilde{}$ . . . . Hilbert transform

1 Introduction

Contents

1.1 Background and Motivation

Gas turbine is an essential part of an aircraft and a power station. The demand for air transport and power has increased significantly during the last decade and has gradually recovered since the COVID pandemic. There has been already a development race towards more efficient, more environmental-friendly machines through technological advances from all components of the gas turbine and its architecture. Notably, the overall cycle efficiency of a gas turbine can be improved by two means: increasing the turbine entry temperature (TET) and increasing the overall pressure ratio (OPR).

Whilst trying to increase TET and OPR, the weight and minimum lifespan of an engine are also restricted to maintain the benefits of an improvement. The increases in TET and OPR have been achieved by technological advances in cooling methods, high heat-resistant material, and manufacturing techniques (single crystal blade). The improvement in OPR is also due to other modifications such as the increase in by-pass ratio and the use of geared turbo fans. Such modifications has led to the following changes in the gas turbine architecture:

- Fewer compressor stages and lower blade counts lead to more heavily loaded blades.
- Reduced axial distance between bladerows leads to increasing interactions among bladerows and less room for wake mixing.
- Highly three-dimensional blade design including sweeping and leaning, which aims to form a more efficient design in terms of aerodynamics. However, they have consequences on the structural response.
- Hollow, thinner, lighter components and the use of composite material have benefits of reducing weight. However, they will alter the structural response.
- Introduction of blisks (integrally bladed disk) and blings (integrally bladed ring). This modification reduces weight by eliminating inter-locked structures between blades and disks. However, it also removes the natural damping sources among the components.

Apart from the current state-of-the-art gas turbine technology, novel and market disruptive future propulsion systems are also sought after. The environmental commitment of the United Kingdom is to reduce carbon emission by 78% by 2035 and reach net zero by 2050. In order to reach such an ambitious target, the UK engineering industry has to play a pivotal role. There has been initiatives from within the UK to design a hybrid or fully-electric aircraft. Due to the limited power density of batteries compared to fossil fuels, the electric propulsion system needs to be much lighter and more compact compared to current propulsion architectures.

All of those aforementioned technical modifications in both current and future technologies results into a higher susceptibility to aeroelastic vibrations due to stronger fluid-structure interaction effects. This in turn would endanger the safety and robustness of the system, particularly important for a passenger-carrying aircraft.

The aeroelastic vulnerability is exacerbated by the inevitable presence of the blade-to-blade variations, also known as mistuning. The variations stem from the manufacturing tolerances, assemble processes, as well as wear and tear. Mistuning has been known to significantly affect the aeroelastic performance of a bladerow. Mistuning can be categorised into two main groups: structural mistuning and aerodynamic mistuning. The former involves the change in structural parameters such as the blade mass and the blade stiffness. The latter involves variations in the blade stagger angle, the leading and trailing edge shape, the blade thickness, and the blade camber. While the structural mistuning has been studied extensively in the past, the aerodynamic mistuning has recently attracted more attention. There is a lack of clear and systematic understanding of physical behaviour and mechanisms of a mistuned bladerow, particularly in the context of the aerodynamic mistuning versus the structural mistuning. In addition, most mistuning studies in the past has used some types of reduce-order modelling techniques, which can have certain loss of accuracy.

Therefore, it is clear that the routine aeroelastic design and analysis of a bladerow is essential for the development of an environmental friendly and robust gas turbine, particularly under the stochastic effects of mistuning. If the vibration mechanisms of a mistuned bladerow is better understood, these inherent variations can be exploited for an aeroelastic performance gain. The simulation tools should be high-fidelity to reflect the required accuracy with an increasing coupling level of the components.

1.2 Research Questions and Scope

The present thesis aims to improve understanding of the physical vibration mechanisms of mistuned bladerows and thus generate design and/or control methods for a better aeroelastic performance. In order to achieve the research objectives, the following research questions need to be properly addressed:

i **What are the fundamental vibration mechanisms and aeroelastic effects of mistuning, particularly in the context of the structural mistuning versus the aerodynamic mistuning?** Since most previous works in mistuning used some reduce-order modelling techniques, it is important to establish the fundamental understanding of the mistuning problem using high-fidelity fully-coupled simulations. Both the structural mistuning and the aerodynamic mistuning have to be investigated and compared to each other.

ii **How may the structural mistuning and the aerodynamic mistuning interact? Can we take advantage of this interaction for an aeroelastic performance gain using an intentional mistuning design?** The concurrent structural-aerodynamic mistuned bladerows need to be investigated to analyse the interaction effects among the two. If the interaction effects are significant, it is possible that the concurrent mistuning concept can be utilised for leveraging aeroelastic performance.

iii **Is it possible to run the aeroelastic analyses with a reduced computational cost while maintaining a comparable accuracy compared to the direct high-fidelity simulations?** Aeroelastic analyses especially the fully-coupled methods are computationally expensive. The emerging multi-scale modelling methodology will be extended and applied to aeroelastic applications. The accuracy and efficiency of the newly developed method needs to be demonstrated against direct high-fidelity solutions.

1.3 Thesis Overview

The main body of the thesis consists of the following chapters:

In Chapter 2, past literatures related to the research questions are reviewed. In specific, the current state-of-the-art aeroelasticity modelling approaches are described. The effects of mistuning, its modelling approaches, and its intentional design concept are also discussed.

In Chapter 3, the simulation methodologies adopted in the present thesis are described in more details. The Computational Fluid Dynamics (CFD) and Fluid-Structure Interaction (FSI) modelling procedures using the solver ANSYS CFX are reported. The basic of the multi-scale technique and the influence coefficient method are also described. These descriptions serve as the baseline for further extensions in the later Chapters.

In Chapter 4, the baseline test case configuration is described. Steady and unsteady flow simulation results are validated against the available experimental data, with the particular attention on the effects of the laminar separation bubble and the tip clearance. In the second part, the validity and applicability of the influence coefficient method in a linear cascade setup are examined.

In Chapter 5, the fundamental vibration characteristics of a mistuned cascade will be investigated using the fully-coupled fluid-structure simulation method. The aeroelastic effects of mistuning will be also studied. The characteristics and effects of the structural mistuning and the aerodynamic mistuning are compared to each other.

In Chapter 6, the interactions between the structural mistuning and the aerodynamic mistuning are further investigated. A new design concept is proposed to leverage the blade's aeroelastic performance. The superposability of the two types of mistuning is examined to study the effectiveness of the simple linear superposition method in early design stages.

In Chapter 7, the theoretical framework of the multi-scale method is extended to applications with unsteady flow and grid deformation for the first time. The newly developed method is applied to the modelling of an arbitrarily mis-staggered bladerow subject to both clean and distorted inflow conditions. Both the accuracy and the efficiency of the multi-scale method are compared against direct high-fidelity solutions.

In Chapter 8, the implementation of the multi-scale method is extended to the fully-coupled fluid-struture interaction simulation method. The newly developed method is applied to the forced response modelling of a fully-coupled mistuned bladerow under an inlet distortion. Both the accuracy and the efficiency of the multi-scale method are compared against direct high-fidelity solutions.

In Chapter 9, conclusions drawn from the present research are summarised. Some possible suggestions for future works are also discussed.

1.4 List of Publications

In this section, the journal and conference publications that are directly related to the results presented in the current DPhil thesis are listed below. All of these publications have been written whilst holding the DPhil candidate status at the University of Oxford.

The following papers form part of Chapter 4.

- **H. M. Phan & L. He, 2018. Validation Study of 3D Oscillating Compressor Cascade. ISUAAAT15 conference paper [Phan and He, 2018].**

- **H. M. Phan & L. He, 2019. Validation Studies of Linear Oscillating Compressor Cascade and Use of Influence Coefficient Method. ASME Turbo Expo 2019 conference paper [Phan and He, 2019].**

- **H. M. Phan & L. He, 2019. Validation Studies of Linear Oscillating Compressor Cascade and Use of Influence Coefficient Method. ASME Journal of Turbomachinery paper [Phan and He, 2020b].**

The following papers form part of Chapter 5.

- **H. M. Phan & L. He, 2021. Investigation of Mistuned Oscillating Cascade Using Fully-Coupled Method. ASME Turbo Expo 2020 conference paper [Phan and He, 2021c].**

- **H. M. Phan & L. He, 2021. Analysis Of Structurally and Aerodynamically Mistuned Oscillating Bladerow Using Fully-Coupled Method. GPPS Xian 2021 conference paper [Phan and He, 2021a].**

- **H. M. Phan & L. He, 2021. Investigation of Structurally and Aerodynamically Mistuned Oscillating Cascade Using Fully Coupled Method. ASME Journal of Engineering for Gas Turbines and Power paper [Phan and He, 2022]**.

The following papers form part of Chapter 6.

- **H. M. Phan & L. He. Phasing of Structural and Aerodynamic Mistuning for Leveraging Aeroelastic Performance. Manuscript submitted to ASME Turbo Expo 2022 conference**.

The following papers form part of Chapter 7.

- **H. M. Phan & L. He, 2020. Efficient Steady and Unsteady Flow Modeling for Arbitrarily Mis-Staggered Bladerow Under Influence of Inlet Distortion. ASME Turbo Expo 2020 conference paper [Phan and He, 2020a]**.
- **H. M. Phan & L. He, 2021. Efficient Steady and Unsteady Flow Modeling for Arbitrarily Mis-Staggered Bladerow Under Influence of Inlet Distortion. ASME Journal of Engineering for Gas Turbines and Power paper [Phan and He, 2021b]**.

The following papers form part of Chapter 8.

- **H. M. Phan & L. He, 2021. Efficient Modeling of Mistuned Blade Aeroelasticity Using Fully-Coupled Two-Scale Method. Manuscript submitted to Journal of Fluids and Structures**.

2
Literature Review

Contents

This chapter summarises past researches related to the numerical methodology for blade aeroelasticity prediction and the mistuning effects. In the first section, current state-of-the-art aeroelasticity simulation methods are briefly described. In the second section, the aeroelastic effects of mistuning are discussed. Finally, the third section presents a non-exhaustive list of available numerical methods for mistuning study.

2.1 Numerical Modelling of Blade Aeroelasticity

The challenge to design an efficient and reliable gas turbine has been continually tackled by both the aviation and power generation industry. The development is driven not only by market demand for a low operating cost machine but also by increasingly strict regulations to reduce exhaust emissions and noise pollution. While doing so, gas turbine manufacturers are also under a pressure to launch their latest technology with a fairly reasonable capital expenditure projection as well as the development time. In the last few decades, Computational Fluid Dynamics (CFD) simulation tools have been proven to be useful in the design and analysis stage, leading to a much shorter product-to-market cycle and a much cheaper development cost compared to that in the early days of the industry. Among the blade aeroelasticity phenomena, flutter and forced response are the most important characteristic for a turbomachinery blading design.

2.1.1 Flutter

Flutter is a self-excited vibration phenomenon that endangers the structural integrity and leads to failures of turbomachinery blades. Starting from an initial small vibration amplitude, the energy exchange between the blade and the surrounding fluid flow amplifies the vibration amplitude with time. Depending on the origin of the aeroelastic stabilities, flutter can be categorised into different groups as shown in Figure 2.1:

i Region I - subsonic/transonic stall flutter: this type of flutter is close to the stall line. It involves flow separation on the blade suction surface.

ii Region Ia - system mode instability: this type of instability seems to be associated with the upper end of the region I. Although the blade loading is high, flutter may not involve flow separation as an essential part of the mechanism. The appearance of oscillating shocks may help explain the negative aerodynamic damping.

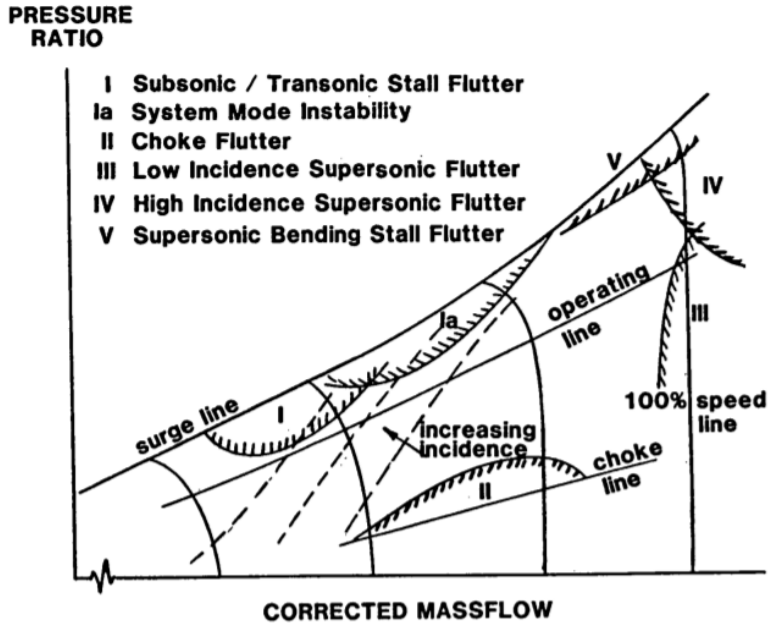

Figure 2.1: Illustration of different types of flutter [Sisto, 1987].

iii Region II - choke flutter: this type of flutter is near the choke line. It is characterised by the occurrence of choked flow, unstable separations and shock waves.

iv Region III - supersonic unstalled flutter: this type of flutter appears in the supersonic flow region and usually as a torsional mode. It is characterised by low back pressure, hence it is also known as supersonic started flutter at low back pressure.

v Region IV - high-incidence supersonic flutter: this type of flutter is similar to region III although the flow incidence angle is usually high.

vi Region V - supersonic bending stall flutter: this type of flutter is usually accompanied by a strong in-passage shockwave and a boundary layer separation due to a bending mode vibration. It usually appears as the back pressure increases so it is also known as supersonic flutter started at high back pressure. As a result, shockwaves will form near the leading edge.

Accurate and efficient predictions of blade flutter is crucial in the engine development and the certification campaign. Modern numerical modelling of turbomachinery flutter predictions are built upon the two most important modelling bases, namely the monochromatic travelling wave concept [Lane, 1956] and the energy method [Carta, 1967]. The first assumption dictates that the blades in the same row would vibrate at a same frequency and a constant interblade phase angle. The second assumption simplifies the flutter prediction process into a decoupled manner such that the aerodynamic forces are assumed to have a negligible effect on the structural responses. The in-vacuo mode shape and frequency can be obtained separately and used as an input to the CFD codes. The energy method adopts the concept of aerodynamic damping to determine the flutter susceptibility. When the aerodynamic damping is positive, the blade vibration energy dissipates to the surrounding medium and the blade would be stable. Vice versa, when the aerodynamic damping is negative, the blade absorbs energy from the surrounding medium and the blade would be unstable. Since its introduction, the energy method has become the most common method for turbomachinery flutter predictions thanks to its simplicity. Its associated spanwise integration capability is also compatible with the section-by-section design procedures [Marshall and Imregun, 1996], although direct three-dimensional (3D) simulations with energy method have become popular.

In the energy method, the bladerow will be oscillated at a pre-defined mode shape, frequency, and interblade phase angle to calculate the aerodynamic damping. Since there are many possibles interblade phase angles depending on the number of blades in the row, these modelling procedures have to repeat several times. The most straightforward modelling domain is the full-annulus or sector of the bladerow that contains a repeating vibration period. Thus, the standard periodicity boundary conditions can be applied to the two outermost interfaces. In a few scenarios, the periodicity conditions can stretch for several blade pitches (i.e. the flow pattern repeats itself after an integer number of blade passages, dividing the whole annulus into what is known as nodal diameter). For some extreme cases, the pattern can have a wavelength of the whole circumference, which hinders the effectiveness of the classical direct periodicity simulations. In these cases, the current state-of-the-art numerical methodology is to adopt a phase-shifted periodicity. Erdos et al. [1977] pioneered the direct store method, which has been superseded by more advanced approaches such as time-inclination [Giles, 1990], shape-correction [L. He, 1990], and chorochronic periodicity [Gerolymos et al., 2002]. On the basis of the aforementioned approaches, it is now rather common to perform efficient unsteady flow modelling as a routine task using advanced methods such as Non-Linear Harmonic [L. He and Ning, 1998] and Harmonic Balance [Hall et al., 2002]. Extensions and applications of those methods are still an on-going topic of research [Vilmin et al., 2006; McMullen and Jameson, 2006; Frey et al., 2014; Crespo et al., 2016]. A review of the use and history of Fourier method for turbomachinery applications can be found in Ref. [L. He, 2010].

2.1.2 Forced Response

The turbomachinery bladerow is subject to aerodynamic disturbances from either upstream (e.g. wake, inlet distortion) or downstream bladerows (e.g. potential field). These disturbances will have a set of characteristic frequencies (i.e. engine order) that is related to the shaft rotational speed. When the blade passing frequency coincides with the system eigen-frequency, resonant vibration takes place, which is referred to as the forced response problems. For forced response, vibration amplitude is bounded unlike in the flutter case so sudden failures are not possible. However, the vibration induces extra dynamic stresses on the blade, which adds on top of the existing static stress (due to centrifugal force, steady aerodynamic and thermal load). The blade life time is therefore reduced. If the blade's structural integrity is not inspected and maintained properly, early High Cycle Fatigue (HCF) failures can occur. Unfortunately, avoidance of the forced response vibration is almost impossible. Possible excitation sources will exist across the gas turbine working range. To assess the potentially dangerous resonant crossing operating point, one can use the Campbell diagram as shown in Figure 2.2. The horizontal curves are the system's eigen- frequencies with respect to the rotational speed, whereas the inclined lines are the engine order (EO) excitations. The intersections between the eigen-frequency curves and the engine order lines are the resonant operating points.

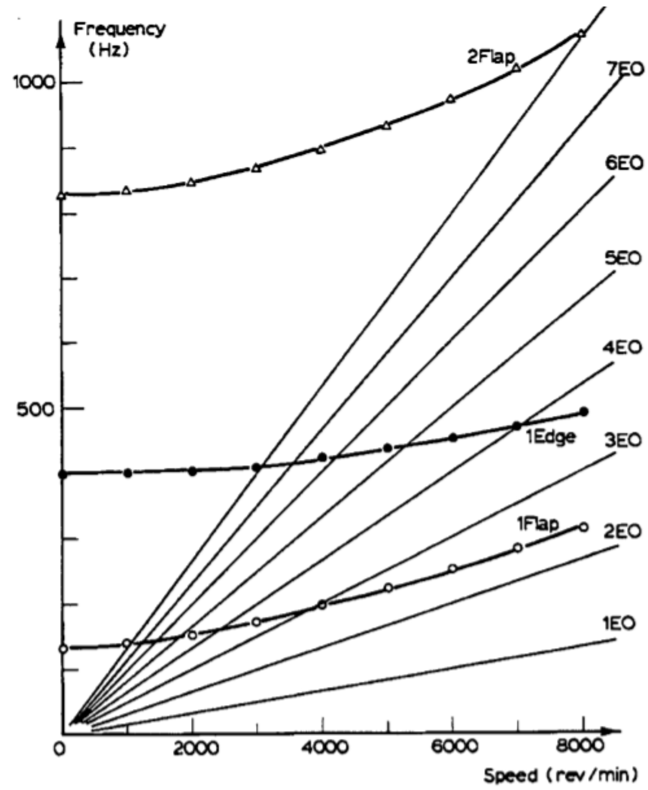

Figure 2.2: Example of the Campbell diagram [Ewins and Henry, 1987].

Since the forced response vibration is unavoidable, it is important to calculate the response vibration amplitudes and thus dynamic stresses for risk management purposes. Modern numerical modelling of turbomachinery forced response relies on the superposition method of the aerodynamic damping force (aero-damping) and the aerodynamic excitation force (aero-forcing) [e.g. Schmitt et al., 2003; Tran et al., 2003]. These two contribution effects can be calculated separately. Under the uncoupled assumption, the aero-damping is only dependent on the blade vibration amplitude, while the aero-forcing is independent of the blade vibration amplitude. The procedures to calculate the aerodynamic damping is similar to what has been described earlier for the flutter prediction methods.

The aero-forcing modelling can be carried out with a stationary bladerow subject to a periodic excitation. Recalling the tuned bladerow assumption where the vibration frequency and interblade phase angle is uniquely defined, the phase-shifted simulation methodology can also be adopted in this kind of calculation. Some examples of these Fourier-based methods in the rotor/stator interaction studies are Sicot et al. [2011], Burgos et al. [2011], Chen et al. [2001], Wang and Huang [2017], Stapelfeldt and Di Mare [2015]. On the other hand, geometry scaling technique is a more straightforward method to apply considering the standard periodicity condition although the effects of aerodynamic dissimilarity are still under investigation [Mayorca et al., 2011; Buchwald et al., 2019]. A similar approach is to scale the rotor-stator interface rather than the geometry [Galpin et al., 1995], known as the Profile Transformation (PT) method. The other method is known as the Time Transformation method, which is based on the time-inclination method [Giles, 1988]. Time is transformed such that the pitchwise boundaries are periodic in the transformed time coordinate. Comparison and application of these methods in the context of a commercial solver can be found in Ref. [Connell et al., 2011; Connell et al., 2012; Biesinger et al., 2010];

2.1.3 Fluid-Structure Interaction

The interaction between solid structures and the surrounding fluid flow, known as the fluid-structure interaction (FSI) problem, is of interest in many applications. For turbomachinery applications, the uncoupled methods have been predominantly used with great success thanks to the excellent stiffness-to-weight ratio of the titanium/nickel-based blades. However, modern gas turbines have the tendency to make more use of lightweight composite materials and innovative propulsion architectures [Brandstetter et al., 2019; Rendu et al., 2020; Provenza et al., 2019; S. C. Stapelfeldt et al., 2016], which hinders the effectiveness of the uncoupled methods. Sadeghi and Liu [2005] demonstrated a discrepancy of the predicted flutter boundary between the uncoupled and the fully-coupled methods for a linear cascade of uncambered biconvex airfoils. Carstens and Belz [2001] and Carstens et al. [2003] reported a nonlinear flutter phenomena at transonic flow condition using the fully-coupled method. Chahine et al. [2019] investigated flutter of the transonic fan rotor acorss a range of mass ratio and stiffness. They concluded that the decoupled and fully-coupled methods are in good agreement across a large range of structural conditions. Neverthelss, the prediction discrepancy can be as high as 27.3% between the two methods at a combined low mass ratio and low stiffness condition. As a result, the use of fully-coupled methods has become more popular recently and is projected to grow in the future.

On the numerical modelling aspect, the fluid-structure interaction problems can be classified broadly into two approaches: the ***monolithic approach*** and the ***partitioned approach***. The monolithic approach treats the fluid and the structures in the unified manner to form a single system equation for the FSI problem. Although this method usually produces highly accurate results, it consumes extensive computational resources. For large-scale FSI problems, this is sometimes impractical. On the other hand, the partitioned approach treats the fluid and the structures separately with different numerical approaches. The communication between the two are exchanged after some time. Depending on the direction and the frequency of information exchange, the partitioned approach can have different degrees of fluid-structure coupling. For a more complete description of the fluid-structure methods and their applications in the aerospace/turbomachinery context, one can refer to the review papers in Ref. [Marshall and Imregun, 1996; Kamakoti and Shyy, 2004].

2.1.4 Validation of Numerical Method

Development of efficient numerical methods for blade aeroelasticity needs to be accommodated with routine validations against the experiment data. Many test rigs have been built all over the world in the last decades to acquire the experimental data for oscillating blades. The testing facilities can be rotating or stationary (linear cascade). Rotating rigs are the most realistic simulator of blade flutter due to their close resemblance to the real engines. The early work of Stargardter [1977] obtained the vibration mode shapes under actual opearating conditions using a laser-based optical technique. Halliwell et al. [1984] measured the unsteady pressure data at one blade tip section of a shrouded transonic fan undergoing unstalled supersonic flutter. They showed the effect of a shockwave's position on the aeroelastic stability. Corral et al. [2019] described a high-speed rotating wind tunnel with non-intrusive measurement techniques such as blade tip-timing optical probes and unsteady pressure transducers. The rig was applied to study the flutter vibration of a turbine rotor under a wide range of operating conditions.

The above test rigs are of free flutter type, where flutter takes place both intentionally and unintentionally. The other type is the driven flutter test rig, where the blades are driven to pre-defined oscillation amplitude, frequency, and pattern using a driving mechanism. All blades can be excited according to the tuned blade travelling-wave theory of Lane [1956]. However, this is clearly more difficult and uneconomical because multiple driving motors have to be used. Instead, Hanamura et al. [1980] proposed the Influence Coefficient Method (ICM) that oscillated only one central blade and measured the unsteady pressures on the oscillating blade itself as well as its neighbours. Based on the linear superposition method, the unsteady pressures in the corresponding tuned vibration mode can be reconstructed from the measured data of the all blades. Since its introduction, it has become the most common method in getting equivalent tuned cascade data from experimental linear cascades and annular sector rigs. Examples of the applications of the ICM method in the experimental studies can be found in Ref. [Bölcs and Fransson, 1986; Buffum and Fleeter, 1990; L. He, 1998a; Vogt and Fransson, 2007; Bell and He, 2000; Yang and He, 2004; Huang et al., 2008; Huang et al., 2009; Ma et al., 2017]. In recent years, there have been more efforts on building the transonic test rigs that utilize the ICM method in acquiring the aeroelastic data [Tian et al., 2019; Watanabe et al., 2018; Gan et al., 2022].

These experimental test rigs have provided a great amount of validation data for CFD modelling practitioners, which in turn provides many insights into the physical mechanisms of the aeroelastic stability. Unlike the experimental set up, the computational setup does not face any difficulty on oscillating a large number blades although the efficient phase-shifted simulation method is frequently used. Therefore, it is common that CFD tuned cascade simulation data is validated against the ICM-based experimental data. Discrepancies between these two methods are sometimes observed but unfortunately quite a few researchers have mistakenly blamed it on the conventional turbulence modelling or the flow nonlinearity issues. In this thesis, the comparison between the tuned cascade and ICM-based cascade setup will be analysed in more details to demonstrate that they are not meant to be matched at certain conditions. Thus, one should exercise caution when comparing the two.

2.1.5 Three-Dimensional Effects on Blade Aeroelasticity

The turbomachinery aeroelastic data available in the public domain for validation purposes are scarce. However, the published detailed measurements are usually limited at mid-span 2D sections [Bölcs and Fransson, 1986]. Given the 3D nature of turbomachine blades, the understanding of fully three-dimensional features and their impact on the aeroelastic stability is important. Widely developed CFD solvers for blade flutter prediction also need 3D experimental cases for validation.

Blade tip leakage is an important three-dimensional flow feature that has attracted much attention from various researchers in the past. To avoid excessive blade-casing rubbing interactions, blades are manufactured with radial clearances. Due to the pressure difference between the blade suction surface and the blade pressure surface, the flow is leaked across this gap. Instead of convecting downstream, the flow travels in the circumferential direction across the tip gap. When the flow exits on the suction side, it forms a tornado-like vortex. The tip leakage reduces the throughflow mass and creates total pressure losses. In addition, the tip leakage vortex also blocks the axial incoming flow, which promotes stall at off-design conditions. The situation is exacerbated by an increase in tip clearance during operation as well as due to blade tip wear. Therefore, tip clearance is deemed to be detrimental to aerodynamic losses, stall inception, and stall margin [Storer and Cumpsty, 1991; Camp and Day, 1997]. Figure 2.3 illustrates the tip leakage vortex formation in a turbomachinery bladerow.

On the other hand, fewer researchers have studied the behaviour and impact of tip clearance on the compressor flutter stability, but there is however still lack of consistent findings. Yang and He [2004] showed a destabilizing effect when the tip clearance was increased in their low speed linear cascade experimental case subject to oscillation in a bending mode. Besem and Kielb [2017] investigated

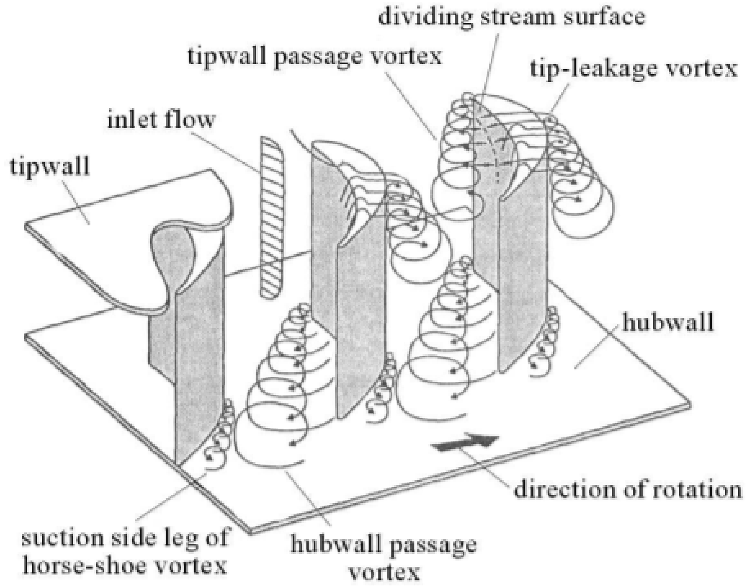

Figure 2.3: Illustration of typical three-dimensional flow phenomena in turbomachine blade passages [Sjolander, 1997].

computationally the effects of tip clearance for rotor blades oscillating in a torsion mode, but found a non-monotonic variation of aero-damping with tip clearance. The damping initially increased with the tip gap size until it reached a maximum and it then decreased with the further tip gap increases. And overall, the tip gap seemed to have a stabilizing effect compared to the zero tip-gap case [Besem and Kielb, 2017]. Dong et al. [2020] numerically studied the effects of tip clearance on the aeroelastic stability of a wide-chord fan rotor at 70% design rotation speed in a bending mode vibration. They found that the aerodynamic damping increased initially until reaching a maximum then decreased with an increase in tip gap. On the other hand, Fu et al. [2015] investigated a transonic rotor in a bending mode vibration, which was observed to subject to flutter during the rig test. They showed that the aerodynamic damping decreased with increasing tip gap until it reached a minimum, then an opposite damping variation with tip gap was observed. This finding is in contrast to that of Besem and Kielb [2017] and Dong et al. [2020]. Overall, the previous studies of tip-leakage effects on the compressor blade aeroelastic stability still remain inconclusive.

2.2 Mistuning Effects on Blade Aeroelasticity

To simplify the aeroelastic modelling and analysis procedures, the turbomachinery blades are typically assumed to be tuned such that all blades share the same mechanical properties and geometric shape. Thus, the whole-annulus domain can be efficiently modelled using a standard/phase-shifted periodic single-passage solution. Unfortunately, the assumption of identical blades can never be achieved in practice since the blade-to-blade variations are inevitably present due to manufacturing tolerances, assembly processes, as well as wear and tear. This problem, known as mistuning, has long been recognised by the community and is still an active subject of research. Mistuning can be classified into two main categories: ***structural mistuning*** and ***aerodynamic mistuning***. In the following sections, these mistuning types and their previous studies will be described in more details.

2.2.1 Structural (Frequency) Mistuning

Structural mistuning involves the change in structural parameters such as the blade mass, blade stiffness, and blade damping, which in turn induces the change in the blade eigen-frequency. It has also been referred to as frequency mistuning in past literatures. Sadeghi and Liu [2007] found that frequency mistuning would stabilise a cascade thanks to the temporally changing phase differences between adjacent blades using the fully-coupled method for a four-blade cascade configuration. In addition, they concluded that the effectiveness of frequency mistuning depends on the strength of fluid-structure coupling. Zhai et al. [2012] investigated the aeroelastic stability of a transonic compressor blade using a component-mode-based reduced order model. They reported that alternating frequency mistuning is not only robust in flutter alleviation but also potentially beneficial in the forced response relatively to the random mistuning. Utilizing the same reduced order model, Choi et al. [2003] performed an optimisation study to search for the most robust intentional mistuning pattern for bladed disks. They concluded that the optimised pattern might be irregular although only two blade variations A and B were considered in their study. Interestingly, the optimised pattern always showed a dramatic reduction of amplitude magnification due to an unintentional mistuning compared to the tuned cascade. For a more complete review of frequency mistuning, one can refer to Ref. [Castanier and Pierre, 2006].

2.2.2 Aerodynamic Mistuning

On the other hand, aerodynamic mistuning involves variations in the blade stagger angle, leading and trailing edge shape, blade thickness, and camber. The early study from Hoyniak and Fleeter [1986] showed that the alternating circumferential spacing mistuning enhance the stability for cases with the elastic axis at or forward of the airfoil mid-chord. When the elastic axis moved to 60% chord, the stability enhancement was minimal. Sladojecvic et al. [2007] used a whole-annulus time-domain solver to investigate the effects of alternating stagger angle on the stability of fan blade. They found that small changes of stagger angle (0.5deg) did not have a significant effect, whereas a large value of mis-stagger (2deg) could be considerably destabilizing. Ekici et al. [2010] introduced an approach to study aerodynamic mistuning using harmonic balance method to populate the aerodynamic coefficient matrix, which would then be used to solve the eigenvalue problem. Due to the nature of this approach, it is restricted to a set of symmetry group. Nevertheless, it was proved to be efficient in the investigation of alternating aerodynamic mistuning. They showed that the alternating blade spacing enhanced the blade stability, while the alternating blade staggering could be either beneficial or detrimental depending on the direction of mis-staggering. Ekici et al. [2013] expanded the aforementioned approach to investigate the problem of leading edge blending. They reported that alternating blending would be stabilizing for a loaded rotor but destabilizing for an unloaded rotor. Miyakozawa et al. [Miyakozawa et al., 2009] studied the effects of aerodynamic asymmetry on forced response by perturbing the influence coefficient matrix in the physical coordinates. The results showed that the amplification factor increased as the strength of random force perturbation increases. However, aerodynamic forcing perturbation had a secondary effect compared to frequency mistuning. Leng and Key [2020; 2021] built a method based on a generalized flat plate cascade model to investigate non-uniform blade spacing effects. They reported that the sinusoidal spacing pattern had the largest blade-to-blade variation, in which some blades experienced an unsteady loading three times higher than the tuned blade. Regarding the aerodynamic damping, they found that some mistuned blades could even have negative aero-damping at certain excitation nodal diameters, while the tuned bladerow was stable. Malzacher et al. [2019] performed the mis-staggering experimental investigation on a low-speed linear cascade. They concluded that mis-staggering could either have a beneficial or detrimental effect depending on the mistuning strength. However, the cascade stability seemed not to be affected significantly by the aerodynamic mistuning. Stapelfeldt and Vahdati [2018] investigated the discrepancies between rig tests and numerical predictions of the fan flutter boundary induced by unintentional mis-staggering. They found that, unlike mistuning, mis-staggering can have both beneficial and deteriorating effects on the flutter stability. For the unstable case, the aero-damping first decreases then increases. At a stable mass flow, the aero-damping increases slightly then decreases as the mis-stagger strength increases. They contributed the nonlinear effects due to the competition between the change in aerodynamic flow and the break of the symmetric pattern.

2.2.3 Concurrent Structural-Aerodynamic Mistuning

Works considering both structural mistuning and aerodynamic mistuning together are much scarcer in the literature. In the majority of this kind of study, a structural mistuning analysis takes into account aerodynamic effects through the use of the aerodynamic influence coefficient matrix (e.g. see Sladojevic et al. [2006], Petrov [2010], and Besem et al. [2016]). These previous works suggested that the aerodynamic mistuning could have significant effects on the blade aeroelasticity and might have nonlinear interactions with the structural mistuning. The matrix perturbation method allows the aerodynamic effects to be included in the aeroelastic calculation without the need to recalculate each mistuning pattern. However, this is also a drawback of the previous works because the probabilistic perturbation of the influence coefficient matrix lacks an appropriate physical interpretation. In a recent attempt, Stapelfeldt and Brandstetter [2021] developed a reduced-order model with a better physical representation to include the mistuning effects on nonsynchronous vibrations. They showed that additional structural mistuning lowered the critical decay rate of the aerodynamically mistuned system. However, mistuning effects were still manifested by scaling the coefficients.

2.2.4 Intentional Mistuning

It has been observed that mistuning may have beneficial effects on the blade aeroelasticity in some particular situations (e.g. flutter alleviation). Thus, engineers have intentionally used mistuning in the design consideration to take advantage of these beneficial effects. This is known as intentional mistuning, which is a *designed* variation adding on top of the random variation arising from manufacturing and operation processes. In this section, various intentional mistuning design concept will be summarised.

Early studies typically concluded that structural mistuning had benefical effects on blade flutter, while inducing adverse effecrs on blade forced response [Whitehead, 1966; Ewins, 1969; Kaza and Kielb, 1982; Srinivasan, 1997]. Therefore, intentional mistuning has typically been used to alleviate flutter, while minimizing the effects of the forced response level. Castanier and Pierre [2002] studied the intentional structural mistuning design with harmonic patterns for the forced response of an industrial rotor. They found that some certain harmonic patterns had much lower amplitude response compared to the tuned design. However, their studies used simple lumped parameter model without an aerodynamic coupling. Han et al. [2014] optimised the intentional structural mistuning patterns with only two types of blade to reduce the sensitivity of the forced response bladed disks to random mistuning. Beirow et al. [2019] demonstrated that intentional structural mistuning could drastically reduce the forced response caused by low engine order excitation. The designed mistuning was robust even with extra random mistuning from the manufacturing process. Figaschewsky et al. [2017] used heavy paint to structurally mistuned a jet engine fan. They successfully removed entirely the flutter bite at the expense of a reduced flow range due to a reduced passage area. Regarding the forced response, the response amplitudes did not change significantly. Chen et al. [2019] and Gao et al. [2020] used hard coating as a mean to introduce intentional structural mistuning to the blisk design, which had the potential to reduce the forced response amplitudes. An interesting unusual phenomenon in which the forced response levels of a mistuned bladed disk can be reduced below that of its tuned counterpart was revealed by Petrov [2011]. Some researchers applied this finding and showed that it is feasible to design a practical bladed disk that has reduced forced response amplitude [Martel and Sanchez-Alvarez, 2018; Beirow, Figaschewsky, et al., 2019].

Intentional aerodynamic mistuning for improving the blade aeroelasticity performance is not common in the past scientific publication. However, there have been some patent disclosures recently on this area. Kelly et al. [2010] provided mistuning by varying the pressure side thicknesses. Hayford et al. [2020] claimed for an intentional aerodynamic mistuning design method to reduce vibrations in a gas turbine engine with multiple bypass streams. In their patent, the radially inner array of airfoils were misaligned in the circumferential direction with the radially outer array of airfoils.

It is therefore not surprising that concurrent structural-aerodynamic intentional mistuning design approach has been almost unprecedented. Schoenenborn [2017] disclosed an intentional mistuning design approach where both structural mistuning and aerodynamic mistuning were applied concurrently to reduce vibrations due to surge. The structural mistuning was realised by variation of the stiffness, mass distribution, and/or area moments of inertia. The aerodynamic mistuning was realised by axial offset of the trailing edge.

2.3 Modelling of Mistuning Effects

Due to the probabilistic nature of mistuning, a large number of configurations has to be simulated. Thus, the use of reduce-order modelling method has been common for mistuning study. This section describes some common reduce-order modelling methods as well as a more direct computation of mistuning using the fully-coupled fluid-structure interaction method.

2.3.1 Lumped Parameter Models

The most basic and popular model especially in the early days of mistuning study is the lumped parameter models. It represents the dynamic system as a series of mass-spring-damper elements. This type of model is very computationally efficient, while retaining some useful vibration characteristics of the mistuned system. Figure 2.4 illustrates the mass-spring-damper setup of the lumped parameter model. Examples of mistuned study using the lumped parameter model can be found in Ref. [Castanier and Pierre, 2002; Lee et al., 2005].

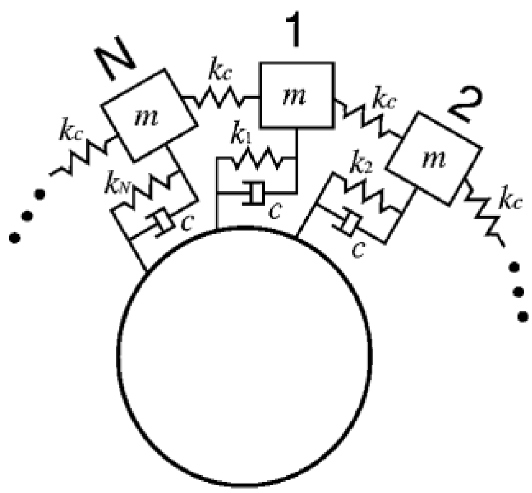

Figure 2.4: Illustration of the lumped parameter model [Castanier and Pierre, 2002].

Another closely related simplified model is the beam frame model, which can be seen as an upgrade of the lumped parameter model. The spanwise variation of blade oscillation amplitude can be simulated using this kind of model, thus high order mode shape can be captured. The Euler-Bernoulli's beam theory [Yuan et al., 2015; Shadmani et al., 2019] or the Timoshenko's beam theory can be adopted [Yuan et al., 2017]. Figure 2.5 illustrates the beam frame model, where the blades have multiple degree of freedoms in the spanwise direction.

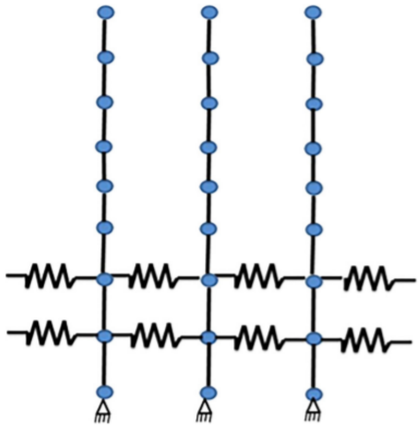

Figure 2.5: Illustration of the beam frame model [Yuan et al., 2017].

2.3.2 Component Mode Synthesis

The family of Component Mode Synthesis (CMS) methods is frequently used for bladed disk studies. The CMS methods divide a bladed disc into two sub-elements: the blades and the disc. Thus, their modes can be calculated separately. The two sub-elements are connected via the interface. There are different types of blade-disc interface: fixed interface [Hurty, 1965], free-interface [Irretier, 1983], and hybrid-interface [Ottarsson, 1994]. A strength of this family of methods is the capability to introduce blade eigen-frequency variations while taking into account the disc's response.

2.3.3 System Mode Based

The family of System Mode based Methods (SMM) is also popular in the literature. There are various methods falling into this group, notably the Fundamental Mistuning Model [Feiner and Griffin, 2002], the Component Mode Mistuning [Lim et al., 2007], and the Integral Mode Mistuning [Vargiu et al., 2011]. The underlying principle of this family of methods is to represent the mistuning effects as perturbations of the tuned system modes. Thus, the SMM methods tend to be more efficient than the CMS methods because fewer modes need to be used to approximate the mistuned system.

2.3.4 CFD-Based Reduced Order Models

Both the families of CMS and SMM methods are finite-element based reduced order modelling techniques for the structures. However, the vibrations of mistuned blades could induce significant fluid-structure coupling, for which the aerodynamic effects play a pivotal role. He et al. [2007] observed that the aerodynamic coupling significantly affects the bladed disk vibrations. Miyakoyawa et al. [2009] showed that the aerodynamic asymmetric perturbations can increase significantly the maximum blade amplitudes. Petrov [2010] proved that the inclusion of aerodynamic coupling was essential for an accurate prediction of forced response amplitudes. In order to incorporate the aerodynamic effects into the solution, the most popular approach is the influence coefficient methods. The underlying principle is to use the high-fidelity CFD model to calculate the aerodynamic response at a particular flow condition. Various works in the literature have adopted this approach [e.g. Sladojevic et al., 2006; Petrov, 2010; Besem et al., 2016].

Another popular CFD-based reduced order modelling method is the modal projection technique, in which the flow solutions are approximated by a few modal basis vectors. A common projection framework is Proper Orthogonal Decomposition (POD). For example, Epureanu et al. [2001] and Willcox and Peraire [2002] used POD to reconstruct the unsteady aerodynamics of oscillating blades.

2.3.5 Fluid-Structure Interaction

Fluid-structure interaction methods have rarely been used in blade aeroelasticity studies due to its expensive computational resource requirement. However, the methods are suitable to investigate the configurations with a high fluid-structure coupling degree. While there exist some previous works using the fluid-structure interaction method to investigate fundamental vibration characteristics of the tuned blade [e.g. Carstens and Belz, 2001; Vahdati et al., 2011; Gan et al., 2014], the application of the fluid-structure interaction method on mistuning is rare. The work of Sadeghi and Liu [2007] was early and notable in this aspect. They showed that the fluid-structure coupling had the tendency to decrease the effectiveness of mistuning on flutter alleviation. In addition, there is also a previous work from Salles and Vahdati [2016], who computed the frequency mistuning study using a high-fidelity fluid-structure interaction method and compared the results against the low-fidelity Fundamental Mistuning Model (FMM) based on the aerodynamic influence coefficients.

2.4 Summary

In this chapter, the past literatures regarding the numerical methods for blade aeroelasticity computation and the mistuning effects have been briefly reviewed. Although many efforts have been devoted to improve our understanding on the problems, there arise some challenges that require further investigations. They are summarised as below:

1. Validation cases of unsteady CFD simulation methods against experimental data with detailed 3D unsteady pressures are still lacking, particularly for cases with aerodynamic features of interest to aerodynamic designers (e.g. laminar separation bubble, tip clearance).

2. Blade aeroelasticity (flutter, forced response) predictions have been performed using uncoupled methods with great success in the last decades. However, the accuracy and effectiveness of uncoupled methods will be reduced when the innovative propulsion architecture and the lightweight material becomes more common. Thus, the fully-coupled fluid-structure interaction will become more popular in the near future when the computing power permits.

3. The physical behaviours and mechanisms of mistuned bladerows are lack of clear and systematic understanding. Past researches have mainly focused on the structural (frequency) mistuning effects. The aerodynamic mistuning have gain more attention recently although the findings are not conclusive. Investigations with concurrent structural-aerodynamic mistuning is even more scarce.

4. Due to the probabilistic nature of mistuning, a large number of simulations have to be run. Thus, it is common to use a reduced-order modelling technique to simplify the mistuning computation. However, the reduced-order models need to be used with care because of various restricting assumptions made during the model development. Fully-coupled methods are undoubtedly accurate and suitable for fundamental studies of mistuning. To enable the routine use of fully-coupled methods in the early design stage, a more efficient CFD-based simulation method is needed.

3
Methodology

Contents

This chapter reports the modelling procedures adopted in the present thesis. The baseline multi-scale technique and the influence coefficient method are also described, which serve as the starting point for further extensions in later Chapters.

3.1 Baseline Flow Solver

The commercial solver ANSYS CFX is used as the baseline solver for the Navier-Stokes governing equations. The advection terms are discretized by a bounded high resolution scheme similar to the principles proposed by Barth and Jesperson

[1989]. The spatial derivatives in the diffusion terms are evaluated at the location of each integration point using the tri-linear shape functions. The transient terms are discretized by the second-order backward Euler scheme. The unsteady Navier-Stokes equations are solved in an implicit manner:

$$\frac{\partial \rho}{\partial t} + \nabla \cdot (\rho \boldsymbol{U}) = 0 \tag{3.1}$$

$$\frac{\partial \rho \boldsymbol{U}}{\partial t} + \nabla \cdot (\rho \boldsymbol{U} \otimes \boldsymbol{U}) = -\nabla p + \nabla \cdot \tau \tag{3.2}$$

$$\frac{\partial \rho H}{\partial t} - \frac{\partial p}{\partial t} + \nabla \cdot (\rho \boldsymbol{U} H) = \nabla \cdot (\lambda \nabla T) + \nabla \cdot (\boldsymbol{U} \cdot \tau) \tag{3.3}$$

where the stress tensor τ is related to the strain rate by:

$$\tau = \mu \left(\nabla \boldsymbol{U} + (\nabla \boldsymbol{U})^T - \frac{2}{3} \delta \nabla \cdot \boldsymbol{U} \right) \tag{3.4}$$

The governing equations represent the conservation of mass, momentum, and energy at each instantaneous time level. To close the equations, the $k{-}\omega$ Shear Stress Transport (SST) turbulence model is adopted. Many turbomachinery applications show the laminar-turbulent transition behaviour, which are failed to captured by the fully-turbulent SST model. The $\gamma - \theta$ transition correlation coupled with the SST model will be used in these cases [Menter et al., 2004]. The term $\nabla \cdot (\boldsymbol{U} \cdot \tau)$ in Equation 3.3 represents the work due to viscous stresses and is called the viscous work term. This viscous effect on the heat transfer is taken into account by using the total energy model as seen in Equation 3.3.

Standard boundary conditions for turbomachinery aerodynamic applications are adopted. Total pressure, total temperature, and flow angle are specified at the inlet station. The static atmospheric pressure is used at the outlet. The blades, hub, and casing surfaces are modelled as adiabatic no-slip walls. The wall treatment automatically switches from the wall function [Launder and Spalding, 1983] to a low-Re near wall formulation as the mesh is refined. The inlet and outlet are treated as reflecting boundaries since the implementation non-reflecting boundary condition in ANSYS CFX is not robust [Mueller et al., 2021]. To prevent the spurious reflection, inlet and outlet are placed several chords away from the oscillating blade. The buffer zones with coarse mesh are also implemented at the inlet and outlet to damp out the incoming waves.

3.2 Fluid-Structure Interaction Solver

3.2.1 Method Description

The interaction between one or more solid structures and the surrounding fluid flow, known as the fluid-structure interaction (FSI) problem, is of interest in many applications. For turbomachinery applications, it has become more popular recently and is projected to grow in the future thanks to the increasing use of lightweight materials and innovative propulsion architectures. As summarised in the previous chapter, the fluid-structure interaction problems can be classified broadly into two approaches: the ***monolithic approach*** and the ***partitioned approach***. For the fluid-structure simulations in the present work, the partitioned approach is adopted. There are two timestep loop levels: the outer loop and the inner loop. The outer loop represents the physical time-step, while the inner loop represents the pseudo-time-step. At each inner loop iteration, data are exchanged between the fluid and the structure solvers. The structure solver receives the information of the aerodynamic forces/moments acting on the blade, while the fluid solver receives the updated blade position. The iterations continue until reaching the convergence criteria. A tightly coupled simulation process is adopted where data exchange occurs in every inner loop iteration. Because the tightly coupled fluid–structure interaction method is two-way iteratively implicit, the vibration characteristics is part of the solution. Thus, the method is suitable for an investigation of the unknown a priori vibration characteristics as in the present work with the mistuned oscillating cascade. Figure 3.1 illustrates the overview workflow of the fully-coupled fluid-structure interaction method adopted in the current work.

The fluid solver is described in the previous section. The blade structure is simplified as rigid body motion. Thus, the rigid body equations of motion are

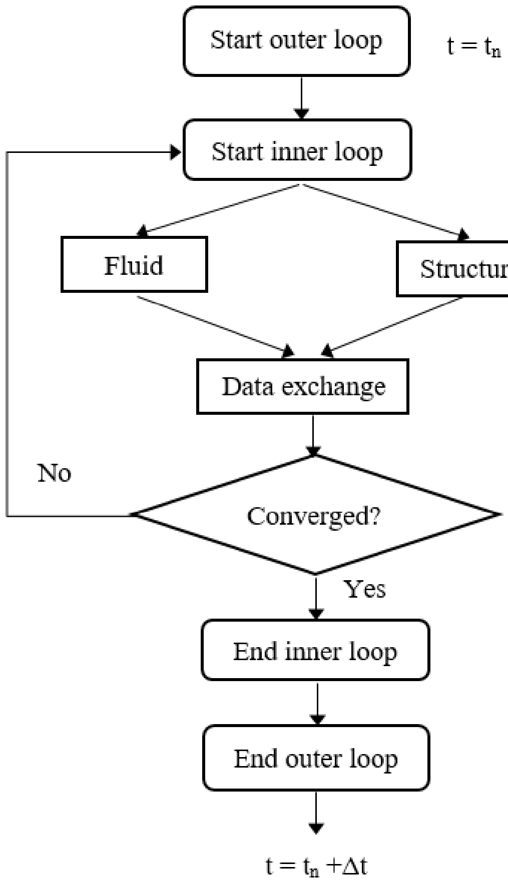

Figure 3.1: Flow chart of the fully-coupled fluid-structure interaction method.

solved separately for each vibration mode:

$$\frac{dP}{dt} = F_{aero} - k_{bending}\left(x - x_{COM}\right) \tag{3.5}$$

$$\frac{d\Pi}{dt} = M_{aero} - k_{torsion}\left(\theta - \theta_{COM}\right) \tag{3.6}$$

where P is the linear momentum, Π is the angular momentum. F_{aero} and M_{aero} denote the aerodynamic force and moment acting on the blade, respectively. Similarly, $k_{bending}$ and $k_{torsion}$ represent the stiffness in the respective degree of freedom.

3.2.2 Initial Perturbation Approaches

For an uncoupled simulation, a mode shape with fixed oscillation amplitude is used to drive the blade movement. The mesh motion is therefore known a-priori. At each time instant, the mesh motion equation will be solved separately from the flow equations, thus it is known as a uncoupled simulation.

On the other hand, for a fully-coupled fluid-structure simulation, the instantaneous oscillation amplitude is not known a-priori. It is an implicit result from the two-way balance of flow and rigid body equations such that the dependencies between the fluid and the structures are converged within a time step. Although the fluid initial conditions can be specified from the converged steady-state solution, the structural initial conditions require a special attention. Within the fully-coupled framework, there are more than one way to initialize/start the FSI simulations. For turbomachinery applications, it is a common practice to impose a specific initial inter-blade phase angle pattern according to the investigated nodal diameter [Doi and Alonso, 2002; Vahdati et al., 2011; Im and Zha, 2012]. This practice stems from the monochromatic travelling wave behaviour of turbomachinery flutter, which was proposed by Lane [Lane, 1956]. On the other hand, only few researchers used a non-travelling wave perturbation as an initial condition [Carstens et al., 2003; Corral and Gallardo, 2014] due to a high number of oscillation cycles needed to establish the coupled vibration characteristics, particularly for aerodynamically induced instabilities [L. He, 1994]. Although a travelling wave perturbation is more efficient, a non-travelling wave initialization is necessary if the vibration characteristics are not known a priori. In the present work, vibration characteristics of the mistuned cascade are of interest. Thus, the single-blade perturbation will be adopted for free response (self-excited) mistuned configuration, unless otherwise stated. On the other hand, the forced response computations involve a periodic excitation due to flow disturbances. The forced response vibration levels should be independent of the initial structure perturbation. Thus, there is no initial structural perturbation for the forced response simulations.

Figure 3.2 illustrates the initialization techniques for the fully-coupled simulations of the oscillating bladerow with and without the external excitation. Figure 3.2a shows that all blades have initial angular velocities for the travelling wave perturbation technique, while only a single blade has a non-zero initial angular velocity in Figure 3.2b. It can be seen that multiple nodal diameter vibration modes are excited during the transient process in the single-blade perturbation technique.

However, the unstable modes eventually die out, leaving only the most unstable mode in the vibration history. The time taken of this process depends on the blade-to-blade coupling strength. In addition, Figure 3.2c shows the blade vibration displacement with time for a typical forced response computation. Although the blades do not have an initial perturbation, they are constantly subjected to the periodic external forcing. As a result, they are excited and the steady-state response amplitude is a two-way balance between the forcing and the damping work.

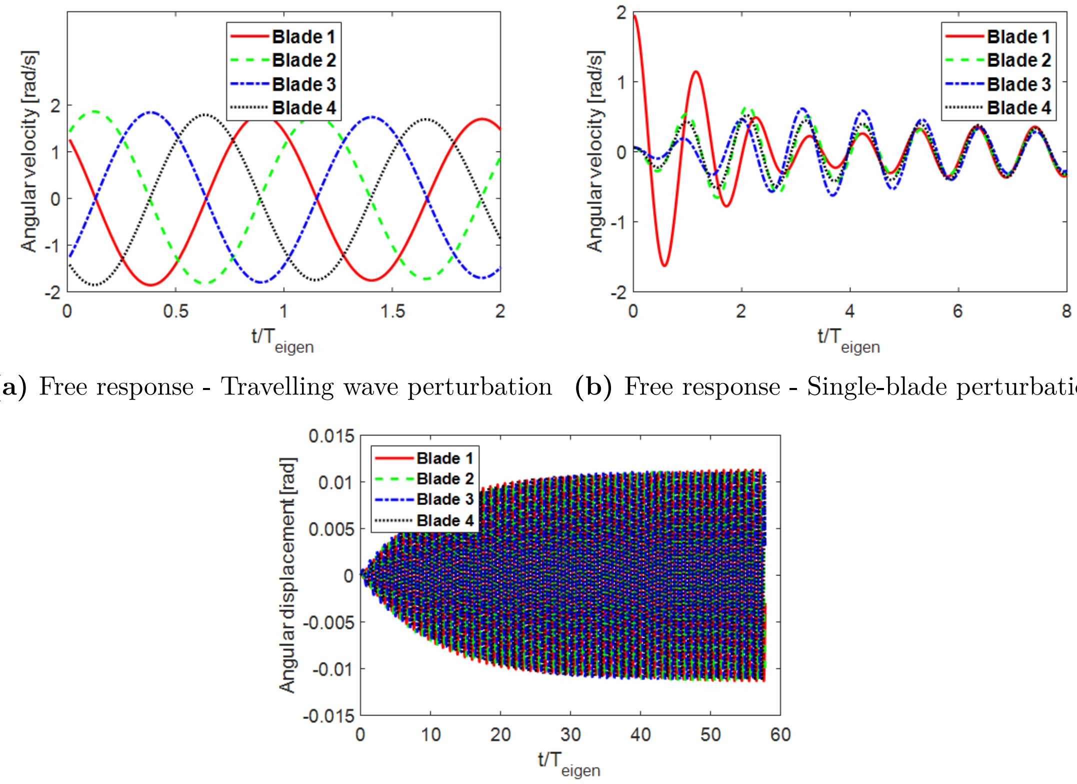

(a) Free response - Travelling wave perturbation **(b)** Free response - Single-blade perturbation

(c) Forced Response - No initial perturbation

Figure 3.2: Different initialization techniques for the fully-coupled simulations of the oscillating bladerow.

3.2.3 Data Post-Processing

Aerodynamic Damping

Because no mechanical damping is considered in the present work, aerodynamic forces are solely responsible for the damping effects. For uncoupled simulations, the aerodynamic work can be calculated from the energy method:

$$W = \int_0^T \int_S p\mathbf{n} \cdot \mathbf{u} ds dt \tag{3.7}$$

The non-dimensional aerodynamic damping can be calculated from the aerodynamic work.

On the other hand, the standard logarithmic decrement is used for fully-coupled simulations based on the readily available time-domain vibration history:

$$\log \text{dec} = \frac{1}{n} \ln \left(\frac{\hat{q}_n}{\hat{q}_0} \right) \tag{3.8}$$

where $\hat{q}$ is the peak vibration amplitude.

The aerodynamic damping and the logarithmic decrement can be converted to one another. However, the global log-dec parameter does not provide meaningful understanding of local vibration effects. As a result, the Hilbert transform-based analysis approach [Phan, 2021] is used to further analyse the fully-coupled simulation results. This analysis method can be seen as an improved energy method, where the spatial and temporal dependency of the aerodynamic damping can be computed. Thus, it is particularly suitable for the non-linear non-stationary data obtained from the time-domain fully-coupled fluid-structure simulation. In Ref. [Phan, 2021], it was shown that this method is consistent to the conventional energy method for uncoupled simulation analyses. For a more detailed methodology formulation, one can refer to Ref. [Phan, 2021] and the Appendix A. The procedures are briefly presented in the current work.

The instantaneous damping work can be calculated as:

$$W_d(t) = -\hat{f} \omega \hat{q} \cdot \sin \psi \cdot \cos^2(\omega t) \tag{3.9}$$

The instantaneous aerodynamic damping is given as:

$$\Xi(t) = \frac{W_d(t)}{(P_{01} - P_2)\, \hat{q}_{tip}^2} \tag{3.10}$$

The time-averaged aerodynamic damping can be found from any time interval:

$$\Xi_{avg} = \int_{t_1}^{t_2} \Xi\left(t\right) dt \tag{3.11}$$

The instantaneous amplitude and phase can be calculated directly from the original signals and their respective Hilbert transforms:

$$\hat{f} = \sqrt{f^2 + \tilde{f}^2}$$
$$\hat{q} = \sqrt{q^2 + \tilde{q}^2}$$
$$\psi = \arctan\left(\frac{q\tilde{f} - \tilde{q}f}{qf + \tilde{q}\tilde{f}}\right)$$

where ˆ is the amplitude and ˜ is the Hilbert transform operator.

Forced Response Amplitude

In a forced response calculation, one is interested in the steady/quasi-steady vibration amplitude. The instantaneous amplitude can be calculated as followed:

$$\hat{q}\left(t\right) = \sqrt{q^2 + \tilde{q}^2} \tag{3.12}$$

The time-averaged forced response amplitude can be found from any time interval:

$$\hat{q}_{avg} = \int_{t_1}^{t_2} \hat{q}\left(t\right) dt \tag{3.13}$$

3.3 Multi-Scale Method

3.3.1 Method Formulation

The multi-scale method is a source term-based approach that has been developed for solving different regimes with markedly different length and time scales [L. He, 2013b; L. He, 2013a; L. He, 2018]. The multi-scale method has been typically used to deal with problems of many repetitive fine-scale element such as film and effusion cooling holes [Duan and He, 2020] as well as the additively manufactured micro-patterns [Kapsis et al., 2020]. In the present work, we adopt the multi-scale method in a global manner, i.e. each passage domain has a particular global region in which the fine mesh is completely replaced by its coarse mesh counterpart. This approach would significantly reduce the total mesh count for the whole annulus bladerow compared to its direct fine mesh assembly, leading to an effective computational saving. The method of using two disparate mesh resolutions in this context is also referred to as the two-scale method.

In the most basic formulation of the multi-scale method, the steady Navier-Stokes equations can be written in a semi-discrete form:

$$R(\boldsymbol{U}) = 0 \tag{3.14}$$

The conservative flow variable $\boldsymbol{U}$ is a seven-element vector for a three-dimensional unsteady flow with two-equation turbulence model, $\boldsymbol{U} = [\rho\ \rho u\ \rho v\ \rho w\ \rho E\ \rho k\ \rho\omega]^T$. $R(\boldsymbol{U})$ is the lumped advection and diffusion terms.

We begin with the fine mesh simulation as in a conventional time-marching approach. If the simulation converges, the instantaneous governing equations are satisfied:

$$R_f(\boldsymbol{U}_f) = 0 \tag{3.15}$$

Supposing the same flow domain is now discretized with a reduced spatial resolution. The poorly resolved but converged coarse mesh solution still satisfies the equations:

$$R_c(\boldsymbol{U}_c) = 0 \tag{3.16}$$

The loss of solution accuracy when the mesh resolution reduces is obvious. Thus, in order to recover the fine mesh solution in the two-scale computation, the fine mesh solution needs to be projected to the coarse mesh discretization through volume-weighted averaging:

$$\boldsymbol{U}_{f\to c} = \frac{1}{\Delta V_c} \sum \boldsymbol{U}_f \Delta V_f \tag{3.17}$$

where the summation is taken for all the fine mesh cells of volume ΔV_f corresponding to a coarse mesh cell of ΔV_c.

The volume-weighted averaging solution $\boldsymbol{U}_{f\to c}$ to be recovered in the two-scale simulation must also satisfy Equation 3.14. However, due to the difference between the volume-averaged solution $\boldsymbol{U}_{f\to c}$ and the coarse mesh solution $\boldsymbol{U}_c$, the projected solution $\mathbf{U}_{f\rightarrow c}$ does not satisfy the discretized governing equations on the coarse mesh:

$$R_c\left(\boldsymbol{U}_{f\rightarrow c}\right) \neq 0 \tag{3.18}$$

Equation 3.18 can then only be balanced if a source term is introduced to the right-hand side of the equations [Ning and He, 2001]:

$$R_c\left(\boldsymbol{U}_{f\rightarrow c}\right) = \boldsymbol{S} \tag{3.19}$$

where $\boldsymbol{S}$ is the steady source term arisen due to the spatial resolution reduction. It is also a seven-element vector, where each entry is to balance its corresponding governing equations at anywhere in space and time.

3.3.2 Steady Source Term Computation

Consider a given steady solution projected onto the coarse mesh, one can evaluate the source term explicitly using the solver numerical discretization algorithm:

$$R\left(\boldsymbol{U}\right) = \boldsymbol{S} \tag{3.20}$$

However, if the detailed discretisation process is not known as typically in a commercial solver, the required source term can be evaluated using an iterative approach. The iterative procedures involve marching the solution with a pseudo time step $\Delta\tau$. The source term change at a pseudo time step n is calculated as the difference between the target flow solution and the current flow solution:

$$\Delta\boldsymbol{S}_n = \frac{1}{\Delta\tau}\left(\boldsymbol{U} - \boldsymbol{U}_n\right) \tag{3.21}$$

Starting from an initial value of the source term (typically given as zero for generality), the iterative procedure is repeated and a new value of the source term is updated based on the previous value and the source term change. An under-relaxation factor α is used to stabilize the iterative process:

$$\boldsymbol{S}_n = \boldsymbol{S}_{n-1} + \alpha\Delta\boldsymbol{S}_n \tag{3.22}$$

The iteration proceeds until the source term approaches a constant value and the L2-norm of the source term change drops several orders of magnitude. Apparently when the source term iteration converges $\Delta \boldsymbol{S}_n \rightarrow 0$ and the current flow solution $\boldsymbol{U}_n$ approaches the target time-averaged flow solution $\boldsymbol{U}$. Thus, the projected flow solution on the coarse mesh has been recovered.

Although the above iterative process has been discuss with the steady simulation, a similar approach is also used to compute the time-averaged source term by replacing the steady quantities by their time-averaged counterpart.

3.4 Influence Coefficient Method

3.4.1 Basic Vibration Characteristics of the Tuned Cascade

Dynamic characteristics of the turbomachinery blade is distinctively different from that of the isolated airfoil due to the presence of neighbour blades. The bladerow could produce multiple aeroelastic travelling-wave modes depending on the blade count. Under the single-mode tuned blade assumption [Lane, 1956], the bladerow will undergo vibrations at a unique travelling-wave mode with a constant interblade phase angle (or nodal diameter) and a constant vibration frequency and amplitude.

The first basic concept is the nodal diameter, which is defined as the set of points along the annulus diameter having zero displacement. It divides the whole annulus into a group of blades. Figure 3.3 illustrates the nodal diameter concept for $ND = 1$ and $ND = 2$. In addition, the instantaneous position of the blades are plotted for reference.

For each nodal diametric mode, there exists a forward traveling wave mode and a backward traveling wave mode with the same nodal diameter. For a compressor bladerow, the direction of positive traveling wave is usually defined as opposite to the direction of rotation. Figure 3.4 illustrates the concepts of forward and backward travelling-wave modes.

(a) Nodal diamter $ND = 1$

(b) Nodal diamter $ND = 2$

Figure 3.3: Illustration of the nodal diameter concept for the oscillating tuned bladerow.

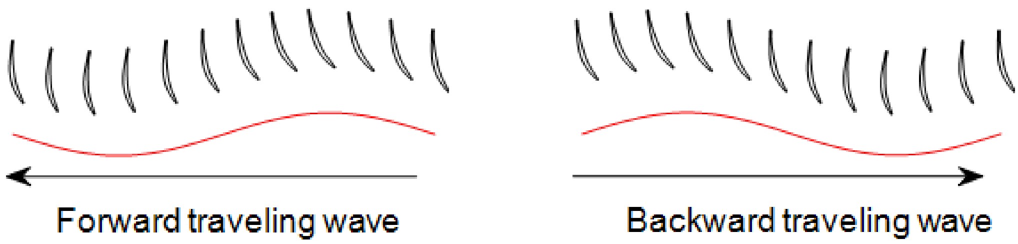

Figure 3.4: Illustration of the forward and backward travelling-wave mode concept for the oscillating tuned bladerow.

3.4.2 Classical Influence Coefficient Method

In order to quantify the aeroelastic properties of interest for a given travelling-wave mode of the oscillating tuned cascade, all blades have to be vibrated as demonstrated in Figure 3.3 and 3.4. Although this is a more straightforward approach, it is uneconomical, particularly for an experimental setup. Hanamura et al. [1980] proposed an alternative approach, where only one blade is vibrated while other blades remain stationary. This method is known widely as the influence coefficient method (ICM). Since its introduction, it has become the most common method in getting equivalent tuned cascade data from experimental linear cascades and annular sector rigs with only one blade oscillating [Bölcs and Fransson, 1986; Buffum and Fleeter, 1990; L. He, 1998a; L. He, 1998b; Bell and He, 2000; Huang et al., 2008; Huang et al., 2009; Vogt and Fransson, 2007; Watanabe et al., 2018; Malzacher et al., 2019]. The influence coefficient method works under the basis of the linear superposition approach. Figure 3.5 illustrates the influence coefficient method setup, where only the middle blade (B_0) is oscillated and the other blades are kept stationary. The effects of the reference blade's vibration on itself and on its neighbours are measured and recorded.

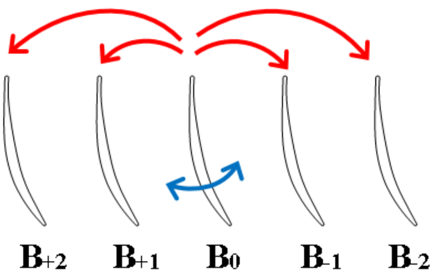

Figure 3.5: Illustration of the influence coefficient method for blade deformation.

Then in the equivalent tuned cascade data reconstruction, the influences of the vibrating blade and its neighbour are linearly superimposed by taking into account the constant interblade phase angle. The tuned data reconstruction process is illustrated in Figure 3.6.

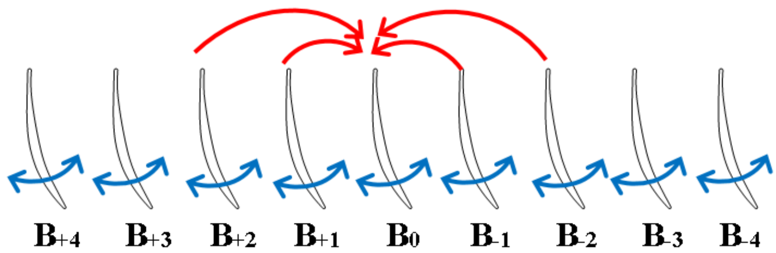

Figure 3.6: Illustration of source term superimposition in a mis-staggered bladerow.

The mathematical equivalence of the aforementioned process is defined as Equation 3.23. As can be seen, the 1st harmonic unsteady pressure coefficient of the tuned cascade $Cp_{1,tuned}$ can be reconstructed by summing the unsteady pressure coefficients from the oscillating blade itself and its neighbouring stationary blades $Cp_1\left(m\right)$, taking into account the constant inter-blade phase angle σ:

$$Cp_{1,tuned} = \sum_{m=-N/2}^{+N/2} Cp_1\left(m\right) e^{-im\sigma} \tag{3.23}$$

where m is the blade number index. N is the total number of blades in the whole annulus assembly. σ is the constant interblade phase angle defined as positive for a forward travelling wave mode.

3.4.3 Generalised Influence Superposition Method

Based upon the linear superposition principle, the total effects acting on a reference blade embedded within an oscillating bladerow can be expressed as the summation of the effects of each blade of the bladerow vibrating individually respectively (a similar concept to section 3.4.2). In the most general form, the linear superposition can be expressed as in Equation 3.24:

$$U_{total}\left(t\right) = \sum_{m=-N/2}^{+N/2} U_m\left(t\right) \tag{3.24}$$

where U_{total} is the total effects acting on a reference blade in an oscillating bladerow; U_m is the individual effect originated from blade m in vibration while all other blades are kept stationary. Note that the indexing in Equation 3.24 is always around the reference blade ($m = 0$). Thus U_0 is the influence of the vibrating blade on itself.

Equation 3.24 is intentionally expressed in the time domain as we are interested in a more general mistuned situation where neither should a constant frequency, nor a constant interblade phase angle for a vibrating bladerow be assumed. Using a Fourier decomposition approach, the time series data is converted to a frequency domain representation with infinite number of harmonics.

$$U_{total}\left(t\right) = \sum_{m=-N/2}^{+N/2} \sum_{n=1}^{\infty} A_{m,n} \sin\left(n\omega_m t + \theta_{m,n}\right) \tag{3.25}$$

where $A_{m,n}$ and $\theta_{m,n}$ is the amplitude and phase originated from blade m with n harmonics; ω_m is the fundamental vibration frequency of blade m.

The Fourier series in Equation 3.25 can be approximated by including up to N_f harmonics:

$$U_{total}\left(t\right) \approx \sum_{m=-N/2}^{+N/2} \sum_{n=1}^{N_f} A_{m,n} \sin\left(n\omega_m t + \theta_{m,n}\right) \tag{3.26}$$

For some cases such as oscillating blades, each blade would typically have a dominant and well-characterised fundamental frequency. Thus, it can be reduced further to include only the term with fundamental frequencies:

$$U_{total}\left(t\right) \approx \sum_{m=-N/2}^{+N/2} A_{m,1} \sin\left(\omega_m t + \theta_{m,1}\right) \tag{3.27}$$

where $A_{m,1}$ and $\theta_{m,1}$ is the 1st harmonic amplitude and phase originated from blade m.

It can be seen from Equation 3.27 that each blade m would still have its own vibration characteristics including the fundamental frequency ω_m, the 1st harmonic amplitude $A_{m,1}$, and the 1st harmonic phase angle $\theta_{m,1}$. In the simplest case where all blades are tuned, each blade would have the same fundamental frequency $\omega_m = constant$ and the same interblade phase angle $\sigma = \theta_{m+1} - \theta_m = \theta_m - \theta_{m-1} = constant$. Equation 3.27 for a tuned cascade can be rewritten and simplified as:

$$U_{tuned}\left(t\right) \approx \sum_{m=-N/2}^{+N/2} A_{m,1} \sin\left(\omega t + \theta_{m,1} + m\sigma\right) \tag{3.28}$$

where $A_{m,1}$ is the 1st harmonic amplitude of the influence due to the vibrating reference blade on the blade m; $\theta_{m,1}$ is the 1st harmonic phase of the influence due to the vibrating reference blade on the blade m; σ is the constant interblade phase angle. The local influence on blade m needs to be shifted back to the reference blade (blade 0), thus we need the $m\sigma$ term.

Equation 3.28 can be written in the complex form, which is exactly the same as in the classical influence coefficient method (section 3.4.2):

$$U_{tuned}\left(t\right) \approx \sum_{m=-N/2}^{+N/2} U_m\left(m\right) e^{-im\sigma} \tag{3.29}$$

where $U_m\left(m\right)$ is the local influence on blade m. Thus it needs to be shifted back to the reference blade (blade 0) as indicated by the term $e^{-im\sigma}$.

In summary, this section has outlined the basis of the generalised influence superposition method, for which no assumptions have been made regarding the constant frequency, amplitude, and/or phase angle of the oscillating blades. It has also been shown that under the assumption of the tuned cascade, the generalised influence superposition method can be reduced to the exact form of the classical influence coefficient method.

Another interesting aspect of the generalised influence coefficient method is its application on reconstructing different quantities other than unsteady pressure as in the classical method. In the later chapters, the author will show that the influence coefficient method can be used for the source terms in combination with the multi-scale method. The author believes that it is another innovative applications of the influence coefficient method.

4

Validation of Three-Dimensional Linear Oscillating Cascade

Contents

This chapter describes the baseline test case configuration. Steady and unsteady flow simulation results are validated against the available experimental data, with the particular attention on the effects of the laminar separation bubble and the tip clearance. In the second part, the validity and applicability of the influence coefficient method in a linear cascade setup are examined.

4.1 Test Case

4.1.1 Description

The compressor blade profile used in this study is the controlled-diffusion blading proposed by Elazar et al. [1990], which has been studied extensively for its steady performance in modern blade profile designs. The blading was utilized in an oscillating cascade test but operated at a reduced Reynolds number. At the original design Reynolds number, $Re = 7 \times 10^5$, there is no bubble separation identifiable. The same blading was adopted in an oscillating cascade experiment at a lower Reynolds number of $Re = 1.95 \times 10^5$ [Yang and He, 2004]. At this lower Re, a laminar bubble separation forms around mid-chord on the suction surface. Numerical simulations by high-fidelity scale-resolving methods also showed the formation of the separation bubble [L. He and Yi, 2017].

Although the cascade was studied at a low-speed condition, it consists of various important features in gas turbine aerodynamic blading design, including the laminar bubble separation and the tip clearance effects. A laminar bubble type separation with subsequent transition to turbulent flow is relevant to turbomachinery design applications for both turbine and compressor bladerows. For compressors in particular, the laminar separation-transition on a blade suction surface is also closely relevant to aerodynamic performances, as extensively studied in the past, e.g. by Dong and Cumpsty [1990], Halstead et al. [1997], Cumpsty et al. [1995]. Thus, it is of interest to assess the aeroelastic impact and predictability of a mid-chord laminar bubble separation on a compressor cascade, although there has been rarely any published work in this aspect so far.

The detailed measurement of unsteady pressures on different spanwise sections over the blade surfaces, especially in the near tip region makes this case suitable for validating modelling techniques and methods, and for exploring and understanding flow physics.

Table 4.1 shows a comparison between experimental and simulated operating conditions. Reynolds number Re and reduced frequency k are matched to a less than 5% discrepancy from the experimental conditions.

Table 4.1: Experimental and numerical operating conditions of the test case.

Conditions	Experimental	Numerical
Inlet flow angle β_1, deg	37.5	37.5
Reynolds number (based on blade chord and exit velocity), Re	1.95×10^5	1.967×10^5
Exit isentropic velocity V_{ref}, ms $^{-1}$	19.5	20.4
Reduced frequency k	$0.2, 0.4$	$0.2, 0.4$
Nominal frequency f, Hz	$4.14, 8.28$	$4.14, 8.28$
Mode shape	Bending, normal to chord	
Tip bending amplitude, Am_{tip}	$0.06C$	
Hub bending amplitude, Am_{hub}	$0.005C$	

4.1.2 Data Reduction

The influence coefficient method (ICM) is employed in both the experimental and the computational validation study to obtain the overall damping for different interblade phase angles (IBPA). As such the whole range of the damping-IBPA variation for a given frequency can be obtained, as commonly required. The key feature, particularly important for experimental setups, is only one blade (blade '0' in the middle, Figure 4.1) in the cascade needs to be oscillated.

The unsteady pressures along all blade surfaces are measured and recorded during a period of vibration. The unsteady pressures are decomposed into temporal Fourier harmonic components:

$$\begin{aligned} p(t) &= a_0 + \sum_n \left[a_n \cos(n\omega t) + b_n \sin(n\omega t)\right] \\ &= a_0 + \sum_n Ap_n \sin(n\omega t + \phi_n) \end{aligned} \tag{4.1}$$

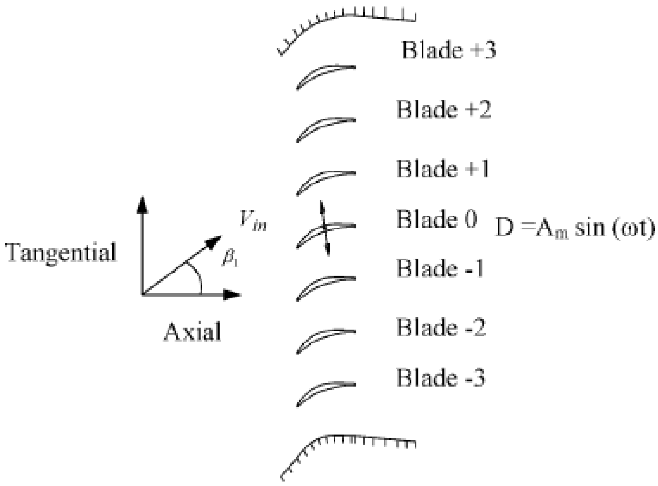

Figure 4.1: Experimental linear cascade configuration for influence coefficient method with only the reference Blade 0 oscillating, reproduced from Yang and He [2004].

Under the assumption of linear superposition, the unsteady aerodynamic influences on a reference blade from all oscillating blades in a tuned cascade (TWM) is equivalent to the sum of unsteady aerodynamic influences of one blade oscillating on itself and on all other non-oscillating blades in the cascade. Therefore, the first harmonic pressure coefficient of the reference blade (central blade) in TWM can be calculated as a sum of first harmonic pressure coefficients from the oscillating blade itself and its neighbouring stationary blades:

$$Cp_1 = \sum_{m=-3}^{+3} Cp_1\left(m\right) e^{-im\sigma} \tag{4.2}$$

where the IBPA σ is defined as positive for a forward travelling wave mode, where blade +1 leads blade 0 (see Figure 4.1).

For a blade oscillated in the sinusoidal motion, only the 1st harmonic pressure does aero-work (Work Sum) on the blade.

$$W_{aero} = \pi Am_l Ap_1 \sin\left(\theta_1\right) \tag{4.3}$$

The local aerodynamic damping is normalized by the blade tip vibration amplitude and the isentropic exit dynamic head.

$$\begin{aligned} \xi_l &= \frac{-W_{aero}}{\left(P_{01} - P_2\right) Am_{tip}^2} \\ &= \frac{-\pi Am_l \mid Cp_1 \mid \sin\left(\theta_1\right)}{Am_{tip}} \end{aligned} \tag{4.4}$$

The overall damping is calculated by integrating the local damping along the blade chord and span:

$$\xi_c = \frac{1}{C}\int_0^C \frac{-\pi Am_l \mid Cp_1 \mid \sin(\theta_1)}{Am_{tip}}\, ds \tag{4.5}$$

$$\xi = \frac{1}{h}\int_0^h \xi_c \, dz \tag{4.6}$$

4.2 Steady Flow Results

4.2.1 Sensitivity to Mesh Resolution

In the present thesis, meshing is carried out using ICEM to generate a high-quality unstructured hexahedral volume mesh. HOH topology is used to create H mesh in the inlet and outlet blocks. The main domain containing the blades are modelled with O grid around the blade surfaces to resolve the boundary layers. For 3D mesh, the tip clearance is modelled as gridded tip, which provides a smooth transition of fluid flow from the passage to the tip region. To ensure that the mesh resolution is sufficient, simulations of three mesh levels are carried out for a 3D single passage. The final mesh resolution is sufficiently fine to capture the flow physics. The final mesh size has 280x75x100 elements in the axial, circumferential, and radial directions. About 20 elements extra are needed in the tip radial direction of the tip gap region for each 1% span of tip clearance. This mesh resolutions yields approximately two million mesh celss for a single 3D blade passage. Figure 4.2a presents the overview 3D mesh of a single passage. Figure 4.2b details the mesh near the hub region, while Figure 4.2c details the mesh near the tip region. Figure 4.3 summarises the mesh sensitivity study results with two aerodynamic quantities of interest, namely the total pressure ratio P_{01}/P_{02} and the mass flow rate. The values are normalised against the value of the finest mesh configuration. The mesh sensitivity results show that the chosen mesh resolution of two-million cells per single 3D passage is justified taken into account the balance between the desired accuracy and the simulation efficiency.

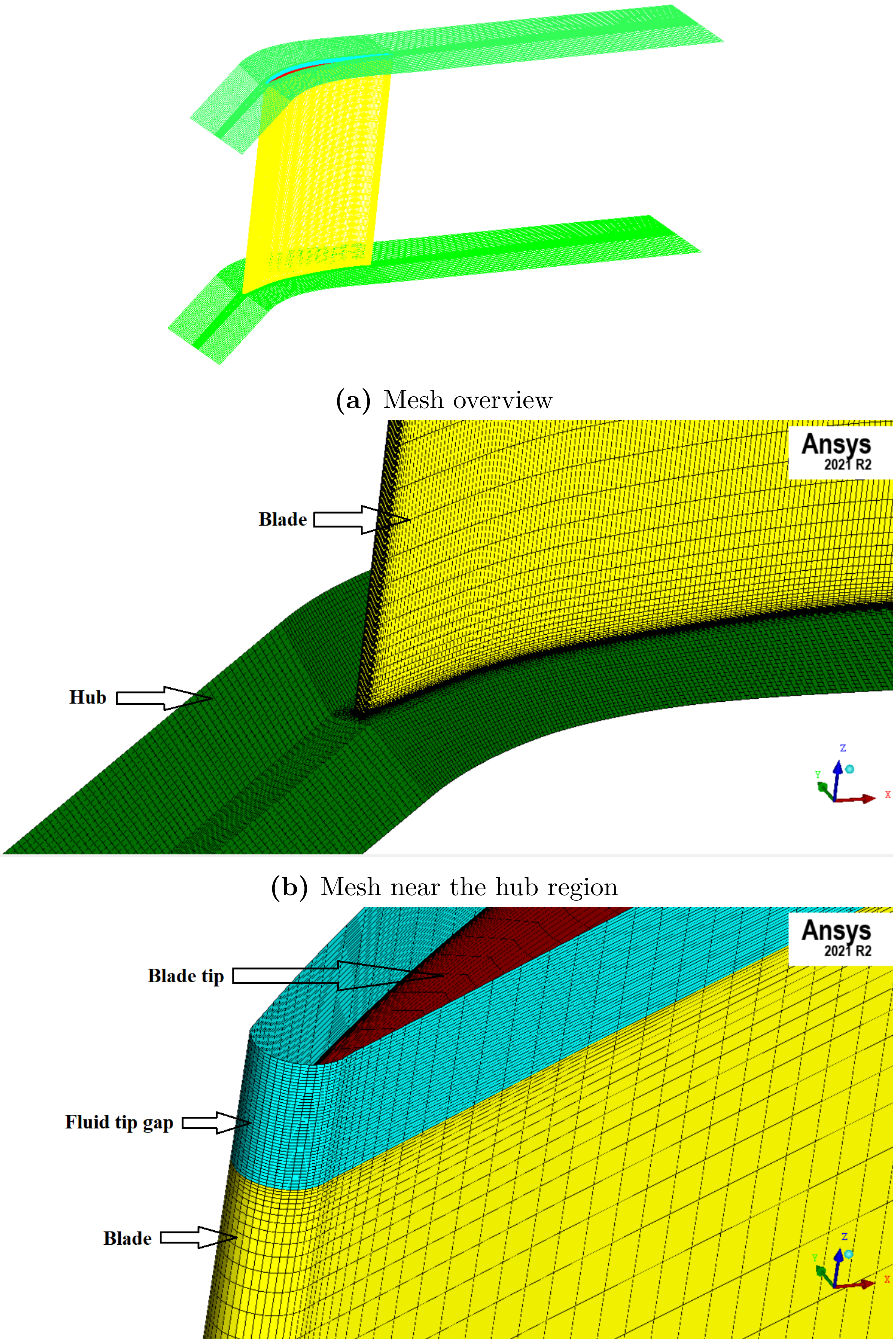

(a) Mesh overview

(b) Mesh near the hub region

(c) Mesh near the tip region

Figure 4.2: 3D mesh details of a single passage.

4.2.2 Sensitivity to Turbulence and Transition Modelling

The laminar bubble separation is captured on the suction surface in the experiment. In the computational study, the turbulence sensitivity shows that only the two-equation $\gamma - \theta$ transition correlation coupled with the SST model [Menter et al.,

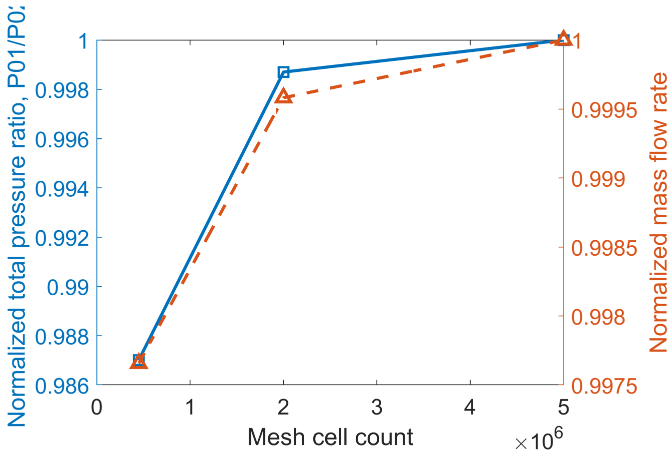

Figure 4.3: Mesh sensitivity study.

2004] is able to predict the separation bubble numerically. Figure 4.4 presents the axial Mach number contours predicted by both the transitional and the fully turbulent models. The laminar separation bubble is clearly identified by the zone of negative axial Mach number, which indicates a flow reversal region.

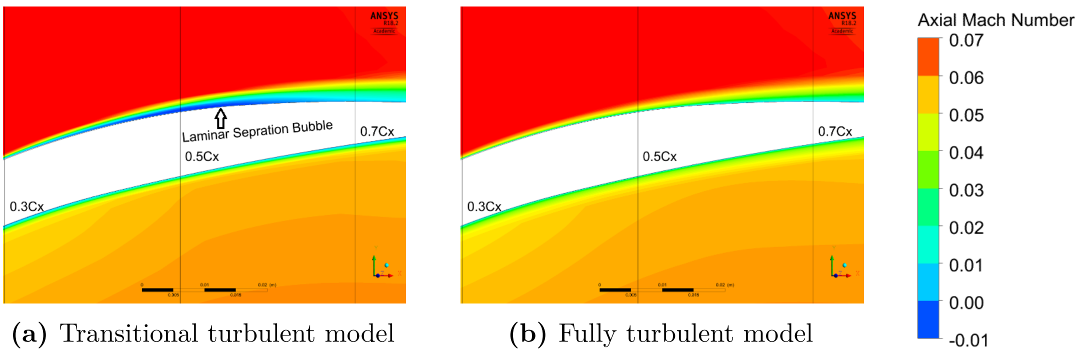

(a) Transitional turbulent model **(b)** Fully turbulent model

Figure 4.4: Axial Mach number contours predicted by different turbulence models.

Figure 4.5 shows the improved predictability of the transitional model from 30% to 50% chord. This computed bubble separation agrees with the experimental results, whereas the boundary layer remains attached if the fully turbulent model is used.

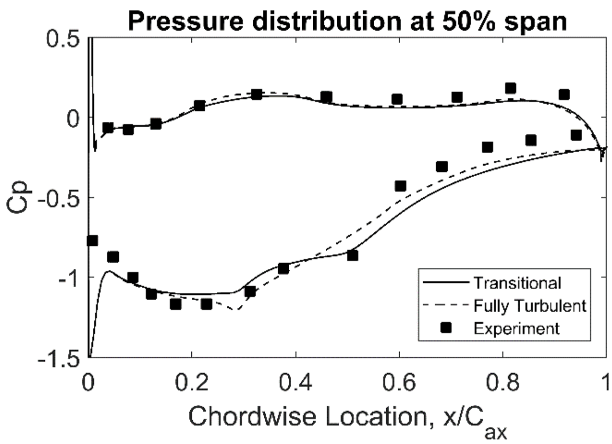

Figure 4.5: Steady pressure of different turbulence models.

4.2.3 Effect of Inlet Endwall Boundary Layer

One of the notable feature of this cascade as experimentally observed is the unloading effect near the endwall. If the uniform total pressure is applied at the inlet (i.e. the endwall boundary would only start to grow from the inlet plane), no significant unloading near the endwall can be observed in the computational results. Figure 4.6 shows different inlet endwall boundary layer thickness configurations that has been tested in the present work. The experimental endwall boundary layer thickness reported by Yang [2004] was shown to over-predict the endwall boundary layer effect numerically. Instead, the endwall boundary layer thickness is reduced gradually to match the steady blade loading recorded in the experiment. The endwall boundary layer thickness with 5% span thinner is finally chosen in the present work due to its excellent match with the experimental data. This is approximately the same size as what was reported by Williams et al. [2010] in the same test rig and under the same flow conditioning. The inlet total pressure loss coefficient Y_p is defined as:

$$Y_p = \frac{P_{01} - P_0}{P_{01} - P_2} \tag{4.7}$$

where P_{01} is the mid-span inlet total pressure, P_0 is the local total pressure, P_2 is the static pressure at the outlet.

Figure 4.7a presents the steady pressure distributions at 50% and 95% spans for the simulation with the uniform inlet boundary condition. There is hardly any

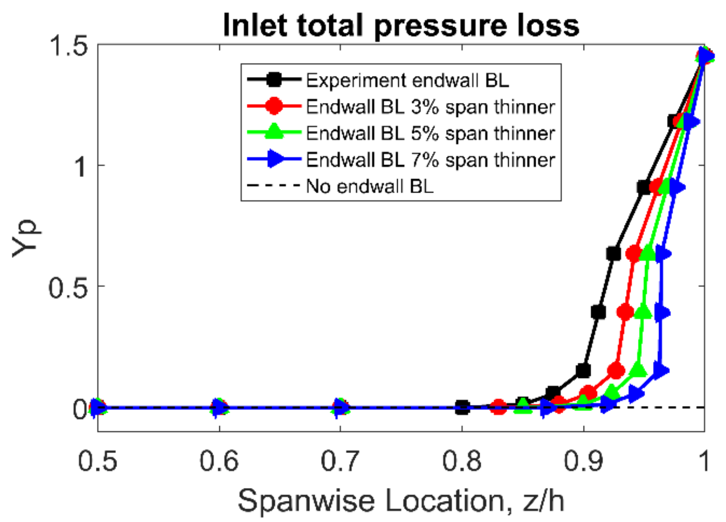

Figure 4.6: Total pressure inlet profile with different endwall boundary layer thickness.

unloading in the tip region in the computed results, clearly in disagreement with the experimental data. The key parameter, as it turns out, is the thickness of inlet endwall boundary layer. A much improved prediction is obtained as shown in Figure 4.7b. The significant unloading effect can now be well captured at 95% span, agreeing with the experiment.

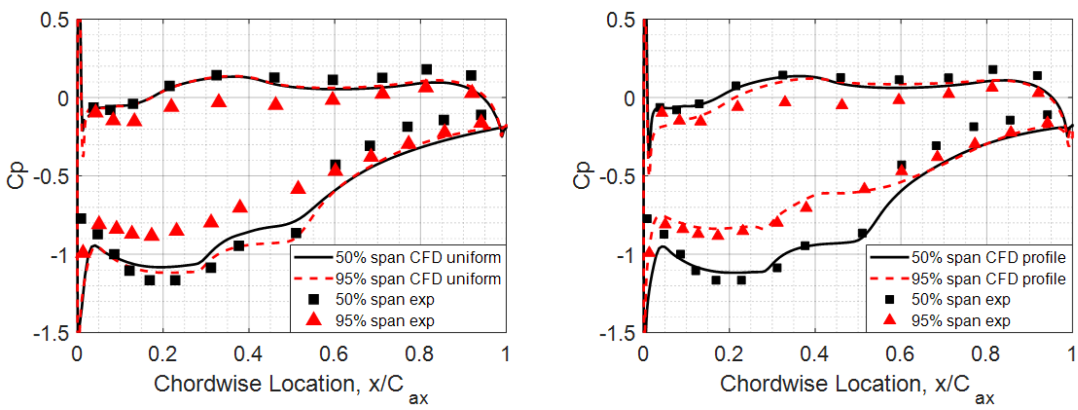

(a) Uniform inlet **(b)** Profile inlet

Figure 4.7: Cp distributions for different inlet BL thickness.

4.2.4 Effect of Tip Clearance

In the experiment, the tip clearance is changed by relocating the blade relative to the perspex endwall in the spanwise direction, while the pressure tapping locations and the cascade casing are fixed. Hence, the percentage span is defined as the location of the pressure tapping relative to the original blade span. The same definition is used in the simulations for tip clearance cases for consistency.

Figure 4.8 presents the steady pressure distributions at 95% span for different tip gaps. Again the results with the profiled inlet (Figure 4.8b) and those with the uniform inlet (Figure 4.8a) are contrasted. There are three regions of surface pressure variations with the tip clearance, to be noted firstly from the experimental data.

i The frontal region from the leading edge to 25% chord. This is the part where the pressures on the suction surface increases (off-loading) when the tip gap increases;

ii The region between 25% and 50% chord. Here the pressure variation is opposite to that of the frontal part. The pressure decreases (up-loading) when the tip gap increases;

iii The rear part from 50% chord to the trailing edge. In this region, the pressures vary non-monotonically with the tip gap. They first increase (off-loading) when the tip gap increases from 0% to 1%. Then when the tip gap further increases from 1% to 2%, the pressures in this rear part decrease (up-loading).

More relevantly to the present interest, we note that the steady pressure variations with the tip gap are well predicted when the inlet end wall boundary profile is introduced (Figure 4.8b). The correct trends for all three regions are well captured in agreement with the experiment, though the detailed distributions in the rear region, particular at the largest tip gap (2%) can only be regarded as fair, which should be reasonably expected given the complexity of the corresponding leakage flow.

On the contrary, the pressures predicted with the uniform inlet are in serious errors in the overall loading for all tip gaps (Figure 4.8a). Furthermore, for the rear

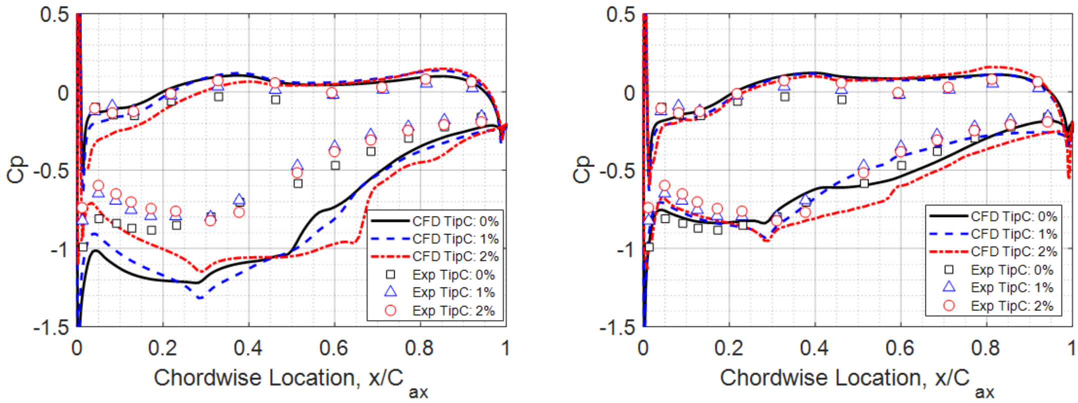

(a) Uniform inlet

(b) Profile inlet

Figure 4.8: Steady surface pressure distributions at 95% span with different tip clearance gaps.

part of the suction surface, the pressure distributions even have a different trend of variation with the tip gap, compared to the experimental one.

4.3 Unsteady Flow Results

4.3.1 Aeroelastic Damping of Tuned Cascade

The unsteady results show here are for the 3D configurations with varying tip gap. The mode of vibration is bending, similar to that executed in the experiment where the validation data was recorded. Figure 4.9 shows the overall damping at reduced frequency $k = 0.2$ and 0.4. The reduced frequency k is defined as:

$$k = \omega C / V_{ref} \tag{4.8}$$

where ω is the vibration frequency, C is the blade chord, and $V_{ref} = \sqrt{2\left(P_{01} - P_2/\rho\right)}$ is the reference isentropic exit velocity. The CFD results are in good agreement with the experiment. The least stable IBPA lies in the forward travelling wave mode, at about 20^0 to 30^0 of IBPAs. Both computational and experimental aero-damping curves seem to follow the trend that as the reduced frequency k decreases, the damping curve moves downward (towards the instability zone) and rightward (towards the forward travelling wave mode zone). This is also in line with the industry experience in the way that the reduced frequency k can be increased by increasing the blade chord and/or the blade thickness to improve the aeroelastic stability.

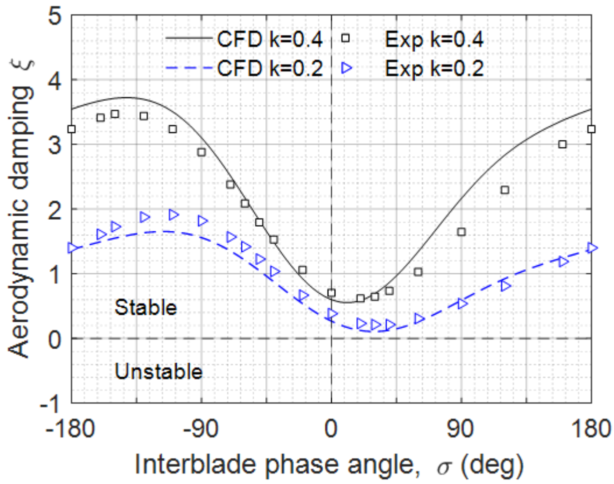

Figure 4.9: Overall aerodynamic damping at $k = 0.2$ and 0.4.

4.3.2 Aeroelastic Effect of Separation Bubble

The laminar separation bubble on the suction surface in the middle span region has been shown to affect the local steady pressure distribution on the suction surface. In this section, its effects on the aeroelastic stability are examined by comparing the results on the 2D mid-span section. To illustrate the aeroelastic stability variation with both the chordwise location and IBPA, we choose the local aero-damping contours on an x-σ map, as shown in Figure 4.10.

The fully turbulent model (Figure 4.10c) produces a continuously smooth local damping distribution on the suction surface for an entire range of IBPA. The transitional model (Figure 4.10b) shows strong variations in local damping distribution around the laminar separation reattachment point around 65% chord (marked by a dash line in the figure). The local damping variations as shown reflect the locations of the bubble separation formation and the reattachment at around 30% and 60% chord. The transitional model can predict qualitatively the effects of the laminar separation bubble compared to the experimental results shown in Figure 4.10a. The fully turbulent model completely misses this behaviour (Figure 4.10c). The pressure surface is shown to be insensitive to the bubble separation formation, hence its local damping distribution remains unaffected regardless of the turbulence model choice.

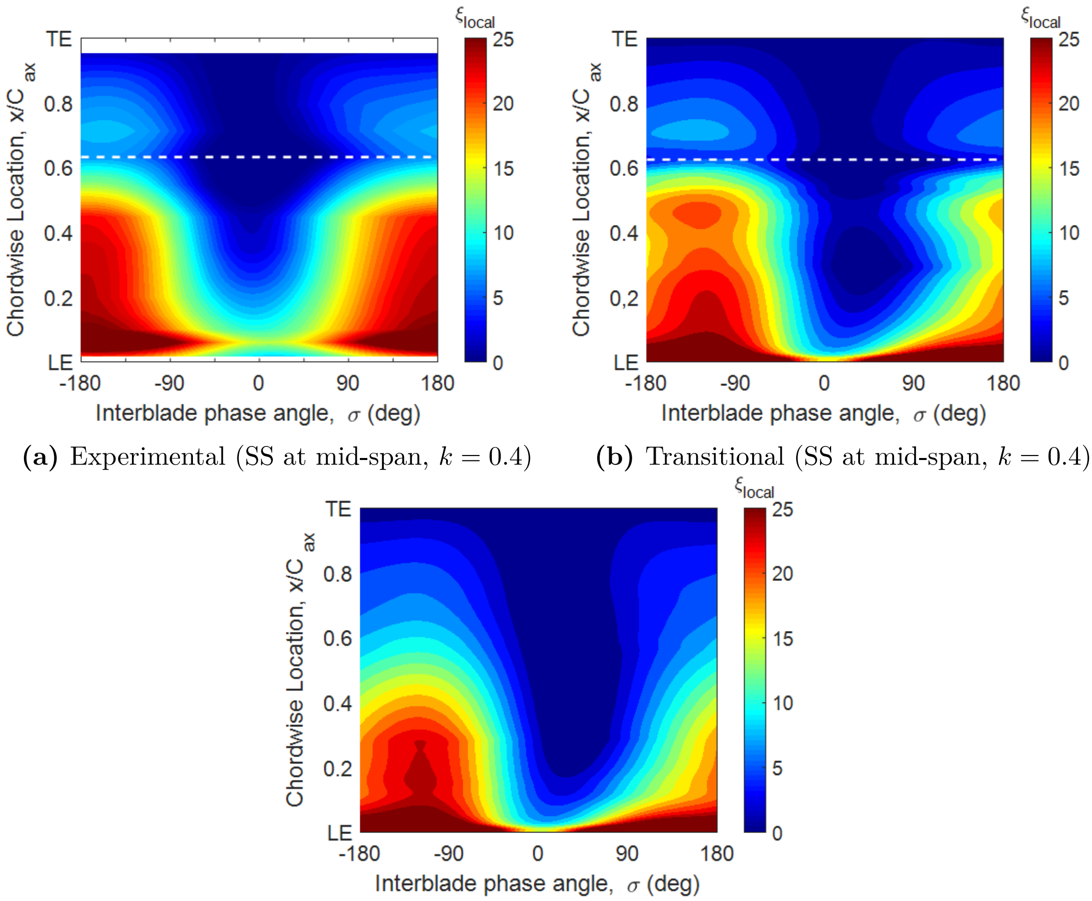

(a) Experimental (SS at mid-span, $k = 0.4$) **(b)** Transitional (SS at mid-span, $k = 0.4$)

(c) Fully turbulent (SS at mid-span, $k = 0.4$)

Figure 4.10: Local damping contours (on x/C-IBPA plane) for suction surface at mid-span (transitional and fully turbulent models vs experimental results).

Figure 4.11 shows the overall damping at the mid-span section calculated by taking integrations along the blade chord. Despite the marked difference in local damping on the suction surface between the transitional and fully turbulent models, the overall damping values over the entire chord are not significantly affected, particularly in the IBPA regions with a minimum damping. Therefore, for the present case the suction surface laminar bubble separation does seem to be insignificant.

The present observation is also in line with the previous finding for an oscillating turbine cascade configuration, for which the bubble-type flow separation on the suction surface was shown to have relatively a small influence on the overall aerodynamic damping, both experimentally and computationally [L. He, 1998a; L. He, 1998b].

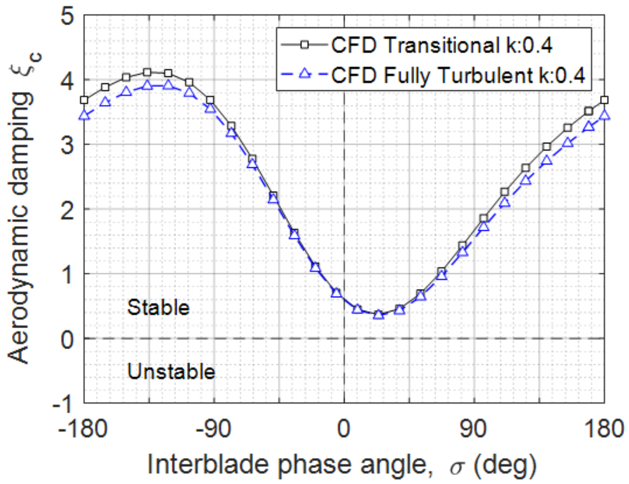

Figure 4.11: Overall aerodynamic damping at 2D mid-span $k = 0.4$ for transitional and fully turbulent models.

4.3.3 Aeroelastic Effect of Tip Clearance

Overall Aero-Damping Variation with Tip Gap

Figure 4.12 shows the effects of tip clearance on the overall damping. It can be seen that the least stable damping decreases as the tip gap increases. The least stable IBPA remains almost the same, to be about 20-30 degrees. The predicted destabilizing trend of increasing tip clearance is captured qualitatively across the entire range of IBPA, compared to the experiment. When the tip gap increases from 0% to 2%, the calculated minimum damping is decreased by about 27%. From the experiment, the minimum damping was also reduced by about 27% compared to that at the nominal zero tip-gap condition. This is a quite considerable damping reduction considering how much the damping is decreased when the reduced frequency k is halved from 0.4 to 0.2 as shown in Figure 4.9, although the very quantitative agreement with the experiment should not be taken to reflect a typical level of accuracy to be expected.

A close inspection of the minimum damping values at the least stable IBPA is taken as shown in Figure 4.13. It can be seen that the computations with the uniform inlet condition predict a rather insignificant reduction in the minimum damping when the tip gap is changed from 0% to 2% span. However a marked

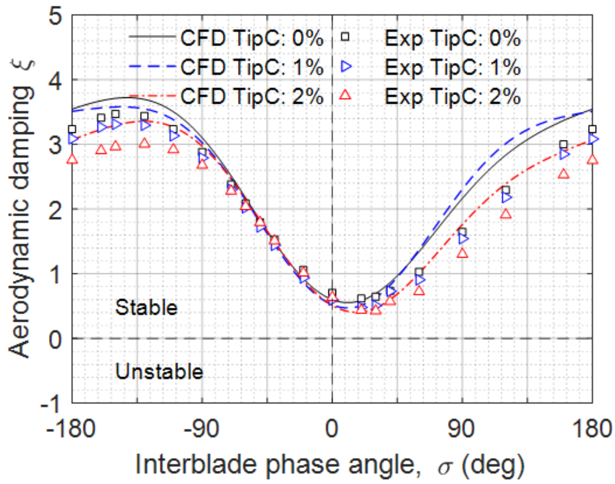

Figure 4.12: Overall aerodynamic damping at $k = 0.4$ for different tip clearance settings.

reduction of the damping with the tip clearance is observed in the CFD with the inlet endwall boundary layer profile, predicting about a damping drop of about 27% with the increase of the tip clearance, in good agreement with the experiment.

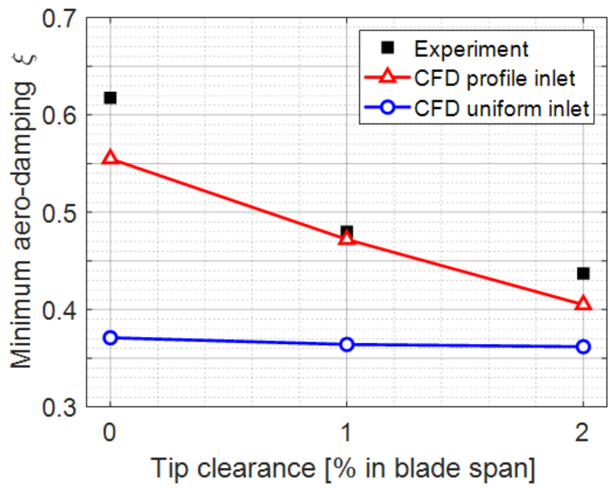

Figure 4.13: Minimum damping at least stable IBPA.

Local Aero-Damping and Quasi-Steady Analysis

To help understand the underlying flow physics that drives the aero-damping characteristics, we now examine the local damping distributions on blade surfaces. The main attention is directed to the blade suction surface where major contributing factors are at play when the tip clearance is changed. Figure 4.14) shows the local damping contours on the suction surface at two tip clearances. Two distinctive regions are noted.

i The bulk frontal part (marked as '***A***' in Figure 4.14) from the leading edge to about 30% chord, and for most of the span from the tip down to nearly 20% span. This is a region with a strong stabilizing effect regardless of the tip gap.

ii The rear part from 30% chord to the trailing edge in the tip region (marked as '***B***'). This is the part where the destabilizing effect of the tip clearance and its increased strength at a larger tip gap are clearly identifiable.

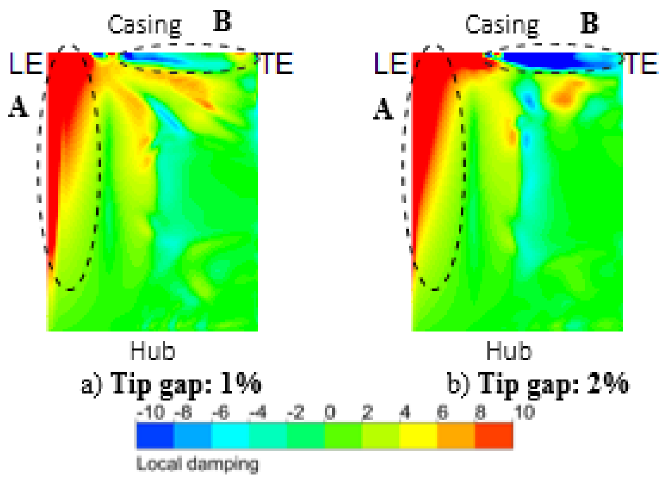

Figure 4.14: Local damping on suction surface at two tip gaps.

The bulk frontal part "***A***" is deemed to be largely independent of the tip gap as the affected stabilizing area stretches well into the mid-span and beyond. A following simple quasi-steady analysis may be used to explain the behaviour.

The bending displacement in the y-direction normal to the chord and the corresponding unsteady aerodynamic force on the blade in this direction f can be expressed as:

$$y = A_y \sin(\omega t) \tag{4.9}$$

$$f = A_f \sin(\omega t + \varphi_f) \tag{4.10}$$

At the mean position with $\omega t = 0^0$ (shown in Figure 4.15a), the vibratory velocity V_y in the y-direction is at its maximum. Given the absolute inflow velocity V_1, the velocity diagram would give a relative velocity (W_1) corresponding to a negative incidence. Thus, the leading edge portion of the blade is off-loaded, leading to a higher local pressure near the LE on the suction surface. In terms of the blade force in y-direction, this local high pressure peak on the suction surface should correspond to a negative contribution to the blade force in the y-direction. Thus the corresponding unsteady force has a 90^0 phase lag (i.e. $\varphi_f = -90^0$. This part then has a positive damping contribution. Hence we can see that the bulk frontal part is predominantly subject to a stabilizing incidence effect localized around the leading edge.

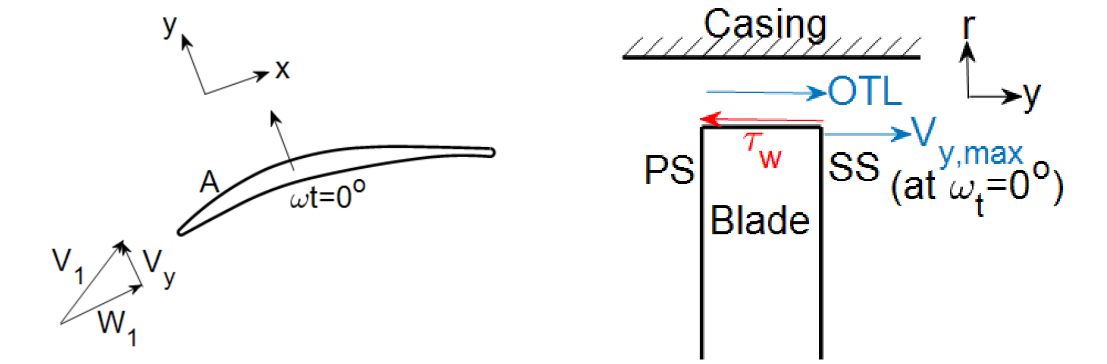

(a) LE incidence effect (for frontal region 'A') **(b)** Tip motion effect (for rear tip region 'B')

Figure 4.15: Quasi-steady analysis illustration for the tip regions 'A' and 'B'.

For the rear part near tip (marked as '***B***' in Figure 4.14), the negative damping has an apparent signature of the tip leakage. Once again, a quasi-steady analysis may be used. Basically, the over-tip leakage ('OTL') flow is driven by the pressure difference between pressure and suction surfaces. The leakage flow is also resisted by the shear stresses from the tip and casing surfaces. For the oscillating blade, we focus on the wall friction shear stresses on the over-tip surface (τ_w in Figure 4.15b). The tip vibratory motion can enhance or suppress the leakage flow, depending on the velocity of the movement. At the mean position ($\omega t = 0^0$), the tip velocity (V_y) is at its maximum in the direction from the pressure surface to the suction one (Figure 4.15b). An increase in the surface velocity should lead to a decrease in the velocity gradient (thus a drop in shear stress τ_w). Correspondingly at this moment with a minimum friction on the tip surface, the tip leakage flow should be roughly at its highest. Recall the steady pressure distributions near the tip at different tip gaps discussed earlier. For the rear portion of the suction surface, an increase in the tip leakage flow would correspond to a decrease in local pressures (up-loading) when the tip gap is increased from 1% to 2% (Figure 4.8b). Thus at $\omega t = 0^0$, we have the minimum pressures on the rear suction surface, i.e. the local pressures lag the blade movement by 90^0. The corresponding local suction force contribution to the overall unsteady force would have a 90^0 phase lead (i.e. $\varphi_f = 90^0$ in Equation 4.10). Therefore, we should expect a local negative damping contribution in the rear tip region '$\boldsymbol{B}$' due to the tip clearance, as observed.

Balancing Tip Leakage Vortex with Passage Vortex

Finally some further understanding on the marked impact of inlet endwall boundary layer profile can be gained by considering the interaction between two main vortices (passage vortex and tip leakage vortex) in a blade passage. Shown in Figure 4.16 are velocity vectors and vorticity contours on several axial cut planes for the case with a uniform inlet. The corresponding results for the case with the inlet boundary layer profile are shown in Figure 4.17.

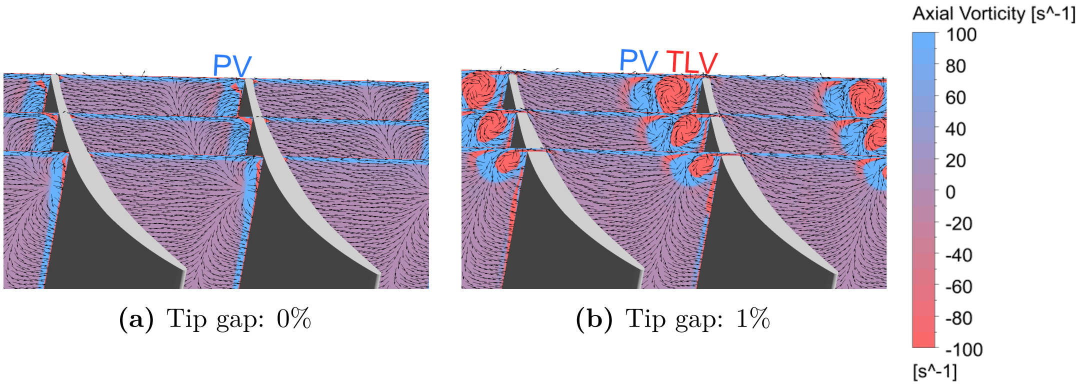

(a) Tip gap: 0% **(b)** Tip gap: 1%

Figure 4.16: Evolution of TLV and PV with **uniform inlet** (velocity vectors and vorticity contours on axial cut planes).

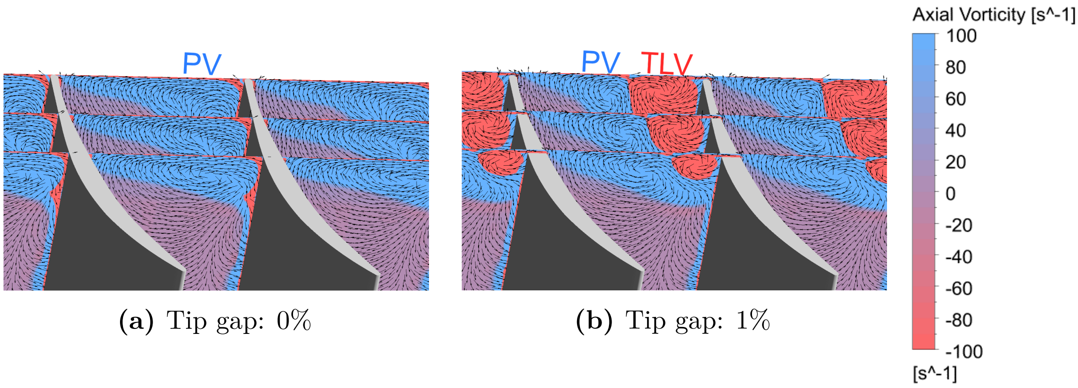

(a) Tip gap: 0% **(b)** Tip gap: 1%

Figure 4.17: Evolution of TLV and PV with **profile inlet** (velocity vectors and vorticity contours on axial cut planes).

The flow with zero tip clearance (Figure 4.16a and Figure 4.17a) should serve as a baseline before the tip clearance effect is examined. A strong passage vortex (PV) is seen under the condition of the inlet endwall boundary layer (Figure 4.17a). On the other hand for the uniform inlet case (Figure 4.16a), the passage vortex is rather weak and not easily identifiable. This is in line with previous research findings that a thicker inlet endwall boundary layer would more effectively promote the cross-passage flow from the pressure surface to the suction surface [Zhang et al., 2014]. This strong secondary flow is mainly responsible for the off-loading near the tip as observed in the measured steady pressures as shown in Figure 4.8b (noting that the off-loading exists for the zero tip gap).

When the tip clearance is introduced, the base flow setup by the passage-vortex is noticeably changed near the suction surface side. The secondary flows near the pressure side remains similar to the cases at the zero tip gap. Now the tip leakage vortex (TLV) seems to be more compact with the uniform inlet flow (Figure 4.16b) than that with the inlet endwall boundary layer (Figure 4.17b).

In the case of the uniform inlet, there is far less off-loading near the endwall when the tip gap is increased, as seen in the pressure distributions (Figure 4.8a). This might be largely attributed to that the base flow responsible for the near tip off-loading is chiefly set up by the passage vortex associated with the secondary flow. And in this case, the two qualitatively different base flows are set up by the two different inflow conditions.

The different base flows may also explain the seemingly different sizes of the tip leakage vortices (TLV) between the two cases. The TLV for the uniform inlet is not strongly mixing out with the primary stream which has much higher velocity/inertia, and appears to be more confined (Figure 4.16b). On the other hand, the TLV seems to interact more strongly with the passage vortex as the base flow is now subject to much stronger cross-passage secondary flow (a weaker primary flow). As a result, the TLV in this case appears bigger (Figure 4.16b).

Overall, the interaction and balance between the TLV and the PV are shown to have important effects on the blade loading near the endwall. The close link of the relative strengths of the two primary vortices to the inlet endwall boundary layer thickness can now be clearly seen. Thus one should not be surprised that different inlet endwall boundary layer thickness can lead to qualitatively differences in blade loading and subsequently aero-damping characteristics in the tip region.

4.4 On Validity of Influence Coefficient Method

4.4.1 Specific Issues of Interest

In the first part of this study, the direct periodicity was adopted in the ICM model to investigate the tip clearance effects in a compressor cascade. Due to the periodic interfaces in the computational model, the flow field is spatially periodic. However, in a practical experimental setup, the cascade configuration has a finite number of blades subject to upper and lower sidewalls as illustrated in Fig. 1 whether the cascade is of linear or sector annular type. With the presence of tunnel sidewalls, the spatial periodicity is more difficult to achieve, particularly for the outermost blades. In an experiment, a better flow field periodicity and uniformity can be managed by a combination of treatments such as wall suction and tailboard angles alignment. CFD modelling of these additional effects is complicated and not covered in this current work. Hence, the validity of the influence coefficient method in a conventional setup representing a realistic experimental configuration is what we are concerned about. In this part, the tunnel sidewalls are modelled as the inviscid-slip wall from the inlet to the leading edge station to avoid the ambiguity of blockage effects due to the build-up of boundary layers in this region. At the lower and upper boundaries of the tunnel sidewalls, the no-slip wall condition is applied.

There are two basic assumptions of the ICM for a linear (or an annular sector) cascade bounded by two sidewalls:

1. The cascade contains a sufficient number of blades so that the unsteady pressures on the furthest blades from the middle oscillating blade will be of a negligible amplitude. This is required for the convergence of the influence coefficients summation based on the finite number of blades in the cascade (Eq. 4.2);

2. A linear behaviour of the unsteady pressures induced by the middle oscillating blade, thus the validity of superposition.

Regarding the first aspect, the decay of unsteady pressure responses of blades with its distance from the oscillating blade is required. The number of blade passages required for getting an adequate result for tuned cascade is indicated by the decaying rate of the unsteady disturbances away from the middle blade. This effectively corresponds to how fast the summation of influence coefficients would converge, thus it may be called the ICM "convergence" characteristics. Figure 4.18 shows the corresponding aerodynamic damping components contributed from each blade in the cascade with the middle oscillating blade B0. The convergence characteristics shown in Figure 4.18 suggest that only the oscillating blade (B0) and two immediate blades at the vicinity to its suction surface and pressure surface (B+1 and B-1) are significant in the aero-damping calculation. Hence, the ICM computational model with five blades is deemed reasonable for the present case.

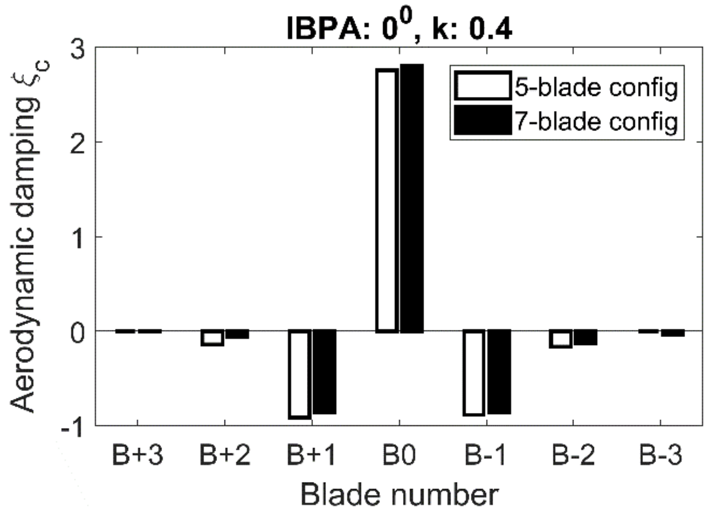

Figure 4.18: Contributions of influence coefficients from the blade B0 and its neighbouring blades (IBPA=0^0 and $k = 0.4$).

The second aspect is the linearity assumption. A test of the linearity is carried out by comparing the unsteady pressure responses computed at two bending oscillation amplitudes, 6%C and 3%C and that measured from the experiment at mid-span, as shown in Figure 4.19. The first harmonic pressure amplitude distributions calculated using the ICM model from the two amplitudes are almost identical, except near the leading edge and the separation bubble region. Similar observation is also made from the experimental results. Hence, despite of a marked local nonlinearity due to the laminar separation bubble, its overall contribution to the aero-damping is deemed to be negligible for this case.

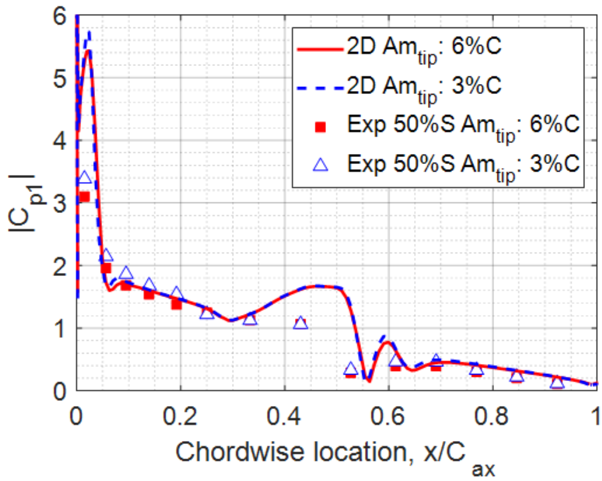

Figure 4.19: Unsteady pressure responses on the suction surface of blade B0 in subsonic regime for two bending amplitudes.

Having examined the validity of the two common assumptions, we now turn our attention to the sensitivity and implications of the far-field conditions, as the main focus of this section. It is worth noting that the ICM-based data from a linear or annular sector cascade are commonly used to generate tuned cascade data for an entire range of IBPAs (e.g. Figure 4.12). As such it seems to be taken for granted or implied that a standard tuned cascade model where all blades are oscillating in a travelling wave mode (TWM) should be directly comparable to an ICM-generated tuned cascade results at any IBPA. A question to be asked is that in addition to the basic assumptions as examined above, *is there any other* *factor at play in terms of the validity and applicability of the influence coefficient method in a linear or annular sector cascade set up?*

It is observed that the present ICM-based damping variations with IBPA all seem quite smooth and sinusoidal. However, LINSUB [Whitehead, 1987], a 2D semi-analytical code for unsteady flows past a tuned flat plate cascade, shows clearly unsmooth aero-damping curves, as seen in Figure 4.20. These spikes are due to the dynamic behaviour of the inlet and outlet ducts rather than flow physics inside the bladerow. The spikes in the unsteady responses happen around a resonance condition of an annular duct acoustic mode corresponding to a certain circumferential wave length and travelling speed (thus frequency and IBPA). Given these very contrasting observations we would like to further examine the sensitivity of the two models (TWM vs ICM) to far-field inlet and outlet treatments.

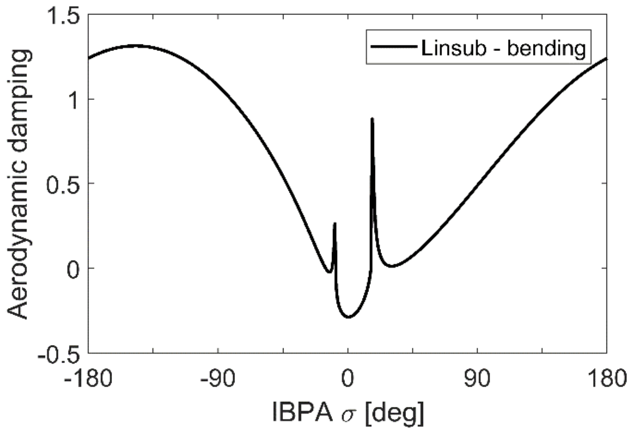

Figure 4.20: Aero-damping variation with IBPA for tuned cascade as predicted by LINSUB (bending mode, $k = 0.6$).

The annular duct acoustic resonance conditions can be estimated based on Equation 4.11 [Whitehead, 1987]. The phase angles that cause acoustic resonance satisfy the conditions that the waves carry energy in a purely circumferential direction, so no energy is lost by radiation in an axial direction. For a subsonic flow, Equation 4.11 gives two discrete angles, a negative σ_R^- and a positive σ_R^+ resonance IBPA phase angle. The flow is cut-on i.e. the acoustic waves propagate when the IBPA is in the range, $\sigma_R^- < IBPA < \sigma_R^+$. M, M_x, and M_y are the total, axial, and circumferential Mach numbers, respectively. k is the reduced frequency and S/C is the pitch-to-chord ratio.

$$\sigma_R = \left(M_y \pm \sqrt{1 - M_x^2}\right) Mk\,(S/C)\,/\left(1 - M^2\right) \tag{4.11}$$

4.4.2 Test Configurations and Conditions

In order to examine the sensitivity of aeroelastic response of the cascade to the far-field treatment, the domain duct lengths are varied to alter the acoustic behaviour of the system. The inlet and outlet duct lengths are increased to about 2C and 5C, respectively. The extended long duct domain is covered with a coarse mesh stretched in the axial direction with an extra numerical damping effect on the far field.

The Fourier Transformation method implemented in CFX in a double-passage domain with the phase-shifted periodicity is used for TWM simulations. In this method, the flow history on the phase-shifted periodic boundaries are stored and reconstructed using Fourier series based on the work of He [1990].

4.4.3 Low-speed Cases

Figure 4.21 presents the overall damping of configurations with different duct lengths predicted by both the influence coefficient method and the tuned cascade model. At this low Mach number, the acoustic resonance is estimated to occur between $\sigma_R^- = -1.4^0$ and $\sigma_R^+ = +1.6^0$ based on Equation 4.11. The computations of both ICM and TWM seem not to be able to capture the acoustic resonance and the overall damping curve is largely smooth and sinusoidal.

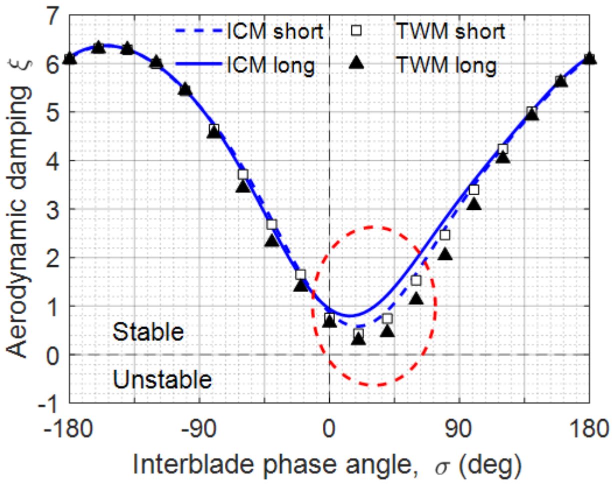

Figure 4.21: Overall aerodynamic damping for different configurations at low-speed condition.

When the duct lengths are extended, the minimum damping changes by +36% for the ICM model and -31% for the TWM model. Importantly, the ICM and TWM models respond in an opposite way when the duct length is extended. The ICM model is shown to be more stabilizing, whereas the TWM model is shown to be more destabilizing as the duct length is extended.

Figure 4.22 presents the first harmonic unsteady pressure amplitudes for both the ICM and the TWM models with different duct length configurations at the forward travelling wave mode IBPA 30^0 and 180^0, respectively.

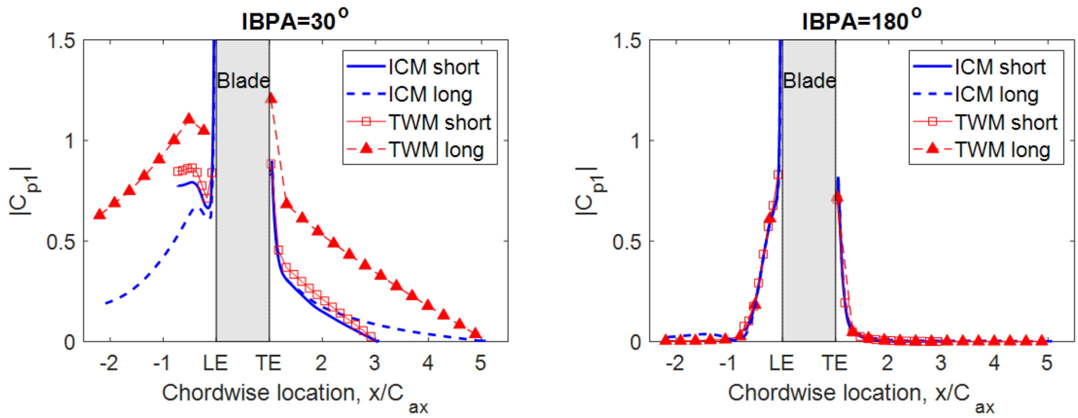

(a) IBPA $\sigma = 30^0$ (b) IBPA $\sigma = 180^0$

Figure 4.22: Far- and near-field pressure amplitudes for different ICM and TWM model configurations at low-speed.

At IBPA 30^0 (Figure 4.22a), the far-field seems to be a cut-off but with a slow decaying rate of the pressure amplitude. There are some notable features for this case. Firstly the difference between different models are relative small for the short duct. But there are much larger differences between the two models for the long duct domain case. Interestingly, the ICM results for the long duct are rather similar to those of the short duct. On the other hand, the substantially different far-field acoustic behaviour of the tuned cascade model leads to a significant mismatch between the overall damping predicted by the ICM-generated and the TWM-based tuned cascade model (Figure 4.22a). Thus the tuned cascade model (TWM) is shown to be much more sensitive to the far-field treatment, at this IBPA condition.

In contrast, the case at IBPA 180^0 (Figure 4.22b) represents a well cut-off scenario with a very fast decaying rate. In this case further away from the acoustic resonance condition, the first harmonic unsteady pressure amplitudes in all configurations decay quickly to zero when approaching inlet and outlet far-field. As a result, the overall damping predicted by all configurations at IBPA 180^0 are almost identical.

A key observation from the above comparisons is the strong IBPA dependence of the sensitivity. It is worth underlining that the corresponding computations for the two IBPAs are carried out with completely consistent mesh resolution, numerics, boundary conditions and turbulence modelling. This serves as a useful example to highlight that extra care should be taken when comparing results between a tuned cascade (TWM) model and a linear cascade based ICM model, especially at conditions close to an acoustic resonance.

4.4.4 High-speed Cases

The experimental rig is in a low-speed regime. Although we have had some useful observations, it would be naturally of interest to ask what we should expect in its high speed counterpart with seemingly more nonlinear transonic flows.

To address this, the current cascade is further studied numerically in a high-speed regime by reducing the static pressure at outlet ($P_2/P_{01} \approx 0.82$). The maximum isentropic Mach number of the blade is about 1.0 - 1.1 on the suction surface as shown in Figure 4.23.

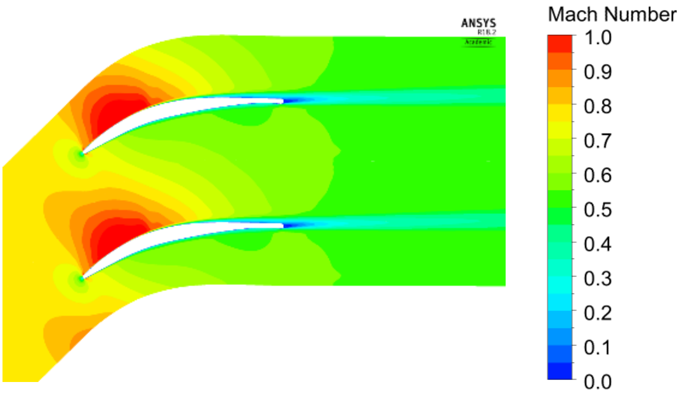

Figure 4.23: Far- and near-field pressure amplitudes for different ICM and TWM model configurations at low-speed.

At this practically transonic flow condition, the linearity assumption of the ICM model is examined by considering various bending oscillation amplitudes: 1%C, and 0.5%C. The unsteady pressure responses show a bump in the first harmonic unsteady pressure amplitude on the suction surface, at the location where the isentropic Mach number enters the transonic regime. Comparisons of the unsteady pressure coefficients of the central oscillating blade for the ICM method (Figure 4.24) show that this transonic bump is sensitive to the bending amplitude, and hence an indication of nonlinearity. At the small bending amplitudes (<1%C), the flow is largely linear. As the bending amplitude increases, the non-linearity increases as can be seen from the unsteady pressure responses at a bending amplitude 3%. For practical high speed flutter predictions, this large amplitude is deemed to be too big. An amplitude of 1% or less would be deemed to be more appropriate. Therefore, for a given small oscillation amplitude, we can say that the linearity assumption of the ICM model should still hold even when the flow field enters a transonic regime.

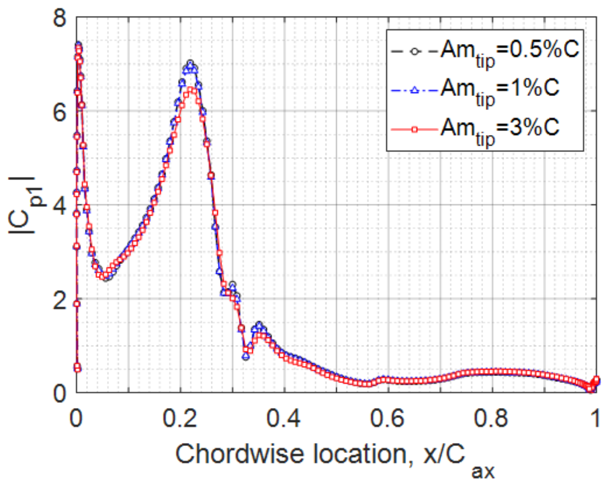

Figure 4.24: Unsteady pressure responses on the suction surface of the central blade B0 at high-speed condition.

On the numerical convergence, the travelling wave mode simulations at a high speed tend to be more difficult to achieve convergence to a periodic state. Additional numerical damping has to be applied for the high speed cases to remove numerical noises from a solution. It is noted that when a strong numerical damping is applied, the acoustic response in the far-field can also be damped significantly, and the overall damping can become smooth and sinusoidal as seen in the influence coefficient method for the low speed case. A similar effect of the numerical damping has been observed when the numerical boundary conditions can be regularized near acoustic resonance, such that the singularity behaviour near the acoustic resonance can become smoother [Frey and Kersken, 2016].

Figure 4.25 presents the overall damping variation with IBPA for different configurations by both the ICM and TWM methods. At this high Mach number condition, the acoustic cut-on condition is estimated to occur between $\sigma_R^- = -8.5^0$ and $\sigma_R^+ = +34.8^0$ based on the theoretical prediction (Eq. 4.11). The damping results of the TWM models seem to be more different from each other as well as from those of the ICM, particularly in the cut-on region bounded by two acoustic resonance IBPAs, indicating a higher sensitivity.

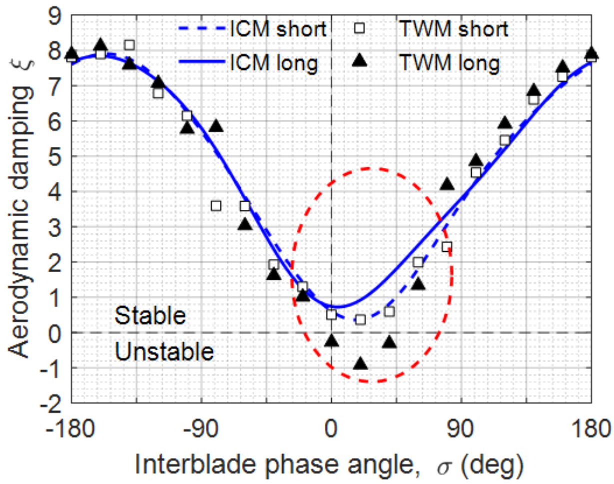

Figure 4.25: Overall aerodynamic damping for different configurations at high-speed condition.

Similar to the case of the low speed flow, the ICM and TWM models are shown to respond very differently when the duct length is extended. The minimum damping is increased by +101% for the ICM model. But for the TWM model, the minimum damping is reduced substantially. In fact the TWM solution damping becomes negative when the large duct domain is used. It is worth noting that the IBPA range with the largest discrepancies correspond to the cut-on region bounded by the acoustic resonance conditions.

The results of the high-speed case reinforces the observation from the low-speed test case. The unsteady flow response is still largely linear. There is a strong IBPA dependency of the damping comparison between the two models of interest. The sensitive regions are around the cut-on IBPAs range with relatively low aero-damping.

4.4.5 Further Discussion

The present computational studies indicate that the linear assumption of the ICM model is largely adequate for a range of flow conditions of practical interest, even in a transonic flow. So the influence coefficient model per se seems to be largely valid, at least as shown for the present cases tested.

However, we do see considerable differences in the results between the influence coefficient model as in the practical linear cascade experimental setup and the tuned cascade model. The differences are clearly dependent on IBPA for a given frequency. The prevailing factor causing the differences seems to be attributed to the inherent different far-field behaviour, manifested by that a tuned oscillating cascade model can excite an acoustic resonance in an annulus duct. On the other hand, the presence of tunnel sidewalls in a linear or annular sector cascade experiment will clearly affect the circumferential travelling waves. The pressure waves would reflect off the tunnel sidewalls and feedback to the main flow field. This would ultimately affect the behaviour and sensitivity of the corresponding influence coefficient model to far-field conditions compared to its tuned cascade model counterpart.

It is also meaningful to make a distinction between the validity of the ICM model itself, and the applicability of the ICM for practical purposes. The present observations suggest that care should be taken when comparing the results between the ICM based on a linear cascade or annular sector cascade experiment and a tuned cascade TWM model for validation purposes.

In many cases, ICM-based experimental data are intended to be used to validate the near-field physical and numerical modelling aspects for oscillating blade rows (e.g. mesh, turbulence modelling, temporal and spatial discretization, geometrical modelling, unsteady viscous flow physics etc). In this case, caution should be exercised when comparisons with a tuned cascade model are made, particularly at conditions when the near-field bladerow unsteady aerodynamics and the aero-damping are highly sensitive to the far field acoustic behaviour and treatment.

4.5 Summary

This chapter consists of two main parts. In the first part, the unsteady CFD solver for oscillating blades as implemented in the solver CFX has been validated against the detailed 3D experimental data of an oscillating compressor cascade. This is one of only few validation studies against detailed 3D unsteady aerodynamic experimental data available in the public domain. The following observations can be made:

1. The tip clearance is shown to have a destabilizing effect on the aeroelastic stability for the present compressor cascade, in agreement with the experiment.

2. There is a distinctive interplay between the inlet endwall boundary layer and the tip clearance in relation to the aerodynamic damping. Qualitatively different aeroelastic characteristics of tip clearance are observed when subject to different inlet endwall boundary layers.

3. The laminar bubble separation on the suction surface has a clear signature in the local aerodynamic damping distribution. However, it yields an insignificant effect on the overall damping.

In the second part, the validity and applicability of the influence coefficient method (ICM) in a linear cascade setup are examined, leading to the following observations:

1. The unsteady flow response in this cascade is predominantly linear for both low speed and high speed transonic conditions. The present results support the validity of the ICM model per se.

2. The main difference between the ICM and the tuned cascade model arises from the inherently different far-field acoustic behaviour. This leads to distinctively different sensitivities of the two models to far-field conditions and treatments. Therefore, cautions should be exercised when using a linear cascade based ICM for validation purposes. We should not expect to reproduce the tuned cascade results over an entire inter-blade phase angle range from the ICM-based experimental data, particularly around the IBPA conditions when the far-field acoustic behaviour becomes strongly influential.

5

Effects of Structural and Aerodynamic Mistuning

Contents

In this chapter, the fundamental vibration characteristics of a mistuned cascade will be investigated using the fully-coupled fluid-structure simulation method. The aeroelastic effects of mistuning will be also studied. The characteristics and effects of the structural mistuning and the aerodynamic mistuning are compared to each other.

5.1 Test Case Descriptions

The control-diffusion compressor blade geometry used in the previous validation chapter is used in this study of mistuning effects. The simulation domain is a two-dimensional cascade with 12 blade passages and periodic lateral boundaries. The baseline flow conditions of the tuned cascade are the same as that in the validation chapter. Figure 5.1 shows the mesh adopted in the present line of work.

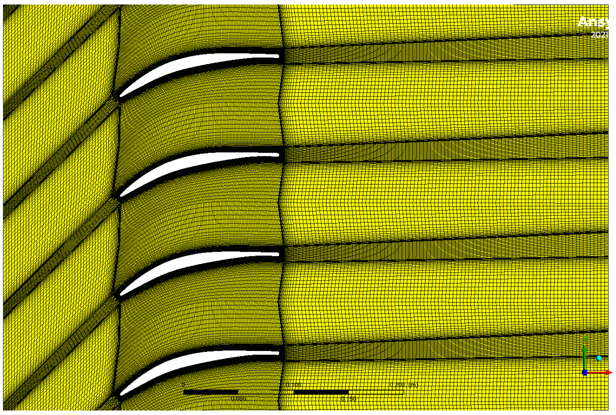

Figure 5.1: Mesh of the two-dimensional cascade.

To simulate the structural mistuning effects, the blade eigen-frequencies are modified via their blade stiffnesses. On the other hand, aerodynamic mistuning effects are simulated via the change in their stagger angles. Figure 5.2 illustrates the convention of negative/positive mis-staggered blade in the aerodynamically mistuned cascade. Because mis-staggering would change the blade steady aerodynamic conditions, it is necessary to investigate its effect on the steady aerodynamic characteristics.

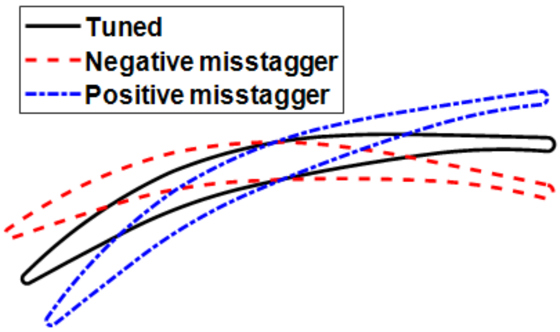

Figure 5.2: Aerodynamic mistuning (mis-staggering) illustration.

Figure 5.3 shows the effects of mis-staggering on the blade steady aerodynamic compared to the baseline tuned cascade (γ_0). For negative mis-staggering (Figure 5.3a), the loading at the leading edge is higher for larger negative stagger angles. This effect can be seen more clearly on the blade suction surface. Because the inflow condition does not change, negative mis-staggering is equivalent to increasing the incidence angle. Thus, the blade loading increases with an increase in negative mis-staggering. On the other hand, positive mis-staggering (Figure 5.3b) induces a decrease in blade loading near the leading edge, although the effects are not as strong as that for negative mis-staggering.

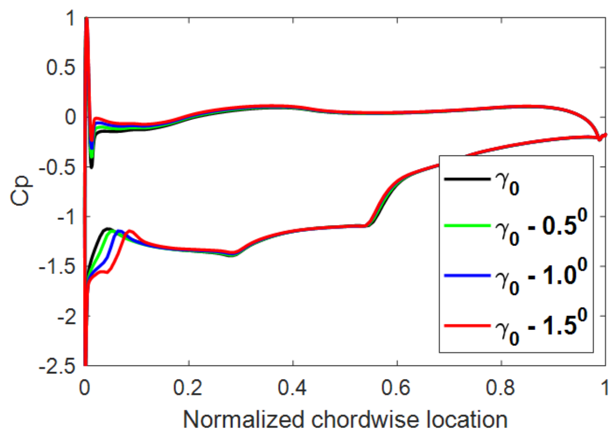

(a) Negative mis-staggering

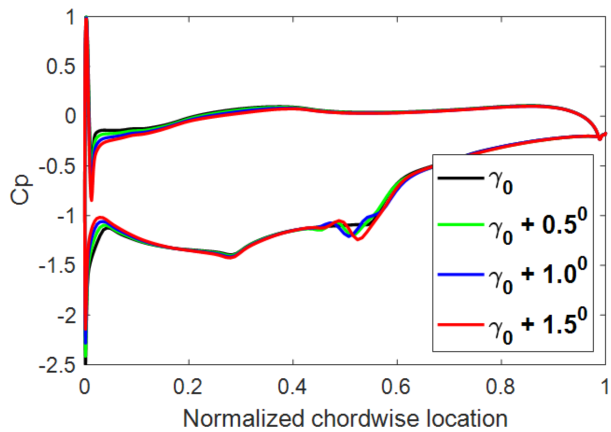

(b) Positive mis-staggering

Figure 5.3: Steady aerodynamic effects of mis-staggering.

Next, the mis-staggering effects on the unsteady aerodynamic of the oscillating blade with torsional mode are assessed in Figure 5.4. Here the blades are still tuned but the stagger angle of all blades are changed simultaneously. Only the small mis-staggering are investigated in this part because the mistuning strength in the present work is relatively small corresponding to the manufacturing tolerances. It can be seen that the negatively mis-staggered configuration has stronger effects on the aerodynamic damping compared to that of the positively mis-staggered configuration. This observation is in line with that observed in the investigation of steady aerodynamic effects. However, the overall effects of mis-staggering on the unsteady aerodynamics of the ***tuned*** cascade are deemed small.

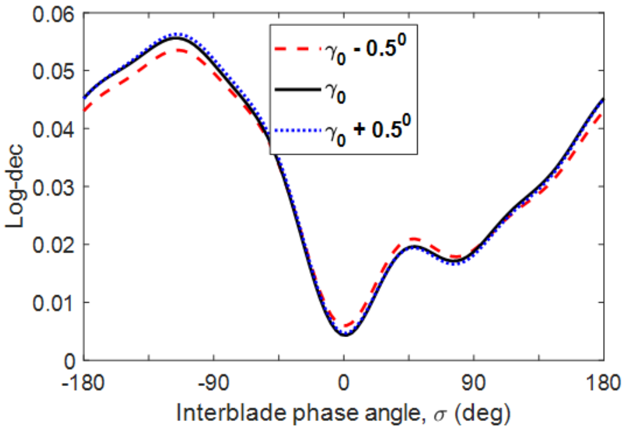

Figure 5.4: Effects of stagger angle on the aerodynamic damping of the tuned oscillating blade in the torsion mode.

In the next section, mistuned cascade will be investigated using the fully-coupled fluid-structure interaction method. The data is post-processed using the methods described in the chapter 3 and the appendix A.

5.2 Validations of Fully-Coupled against Uncoupled Flutter Simulations

The fully-coupled solution of the torsional vibration is validated against the uncoupled solution for the tuned cascade. For validation purposes against the uncoupled method, a high mass ratio $\mu = 800$ is adopted to improve the quasi-periodic vibration of the fully-coupled cascade. These numerical methods should be in good agreement with each other for a high mass ratio configuration, reflecting the suitability of the industry-standard uncoupled solution at a relatively small fluid-structure coupling effect. Figure 5.5 compares the overall damping curve computed by the uncoupled and fully-coupled methods for the torsional vibration mode. Among the uncoupled solutions, there is an excellent agreement between the influence coefficient method (ICM) and the travelling-wave tuned cascade across the entire range of IBPAs. The log-dec is calculated by the fully-coupled method from the successive peaks, whereas the aerodynamic damping calculated from the energy method is converted to log-dec for the uncoupled method. Across an investigated range of IBPAs, the uncoupled and fully coupled methods are well-matched. We note that the local discrepancies between the uncoupled and fully-coupled methods stem from the changing (i.e. decaying or amplifying) vibration amplitude of the fully-coupled solution in contrast to the constant vibration amplitude in the uncoupled method, which is related to the log-dec value. Thus, the local responses at IBPA $\sigma = 0^0$ (minimum log-dec) and IBPA $\sigma = -120^0$ (maximum log-dec) will be further examined.

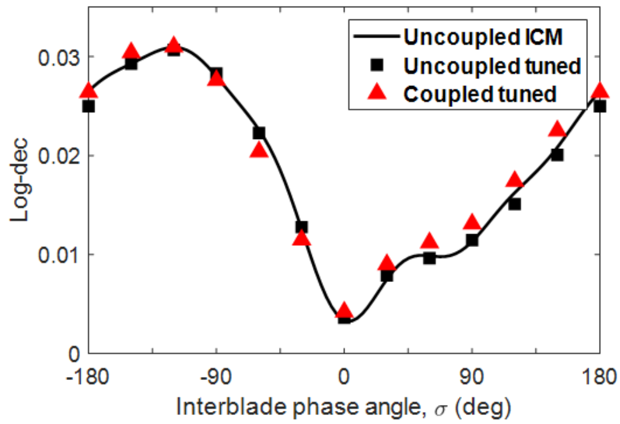

Figure 5.5: Overall damping for torsion mode at $k = 0.8$.

Figure 5.6 presents the unsteady pressure responses at IBPA $\sigma = 0^0$, whereas Figure 5.7 presents that at IBPA $\sigma = -120^0$. An excellent agreement between the predictions by uncoupled and coupled methods is observed at $\sigma = 0^0$. Regarding the case of $\sigma = -120^0$, a general trend is captured by both uncoupled and fully-coupled methods. However, there are still some local discrepancies, such as around 40-60% chord on the suction surface and around 20-40% chord on the pressure surface. At mid-chord on the blade suction surface, there is a laminar separation bubble, followed by the transition to turbulence. From 20% to 40% chord on the blade pressure surface, a laminar separation bubble is formed although no subsequent transition has been observed. At these separated regions, the predictions by the uncoupled and fully-coupled deviate locally from each other. However, these local discrepancies are confined to a rather small area thus its global damping are not significantly affected.

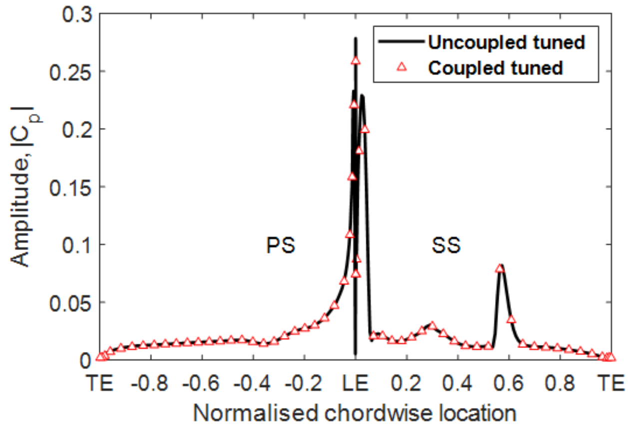

(a) Amplitude

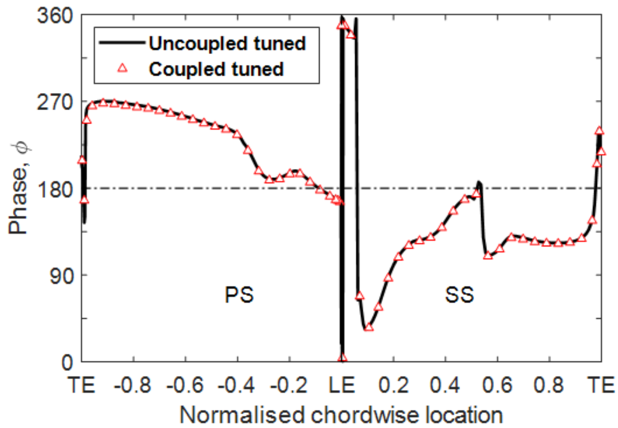

(b) Phase angle

Figure 5.6: Unsteady pressure responses at IBPA $\sigma = 0^0$.

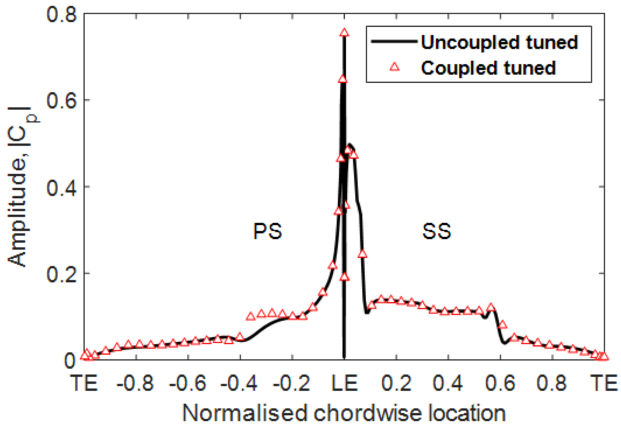

(a) Amplitude

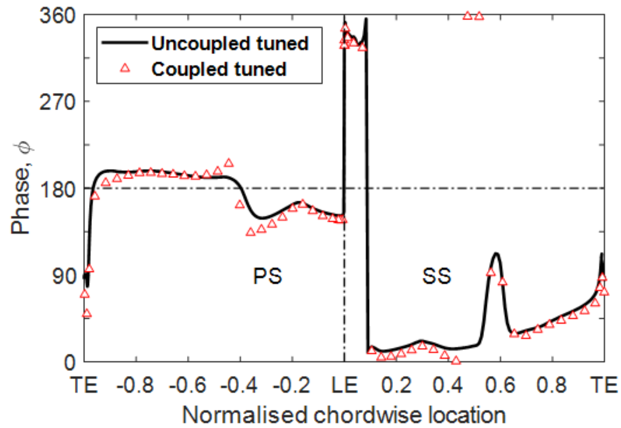

(b) Phase angle

Figure 5.7: Unsteady pressure responses at IBPA $\sigma = -120^0$.

5.3 Basic Vibration Characteristics of Mistuned Cascade

5.3.1 Random Structural Mistuning

In this study, structural mistuning is realised by changing the blade stiffness while retaining its mass and inertia, thus effectively changes the eigen-frequency of each individual blade. Hence, this type of structural mistuning is also known as frequency mistuning. The random mistuning pattern is illustrated in Figure 5.8, where the mistuned frequency is within the range of ±1% from the nominal tuned cascade.

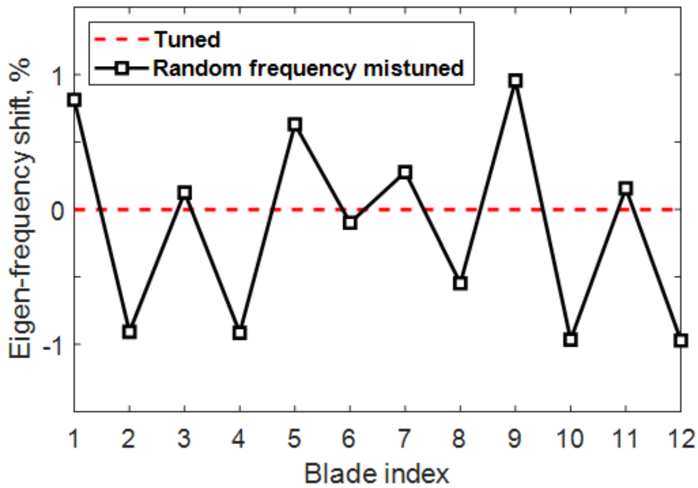

Figure 5.8: Random mistuning pattern.

Figure 5.9 compares the eigen-frequency and oscillating frequency of the randomly mistuned cascade. The oscillating frequency is obtained for each individual mistuned blade by performing Fast Fourier transform (FFT) on its vibration history. It is interesting to note that all mistuned blades eventually couple and oscillate at the same frequency although each blade has a rather different eigen-frequency to start with.

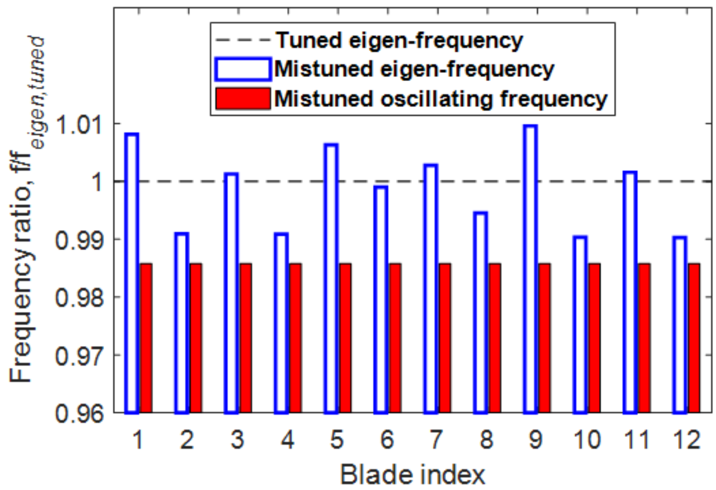

Figure 5.9: Random structural mistuning frequency distribution for all blades.

Figure 5.10 presents the phase evolution of each blade with time. It can be seen that the vibrations of all blades follow a horizontal line (denoted as a white dashed line in Figure 5.10), which mean that all blades are largely in phase with each other. This represents a standing wave with a constant IBPA $\sigma = 0^0$.

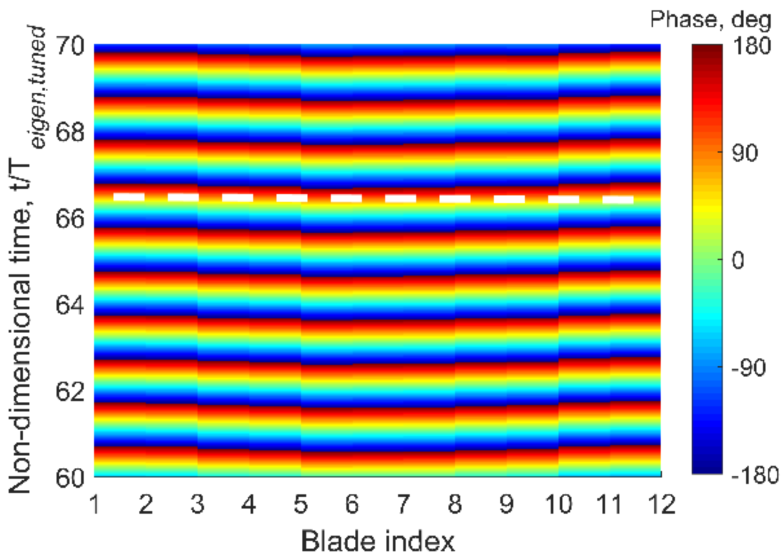

Figure 5.10: Random structural mistuning phase distribution for all blades.

Figure 5.11 presents the normalised blade vibration amplitude against the cascade-averaged value during a specific oscillation cycle. If the tuned cascade theory still holds [Lane, 1956], one would expect to observe a constant vibration amplitude across the cascade. Instead, vibration amplitudes can be seen to vary among blades for the structurally mistuned configuration. The variation pattern can be related to the imposed structural mistuning pattern (see Figure 5.8), in which high eigen-frequency blades tends to have high vibration amplitudes. The magnitude of variation is also large with up to ±40% difference compared to the mean value of the whole bladerow.

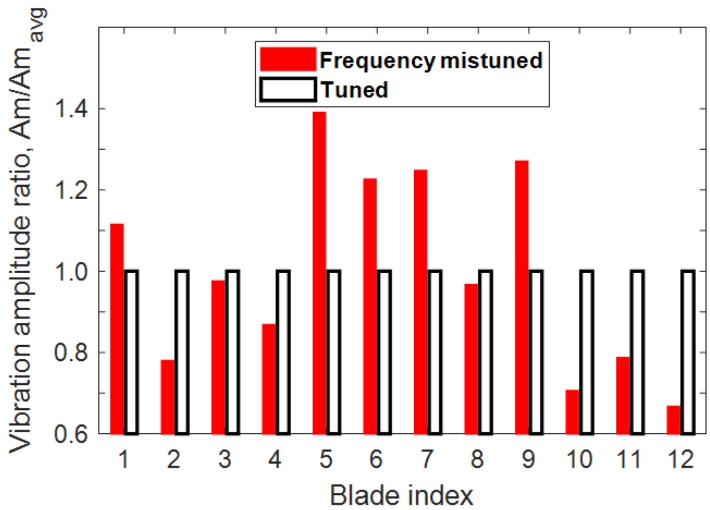

Figure 5.11: Random structural mistuning amplitude distribution for all blades.

5.3.2 Random Aerodynamic Mistuning

In the present work, aerodynamic mistuning is realised by changing the blade stagger angle. A twelve-blade randomly mistuned cascade is reused with the same mistuning pattern as in the previous case. However, this time each blade has the same eigen-frequency but different (mean) stagger angle. The random mis-stagger angle is within the range of $\pm 1^0$ from the nominal conditions.

Figure 5.12 presents the imposed steady mis-staggered pattern and the mean vibration position. The mis-staggering pattern is randomly distributed within the range of $\pm 0.5^0$ from the tuned nominal position. The mean vibration positions can be seen to be consistent with the steady mis-staggered pattern. This suggests that the unsteady interactions of the aero-mistuned blades in this particular test case and condition have small influence on the time-averaged (steady) responses.

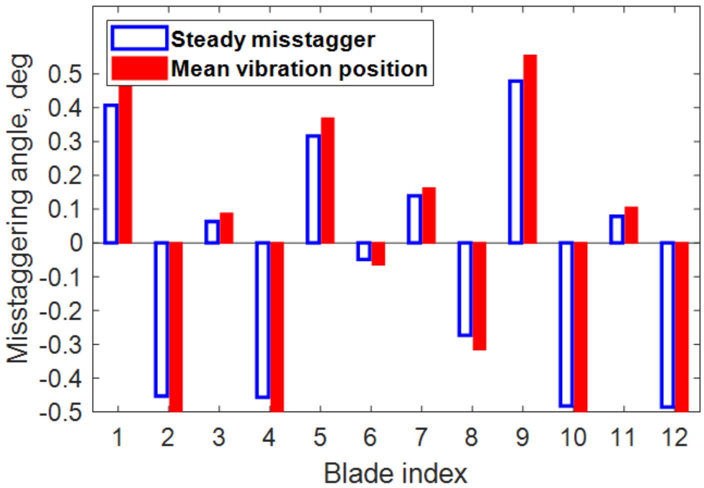

Figure 5.12: Steady/mean mis-staggering for all blades in the random aerodynamic mistuning.

All blades in the aerodynamically mistuned cascade have the same structural properties, thus the same eigen-frequency. Therefore, it is not surprising that all blades oscillate at the same coupled frequency. We then turn our attention to the phase angle distribution of the aerodynamically mistuned cascade as shown in Figure 5.13. Similarly to the tuned cascade, the inter-blade phase angle remains constant across the cascade. In this case, a standing-wave ($\sigma = 0^0$) is observed as denoted by the white dashed line.

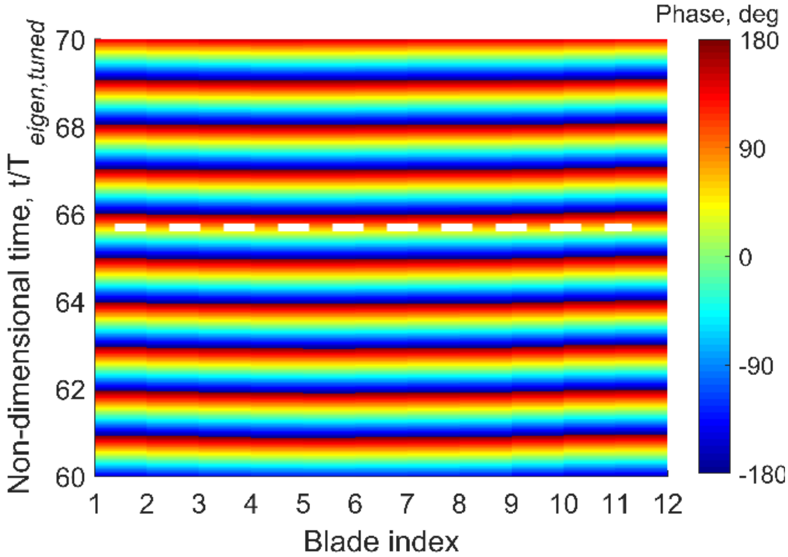

Figure 5.13: Random aerodynamic mistuning phase distribution for all blades.

Figure 5.14 presents the normalized vibration amplitude of the aero-mistuned cascade in comparison with the expectation from the tuned cascade. Vibration amplitudes can be seen to vary among blades, although the variation (±15%) is much less than that of the structurally mistuned configuration (±40%).

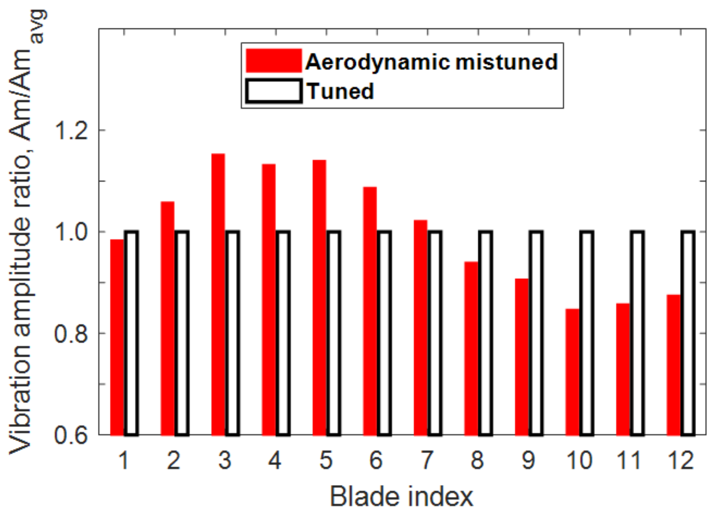

Figure 5.14: Random aerodynamic mistuning amplitude distribution for all blades.

5.3.3 Random Concurrent Structural-Aerodynamic Mistuning

In reality, both structural and aerodynamic mistuning will be inevitably co-existing in a bladerow. A standalone structural or aerodynamic mistuning is still a simplified representation of the mistuned system, although it has been useful to investigate its effect in a separate manner. In this section, we attempt to study the concurrent structural-aerodynamic mistuned bladerow. The mistuned eigen-frequency distribution is the same as in the standalone structural mistuning case, while the mis-staggered angle distribution is the same as in the standalone aerodynamic mistuning case. From Figure 5.15, the mean vibration positions of the concurrent structural-aero mistuning resemble that of the aero mistuning only configuration. This suggests aero-mistuning is solely responsible for the mis-staggering characteristics.

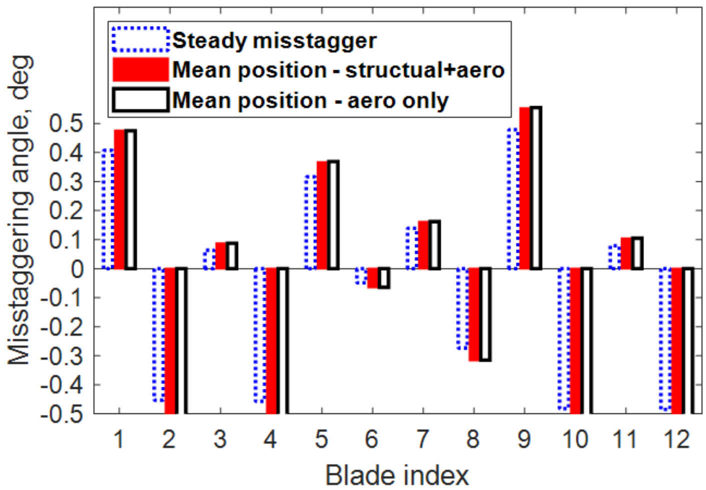

Figure 5.15: Steady/mean mis-staggering for all blades in the concurrent structural-aerodynamic mistuning.

Figure 5.16 shows the frequency distribution of the concurrent structural-aero mistuned cascade. Similarly to the case with structural mistuning only, the coupled oscillating frequency is constant across the cascade regardless of the initial randomly distributed eigen-frequency.

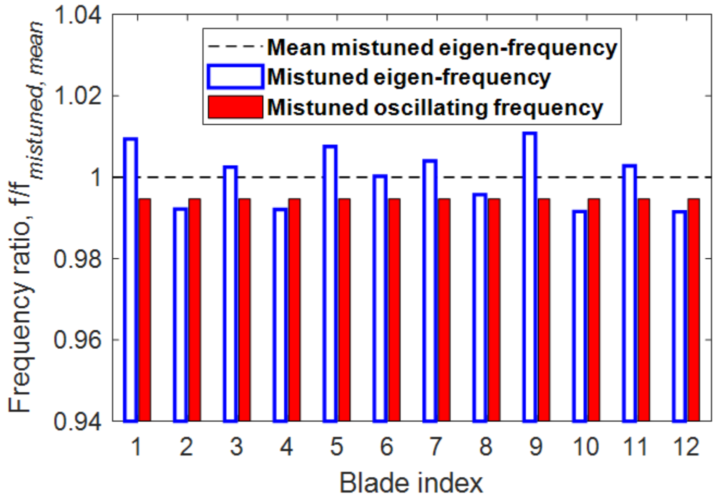

Figure 5.16: Concurrent structural-aerodynamic mistuning frequency distribution for all blades.

Figure 5.17 tracks the instantaneous phase temporal evolution of each blade across the concurrent structural-aero mistuned cascade. Vibrations of all blades follow a horizontal line (denoted as a white dashed line in Figure 5.17), which mean that all blades are largely in phase with each other. This represents a standing wave with a constant IBPA $\sigma = 0^0$.

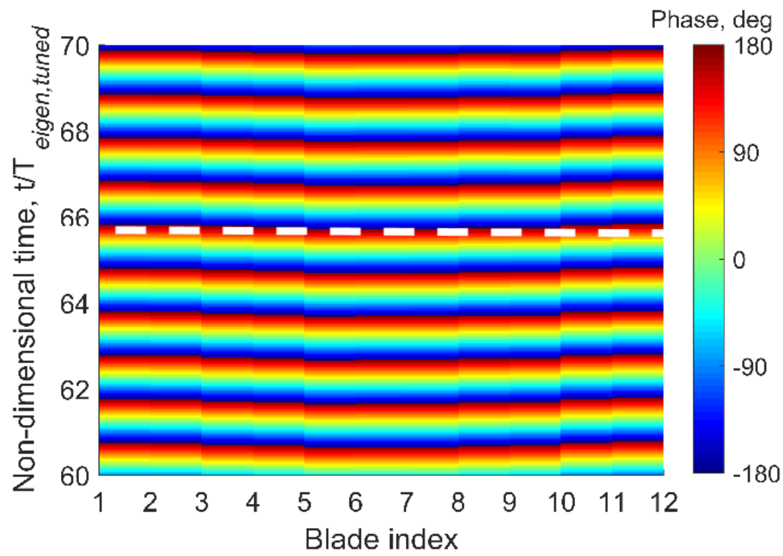

Figure 5.17: Concurrent structural-aerodynamic mistuning phase distribution for all blades.

Figure 5.18 presents the normalized vibration amplitude of the concurrent structural-aero mistuned cascade in comparison with the standalone structural mistuning. Vibration amplitudes can be seen to vary among blades with the variation magnitude up to ±60%. This variation magnitude is higher than both standalone structural or aerodynamic mistuning, which suggests that structural mistuning interacts with aerodynamic mistuning to amplify the mode localization effect.

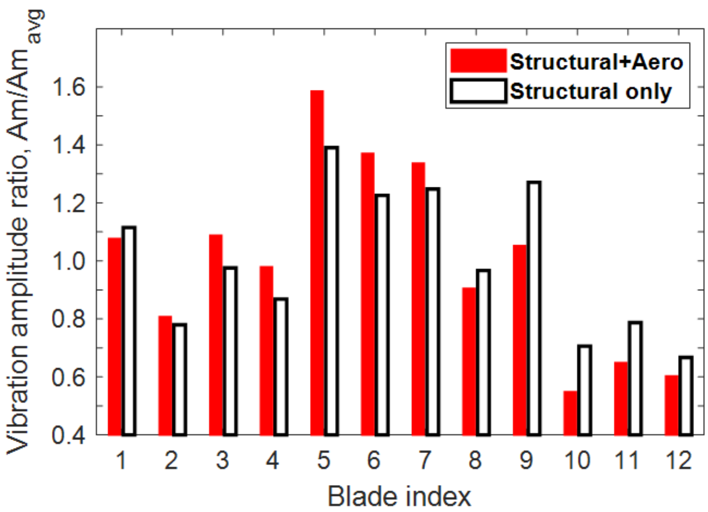

Figure 5.18: Concurrent structural-aerodynamic mistuning amplitude distribution for all blades.

5.4 Aeroelastic Impacts of Mistuning

5.4.1 Alternating Mistuning

Standalone Structural Mistuning

In this section, we will confine our investigations on the aeroelastic stability of an alternating mistuned cascade. The alternating mistuned pattern is illustrated in Figure 5.19, where the odd-numbered blades have higher eigen-frequency and even-numbered blades have lower eigen-frequency. The mean eigen-frequency of the mistuned cascade is the same of that in the tuned cascade. Four mistuning amplitudes will be studied, namely 1%, 2%, 3%, and 4%. Small values of mistuning strength is inevitably present in real configurations, while larger mistuning can be regarded as an intentionally mistuned design.

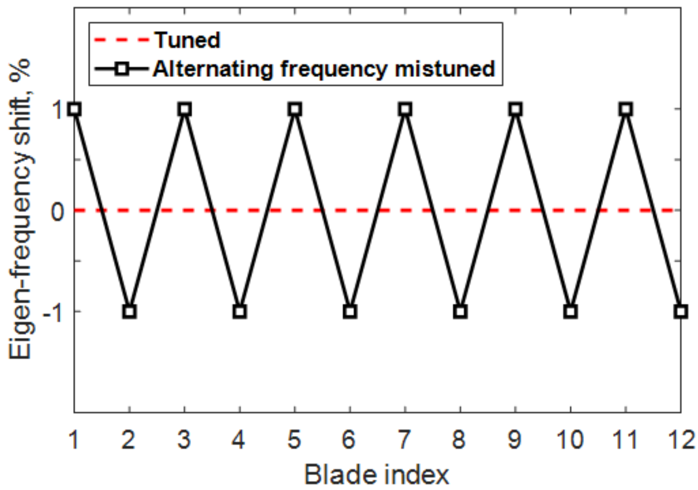

Figure 5.19: Alternating mistuning pattern of 1%.

Figure 5.20 compares the normalised log-dec of an alternating structurally mistuned cascade with a range of mistuning strength and mass ratio. Structural mistuning is observed to be stabilizing for all investigated cases. The stabilization effect increases monotonically as the mistuning strength increases. In addition, the mistuned cascade with higher mass ratio shows stronger stabilization effect.

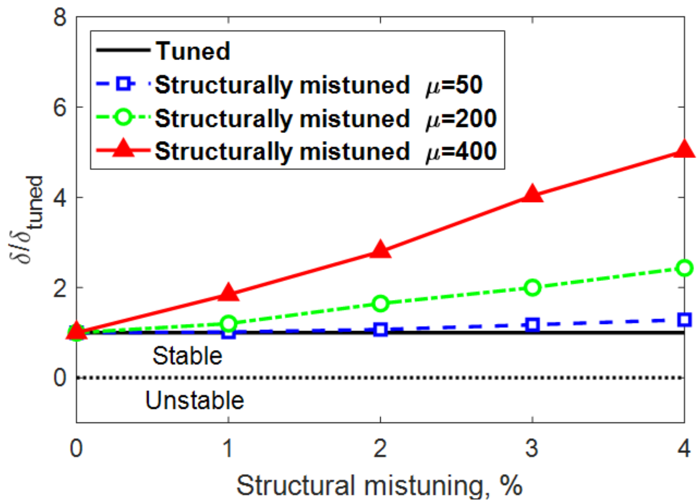

Figure 5.20: Alternating structural mistuning log-dec at $k = 0.8$.

It was observed in the first part of the present work that the vibration amplitudes in a structurally mistuned cascade would be scattered. This is also known as the localized vibration phenomena. Figure 5.21 presents the modal amplitude ratio for a range of mistuning strength and blade mass ratio. The modal amplitude ratio is the proportion of vibration amplitudes of the odd-numbered blade to that of the even-numbered blades in the alternating mistuned cascade. It can be seen that the modal amplitude ratio increases with the mistuning strength. The amount and rate of modal amplitude ratio increase is more obvious as the mass ratio rises. The trend of modal amplitude ratio (Figure 5.21) is similar to that of log-dec (Figure 5.20), thus suggesting that the gain in log-dec is associated with the stronger localization effect.

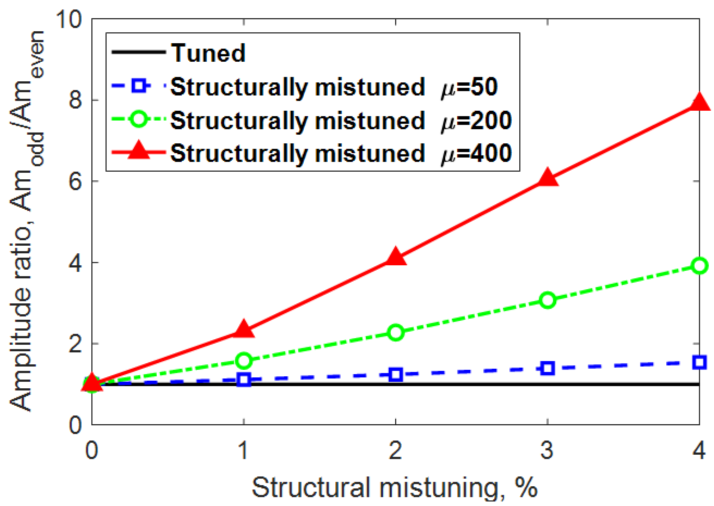

Figure 5.21: Alternating structural mistuning amplitude ratio at $k = 0.8$.

Figure 5.22 illustrates the vibration histories of the 1% frequency mistuning (Figure 5.22a) and 4% frequency mistuning (Figure 5.22b) configurations for a few oscillation cycles once the cascade has been coupled. The mode localization effect can visualized clearly from Figure 5.20, where the odd blades have higher vibration amplitudes compared to the even blades. Both odd and even blades seem to vibrate in-phase with each other, in agreement with the previous observation that the inter-blade phase angle still remains largely constant for the frequency mistuned cascade.

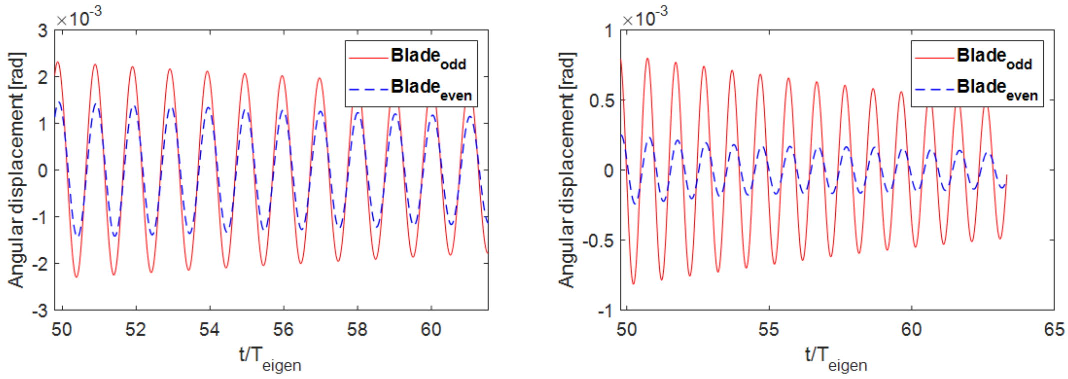

(a) 1% frequency mistuning **(b)** 4% frequency mistuning

Figure 5.22: Alternating frequency mistuning modal displacement at $\nu = 200$.

The above results show that there is a strong correlation between the mode localization and the stabilization effect for the free response of a frequency mistuned cascade. To aid understanding of the mode localization effect, we shall investigate blade responses for the tuned and the mistuned cascade as shown in Figure 5.23. The odd-numbered and even-numbered blades have identical responses for the tuned cascade as the vibration is at IBPA $= 0^0$. On the other hand, odd-numbered and even-numbered responses differently with a non-zero phase angle for the mistuned cascade. As a result, new inter-blade phase angle responses, which are more stable than the minimum IBPA, have been introduced to the mistuned cascade [Bendiksen, 2000]. Thus, the mistuned cascade is stabilized via the mode localization effect. In addition, mode localization increases monotonically with mistuning amplitude. Interestingly, it is also observed that mode localization increases when blade mass ratio increases. Because no structural coupling is present in our computational model, the blade-to-blade coupling takes place via surrounding aerodynamics. As blade mass ratio increases, the blade is more rigid, thus weaker aerodynamics inter-blade coupling. The vibration energy cannot be communicated easily across the cascade, giving rise to the mode localization effect.

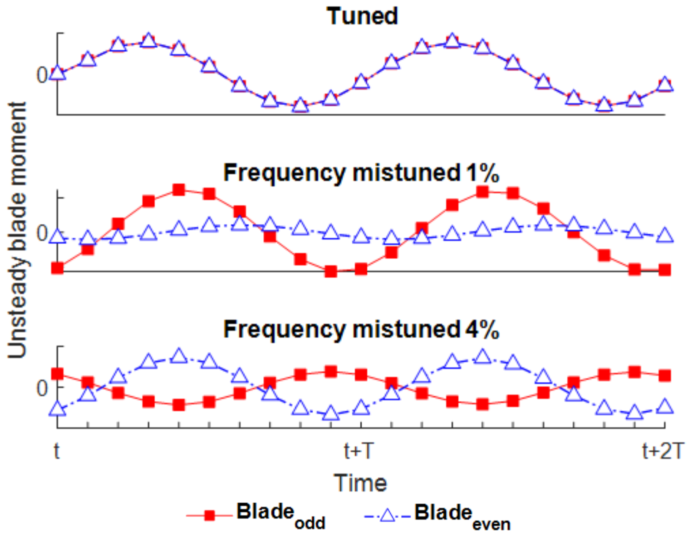

Figure 5.23: Alternating frequency mistuning unsteady blade moment at $\mu = 200$.

Standalone Aerodynamic Mistuning

Next, the alternating aerodynamic mistuned cascade is investigated. The odd-numbered blades are positively mis-staggered, while the even-numbered blades are negatively mis-staggered. The mean stagger angle of the mistuned cascade is the same of that in the tuned cascade. Three mis-staggered angles will be studied, namely 0.5, 1.0, and 1.5 degrees. Figure 5.24 compares the normalized log-dec of an alternating aerodynamic mistuned cascade with a range of mistuning strength and mass ratio. Interestingly, log-dec first increases for small values of mis-staggered angle then decreases as the mis-staggered amplitudes become bigger. This tendency is affected marginally by the blade mass ratio.

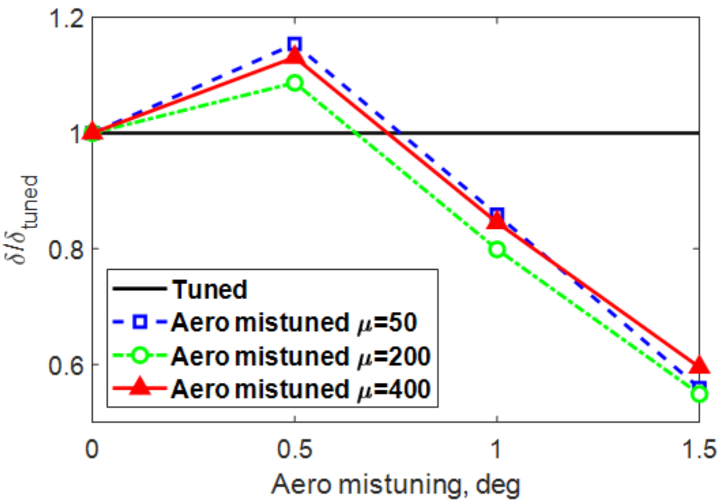

Figure 5.24: Alternating aerodynamic mistuning log-dec at $k = 0.8$.

Figure 5.25 illustrates the vibration histories around the mean stagger angle of the 0.5deg mis-staggering (Figure 5.25a) and 1.0 deg mis-staggering (Figure 5.25b) for a few oscillation cycles once the cascade has been coupled. Unlike the case of the structurally mistuned cascade, the mode localization effect is not strong in the aerodynamically mistuned cascade. Both odd and even blades vibrate in-phase with each other, in agreement with the previous observation that the inter-blade phase angle remains constant for the aerodynamically mistuned cascade.

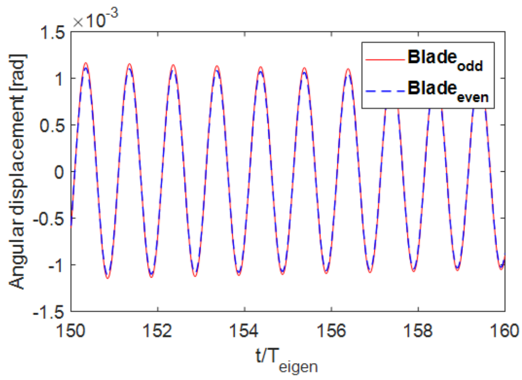

(a) 0.5^0 mis-staggering

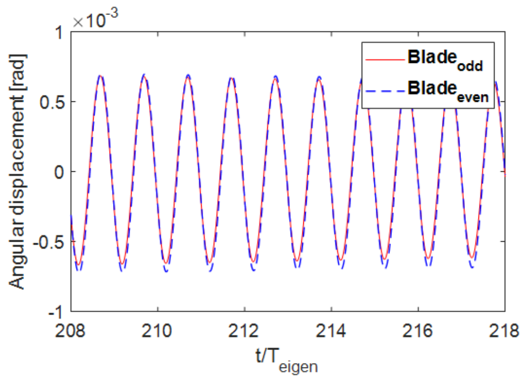

(b) 1.0^0 mis-staggering

Figure 5.25: Alternating aerodynamic mistuning modal displacement around mean position at $\mu = 400$.

If the mode localization effect is not a dominant factor in determining the aeroelastic stability of the aerodynamically mistuned cascade, we shall attempt to explain its stability mechanism from the unsteady aerodynamics point of view. It is already seen that the aerodynamically mistuned cascade greatly resembles the tuned cascade with a unique oscillating frequency, constant inter-blade phase angle, and largely constant modal amplitude. Thus, one can use a tuned-like behaviour to study its vibration effects. We will adopt the influence coefficient method (ICM) terminology here, where the aerodynamic damping of an alternating aerodynamic cascade can be decomposed to individual contribution of the reference blade itself and its neighbours. Only two immediate neighbours are considered since the effects of further blade would diminish.

Figure 5.26 presents the aero-damping decomposition for the negatively mis-staggered (Figure 5.26a) and the positively mis-staggered (Figure 5.26b) blades from the ICM cascade. As expected from the influence coefficient decomposition, the contribution of the reference blade itself is dominant. As the mis-staggering amplitude increases, the negatively mis-staggered blade shows a reduction in positive aero-damping of the reference blade, while the adjacent blades' contribution remain the same. In contrast, the positively mis-staggered blade maintains a similar contribution of the reference blade, whereas the contribution of blade B+1 (blade next to the reference blade's suction surface) is reduced. To find the overall damping, one has to sum all the contributions from the reference blade itself and from its neighbours. It can be seen that the overall damping of the negatively mis-staggered blade would be reduced, while that of the positively mis-staggered blade would increase. The aeroelastic stability of the system is determined by the minimum stability of each constituent blade. Therefore, the system's stability is closely related to the stability of the negative mis-staggered blade.

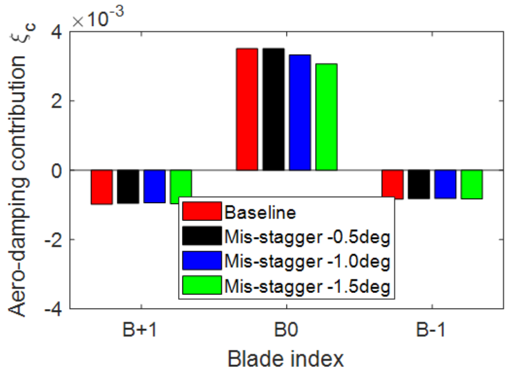

(a) Negative mis-staggering

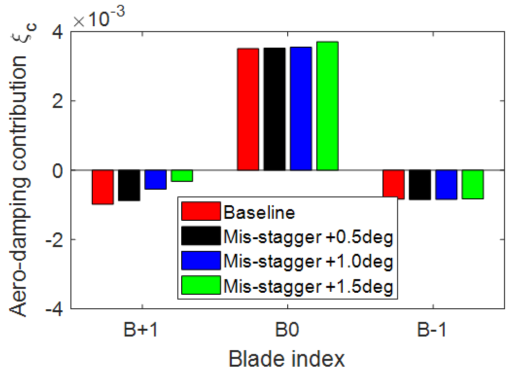

(b) Positive mis-staggering

Figure 5.26: Aerodynamic damping decomposition for mis-staggered blades.

Figure 5.27 shows the summed damping contribution of the negatively mis-staggered blade as discussed above in comparison with the baseline cascade. Figure 5.27 exhibits the same trend of the aerodynamic mistuning effects to Figure 5.24. Thus, it can be concluded that the unsteady aerodynamics of ICM tuned cascade can be used to explain the aeroelastic behaviour of the aerodynamically mistuned cascade even at a large mistuning strength. In addition, the negatively mis-staggered blade is subject to higher flow incidence, thus it is more prone to flow separation especially during upstroke oscillation cycle. These characteristics would make the negatively mis-staggered less stable as already found from the previous discussion. Thus, the negatively mis-staggered could be more likely to experience high-incidence flutter.

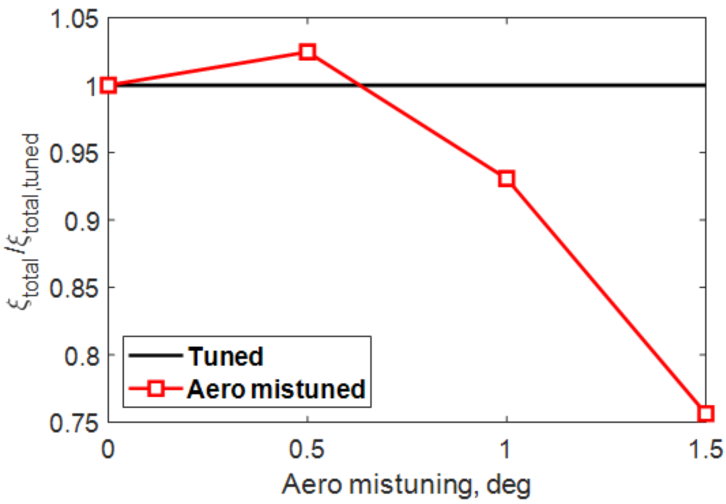

Figure 5.27: Alternating aerodynamic mistuning summed aero-damping.

Although the aero-mistuned cascade is more destabilizing at high values of mis-staggering compared to the tuned cascade (see Figure 5.24), the aero-mistuned cascade is still stable without any sign of flutter at the high reduced frequency condition $k = 0.8$. It would be of interest to explore and answer a question: *if a blade row is structurally tuned, can there be an operating condition at which the aero-mistuned cascade is unstable but the aero-tuned cascade is stable?*

To answer the research question above, we lower the reduced frequency to $k = 0.3$ to promote the flutter susceptibility. Interestingly, a contrasting behaviour between the fully tuned cascade and the alternating aero-mistuned but structurally tuned cascade can be observed as shown in Figure 5.28. Although the fully tuned cascade's vibration is decaying (thus stable, as shown in Figure 5.28a), the vibratory displacement of the alternating aero-mistuned but structurally-tuned cascade amplifies with time, i.e. unstable (Figure 5.28b).

Concurrent Structural-Aerodynamic Mistuning

Given that the standalone structural mistuning has a stabilising effect as observed in the previous section, another different but related research question arises: *what is the interaction between an aerodynamic mistuning and a structural mistuning, when they co-present in the cascade?* Particularly for the already unstable alternating aero-mistuned configuration, the impacts of additional structural mistuning would be of interest.

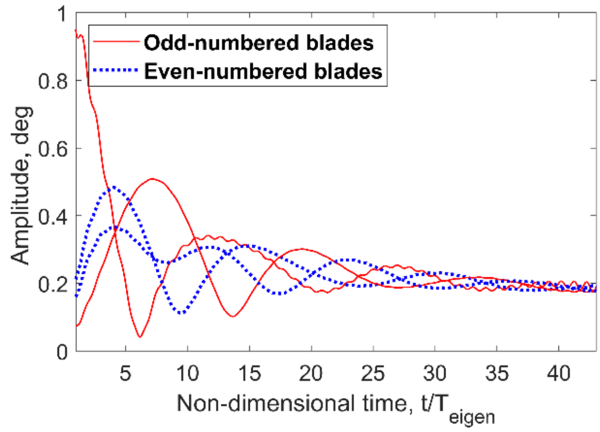

(a) Aerodynamically tuned + Structurally tuned

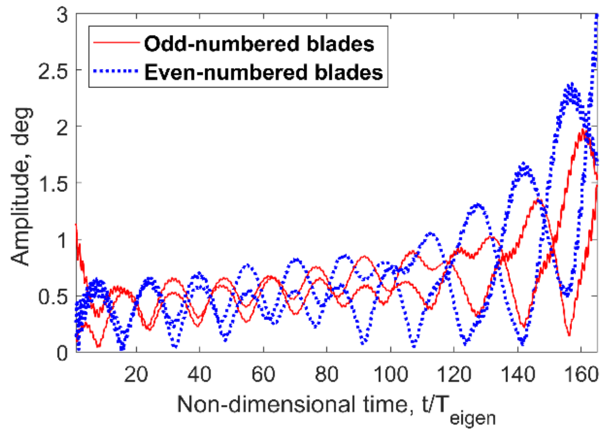

(b) Alternating aero-mistuning 1.5deg + Structurally tuned cascade

Figure 5.28: Amplitude evolution of the tuned and alternating aero-mistuned cascade.

Figure 5.29 presents the amplitude evolution for the aero-mistuned cascade subject to additional 1% structural mistuning (Figure 5.29a) and 4% structural mistuning (Figure 5.29b). It can be seen that both configurations still experience flutter with amplifying vibration amplitudes. It is reminded that 4% structural mistuning by itself could increase five-fold the aeroelastic stability at $k = 0.8$ (see Figure 5.20) compared to the tuned cascade. However, the additional alternating structural mistuning in the present unstable aero-mistuned cascade is shown to behave differently. Quite remarkably, the additional structural mistuning seems to result in an opposite adverse effect now. The seemingly destabilizing effect of the structural mistuning manifests in terms of a strong localization which exacerbates the instability of the most unstable blade. As the structural mistuning increases from 1% to 4%, the most unstable blade reaching a larger amplitude after a fewer number of oscillation cycles.

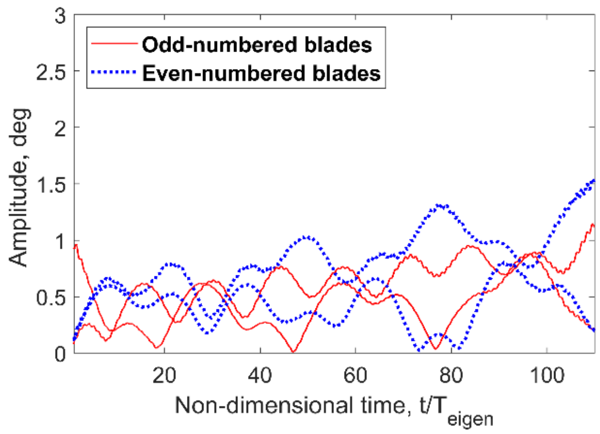

(a) Alternating aero-mistuning 1.5deg + Alternating structural mistuning 1%

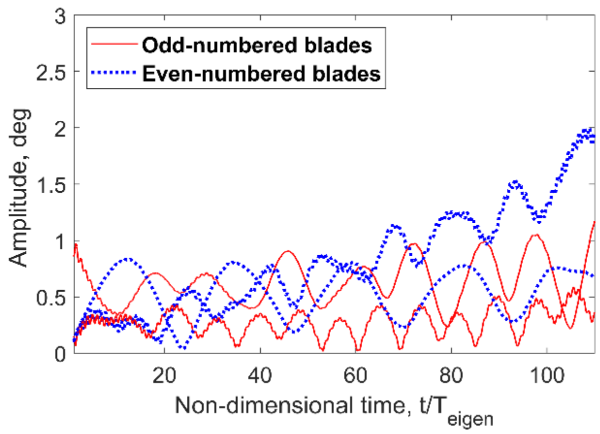

(b) Alternating aero-mistuning 1.5deg + Alternating structurally mistuning 4% cascade

Figure 5.29: Amplitude evolution of the alternating concurrent mistuned cascade with different structural mistuning levels.

5.4.2 Random Mistuning

The previous work has been carried out with an alternating mistuning configuration. It is imperative to check whether the mistuning pattern would affect our findings. In this section, we use an eight-passage configuration subject to random mistuning pattern.

Standalone Aerodynamic Mistuning

Figure 5.30a shows that the eight-passage tuned cascade is stable with decaying amplitude, in agreement with the previous finding. This suggests that the final vibration mode of the tuned cascade is not sensitive to the computational domain size. On the other hand, Figure 5.30b shows that the randomly aero-mistuned configuration does not experience flutter unlike in the alternating mistuning case. Nevertheless, the fluctuating amplitudes in Figure 5.30b point out that the vibration has a beating characteristics that stands out from the tuned configuration.

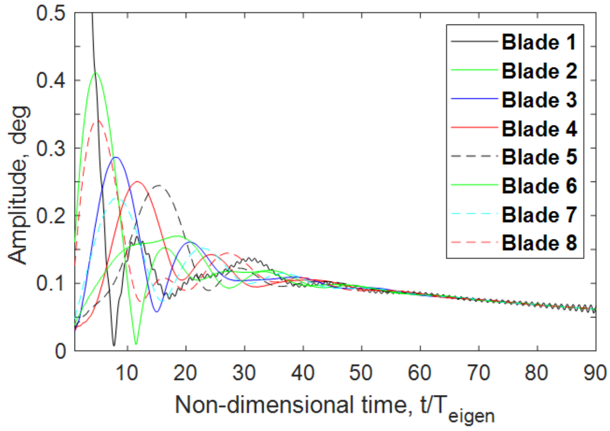

(a) Aerodynamically tuned + Structurally tuned

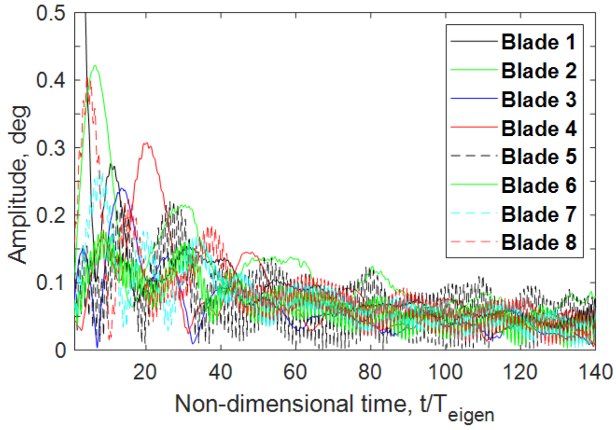

(b) Random aero-mistuning 1.5deg + Structurally tuned cascade

Figure 5.30: Amplitude evolution of the tuned and random aero-mistuned cascade.

Concurrent Structural-Aerodynamic Mistuning

A random structural mistuning is further added to the randomly aero-mistuned cascade. Figure 5.31 shows the amplitude evolution of the aero-mistuned cascade with additional 1% structural mistuning (Figure 5.31a) and 4% structural mistuning (Figure 5.31b). Again, it is clear that the additional structural mistuning has the possibility to exacerbate the cascade instability. With 4% structural mistuning, the most vulnerable blade in the cascade reaches a larger vibration amplitude. As a result, it can be concluded that adding the structural mistuning to the pure aero-mistuned cascade does not always alleviate the instability. On the contrary the added structural mistuning can amplify the vibration amplitude of the most vulnerable blade, most likely due to the associated strong modal localization.

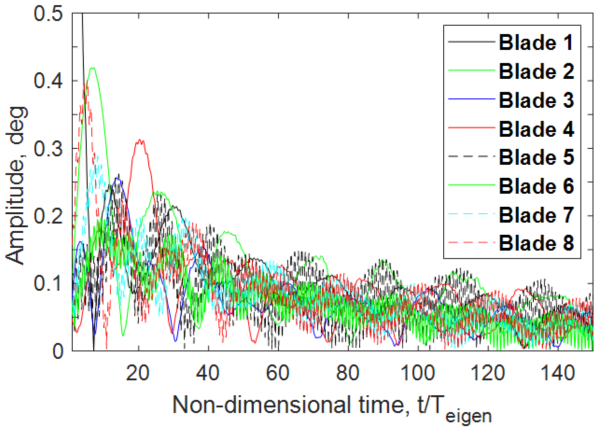

(a) Random aero-mistuning 1.5deg + Random structural mistuning 1%

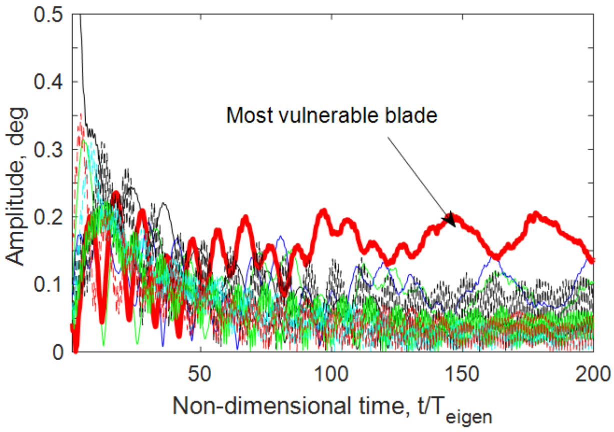

(b) Random aero-mistuning 1.5deg + Random structurally mistuning 4% cascade

Figure 5.31: Amplitude evolution of the random concurrent mistuned cascade with different structural mistuning levels.

5.5 Summary

The objectives of the present paper are to enhance the understanding of the fundamental vibration characteristics and the aeroelastic impacts of the structurally and aerodynamically mistuned cascade. The high-fidelity nonlinear time-domain fully-couple method has been used, without any frequency-domain related CFD reduced-order modeling assumptions. Regarding the basic vibration characteristics of the mistuned cascade, the main observations are:

1. Standalone structural mistuning: blades vibrate with the same coupled frequency, a predominantly constant inter-blade phase angle, but non-uniform amplitudes with a strong amplitude localization.

2. Standalone aerodynamic mistuning: blades vibrate with the same coupled frequency, a constant inter-blade phase angle, a weak amplitude localization, and varying mean blade positions.

3. Concurrent structural-aerodynamic mistuning: blades vibrate with the same coupled frequency, a predominantly constant inter-blade phase angle. The amplitude localization seems stronger than the standalone structural mistuning case. The mean positions are similar to the standalone aerodynamic mistuning case.

Regarding the aeroelastic impact of mistuning in the second part of the work, the following observations are made:

1. Standalone structural mistuning: it always has a stabilising effect. The degree of stabilisation strongly correlates to that of the aeroelastic coupling in terms of the blade mass coefficient.

2. Standalone aerodynamic mistuning: it has a stabilising effect with a small amount of mistuning but shows a destabilising effect with a large mistuning. An aero-mistuning induced flutter with an alternating configuration has been reported for the first time. It shows that an aerodynamic mistuning can lead to flutter at a condition where the tuned cascade is still stable.

3. Concurrent structural-aerodynamic mistuning: when both aerodynamic and structural mistuning are present, there seems to be a distinctive nonlinear interaction between the two. It has been shown that the stability of the unstable aero-mistuned cascade may be improved with a small additional structural mistuning, but degraded remarkably with a larger value of additional structural mistuning.

6

Phasing of Structural and Aerodynamic Mistuning for Leveraging Aeroelastic Performance

Contents

In this chapter, the interactions between the structural mistuning and the aerodynamic mistuning are further investigated with a focus on the design concept to leverage the blade's aeroelastic performance. The superposability of the two types of mistuning is examined to study the effectiveness of the simple linear superposition method.

6.1 Test Case Descriptions

The control-diffusion compressor blade geometry used in the previous validation chapter is used in this study of mistuning effects. The simulation domain is a two-dimensional cascade with 12 blade passages and periodic lateral boundaries. The baseline flow conditions of the tuned cascade are the same as that in the validation chapter.

To simulate the structural mistuning effects, the blade eigen-frequencies are modified via their blade stiffness. On the other hand, aerodynamic mistuning effects are simulated via the change in their stagger angles. The blades vibrate in the torsional mode. For forced response study, the hypothetical assumption is that the inlet distortion has a sinusoidal form with a certain frequency and a circumferential period.

In the next section, mistuned cascade will be investigated using the fully-coupled fluid-structure interaction method. The data is post-processed using the methods described in the chapter 3 and the appendix A.

6.2 Validations of Fully-Coupled against Uncoupled Forced Response

In the present work, we will perform a validation for the forced response vibration of the tuned cascade with the reduced frequency $k = 0.6$. The inlet total pressure distortion is used as the external forcing. Equation 6.1 shows the formula for the harmonic inlet total pressure distortion:

$$P_{01} = P_{01,uniform} + \Delta P_{01} \sin(\omega t + \theta_i) \tag{6.1}$$

where $P_{01,uniform}$ is the inlet total pressure at the nominal flow condition. ΔP_{01} is the amplitude of the distortion perturbation and is specified to be 10% of the nominal inlet total pressure. ω is the forcing frequency that sweeps across the range near the blade eigen-frequency. θ_i is the relative phase angle between the i$^{\text{th}}$ and the first pitchwise grid line.

Figure 6.1 presents the instantaneous total pressure contour across the fully-coupled cascade subject to the harmonic inlet distortion. Note that the total pressure is normalized against the nominal inlet total pressure $P_{01,uniform}$. Figure 6.1a shows the instantaneous contour of the quasi-steady inlet distortion with the circumferential period of 18-passage. On the other hand, Figure 6.1b presents the instantaneous contour of the unsteady inlet distortion with the reduced frequency $k = 0.6$ and the circumferential period of 4-passage. It can be seen that the quasi-steady inlet distortion passes through the cascade without turning, as opposite to that of the unsteady inlet distortion. In addition, the rotating direction and the spatial distribution of the total pressure distortion agrees with the pattern imposed at the inlet for both examples.

Extracting the forced response amplitude predicted by the fully-coupled simulation is straightforward. The fully-coupled forced response solution would produce a vibration history, where the steady-state amplitude can be obtained once the transient oscillation is over. On the other hand, the uncoupled forced response solution is less obvious. In the present work, we will use the single degree-of-freedom (1DOF) modal equation to solve for the uncoupled forced response amplitude. The method is similar to what were used in Ref. [Moffatt et al., 2005; Moffatt and He, 2005]. The damping and the forcing calculations are carried out separately to find the pure aerodynamic damping and the pure aerodynamic forcing, respectively. Then the uncoupled forced response amplitude is given by the following analytical equation:

$$\hat{q}_{uncoupled} = \frac{\hat{f}}{\sqrt{\left(\omega_n^2 - I\omega^2\right)^2 + \left(2\xi_{aero} I\omega_n\omega\right)^2}} \tag{6.2}$$

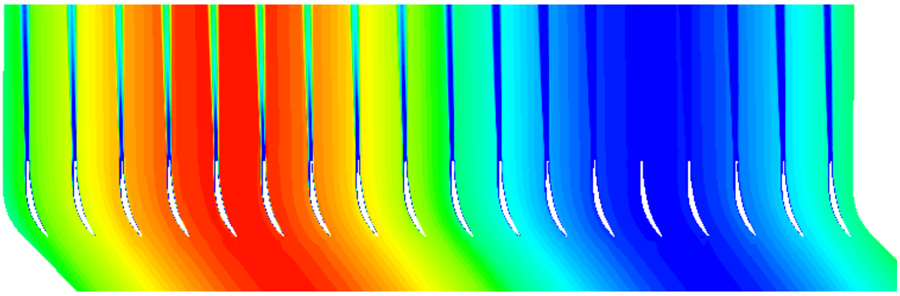

(a) Quasi-steady inlet distortion $k \approx 0$, 1 distortion revolution per 18-passage.

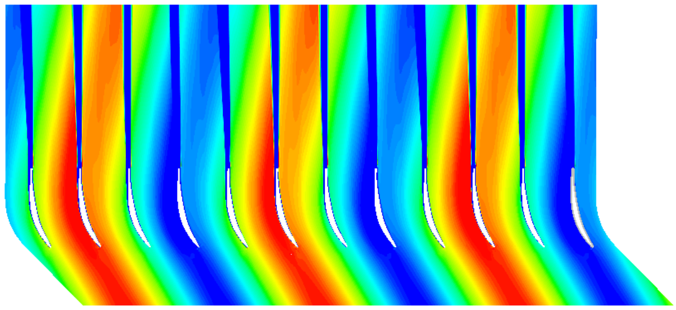

(b) Unsteady inlet distortion $k = 0.6$, 1 distortion revolution per 4-passage.

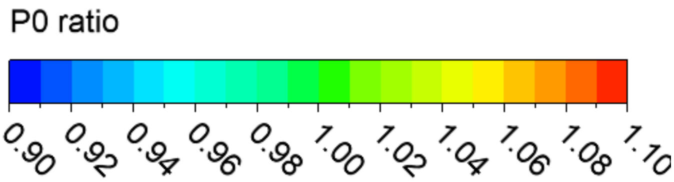

Figure 6.1: Examples of instantaneous normalized total pressure contours of the cascade subject to different harmonic inlet distortion configurations.

where $\hat{q}_{uncoupled}$ is the modal response amplitude. $\hat{f}$ is the modal excitation forcing. ω_n is the blade natural frequency. ω is the forcing frequency. I is the blade inertia. ξ_{aero} is the blade modal aerodynamic damping.

Figure 6.2 compares the forced response amplitude predicted by the uncoupled and the fully-coupled method. It can be seen that the predictions of two methods are well-matched for a range of forcing frequencies. The abscissa of Figure 6.2 is the normalized frequency, which is the ratio between the sweeping forcing frequency and the frequency at which the resonance occurs. Note that the conventional uncoupled method does not take into account the frequency shift, while it is a part of the solution in the fully-coupled method. To partially incorporate the fluid-structure coupling effects, one can use the modified uncoupled method in Ref. [Moffatt et al., 2005; Moffatt and He, 2005] for an improved prediction of the frequency shift by the uncoupled method.

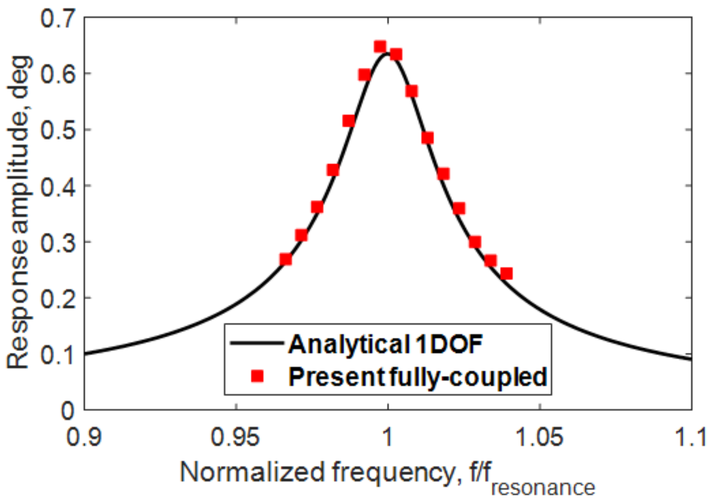

Figure 6.2: Comparison of response amplitudes between the analytical and the fully-coupled solutions for the tuned cascade.

Next, we will perform more detailed comparisons at the resonance peak. We shall adopt the energy method [Moffatt et al., 2005; Moffatt and He, 2005], which simplifies the forced response problem into an energy balance without the need to directly solve the equations of motion. The fundamental basis of the energy balance method is that the steady-state vibration occurs when the forcing (destabilizing) work balances the damping (stabilizing) work. A single point of equilibrium can be found when balancing the linear forcing work and the quadratic damping work. Figure 6.3 illustrates the energy balance concept between the forcing and the damping work.

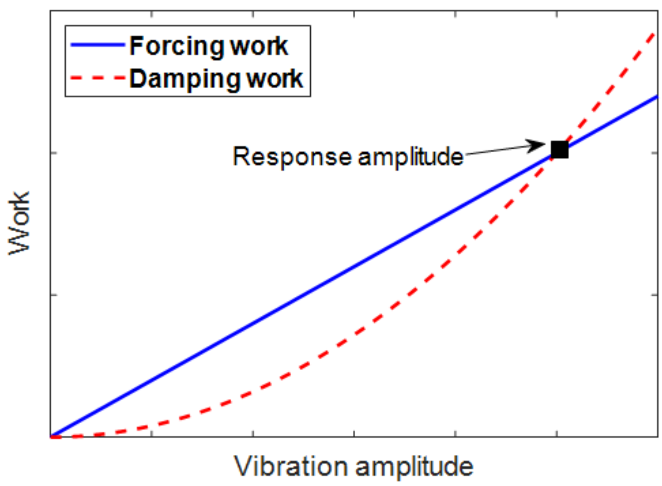

Figure 6.3: Balancing between forcing and damping work at resonance.

According to the analytical 1DOF solution, the phase different between the forcing and the response is 90deg at the resonance peak. However, for the present problem of the blade row subject to the inlet distortion, the phases are arbitrary since there is no fixed reference. To find the blade response phase at the resonance peak, we use an iterative approach to calculate the work done on the blade at different vibration phases [Moffatt et al., 2005; Moffatt and He, 2005]. The response phase is predicted to be at the configuration with the maximum destabilizing work. Figure 6.4 shows the vibration phase sweep to find the peak resonance response phase. Because both the blade motion and the external forcing are periodic, we observe a sinusoidal variation of the forcing work with the vibration phase. The blue square marker denotes the response phase at which the destabilizing work is maximum. The red triangle marker represents the response phase at which the fully-coupled solution is observed. It can be seen that the predicted peak resonance response phase are in very good agreement between the uncoupled and the fully-coupled method.

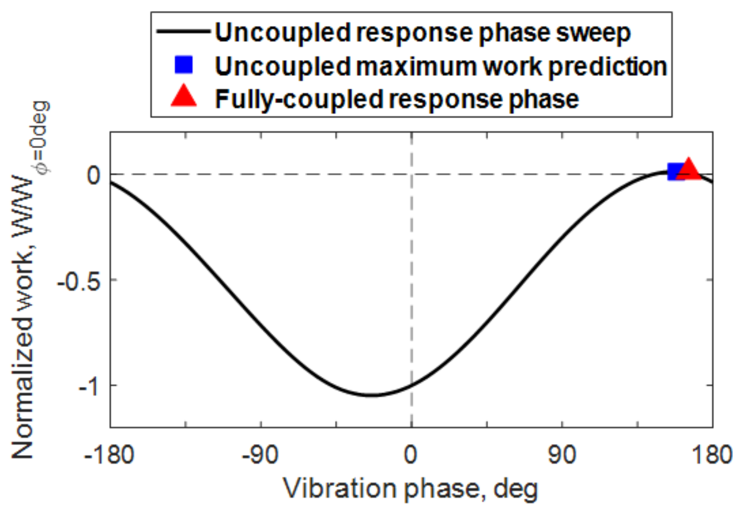

Figure 6.4: Comparison between uncoupled and fully-coupled response phase at resonance.

Figure 6.5 shows the local unsteady pressure responses at the peak resonance. Note that the responses are time-averaged from the instantaneous quantities obtained from the spatial-temporal Hilbert transform-based method. The results predicted by the uncoupled and the fully-coupled method are well-matched on the entire blade surfaces, even in the challenging region of the separation bubble formation (about 40% to 60% axial chord on the suction surface). There is a slight discrepancy in the predicted phase angle near the leading edge on the suction surface. However, this region has a small spatial confinement, leading to a negligible difference in the overall response. Therefore, it can be concluded that the fully-coupled method adopted in the current work is reliable for both the free response and forced response studies.

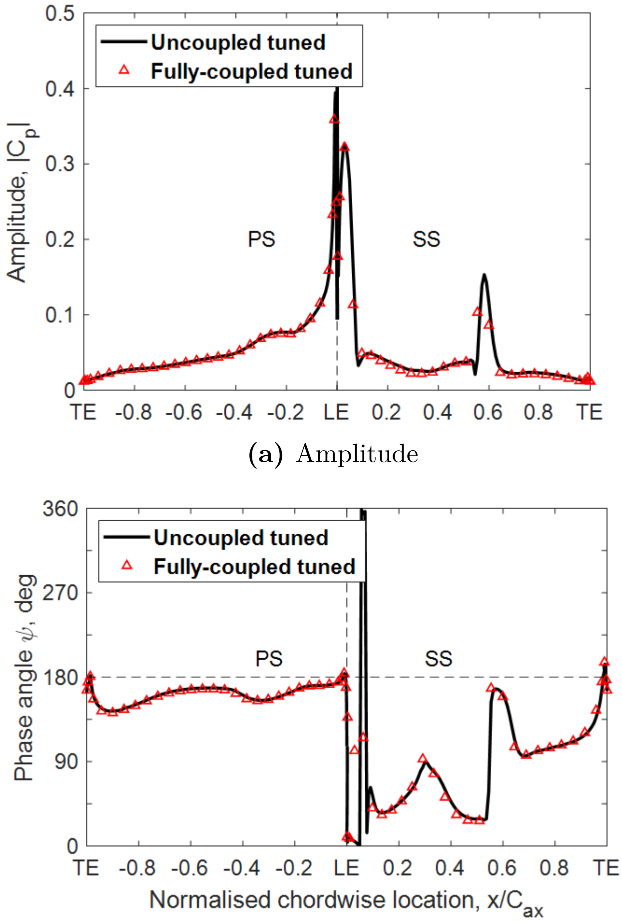

(a) Amplitude

(b) Phase angle

Figure 6.5: Unsteady pressures at the peak resonance response of the tuned cascade.

6.3 Impacts on Self-Excited (Flutter) Characteristics

We will firstly examine the self-excited vibration characteristics of the concurrent structural-aerodynamic mistuned cascade. Three types of mistuning pattern will be studied, namely alternating, sinusoidal, and random mistuning. For each type of mistuning pattern, the phasing effects between the structural and the aerodynamic circumferential mistuning pattern will be investigated.

6.3.1 Alternating Mistuning

The alternating mistuned configuration contains only two types of blade's characteristics. The first concurrent configuration is where the structural and the aerodynamic circumferential mistuning pattern are in phase with each other. In contrast, the other concurrent configuration consists of the out-of-phase circumferential mistuning pattern. Figure 6.6 illustrates these two configurations for the alternating mistuning case. The structural mistuning has a variation of the blade eigen-frequency within the range $\pm 1\%$, whereas the aerodynamic mistuning has a variation of the blade stagger angle within the range $\pm 0.5^0$.

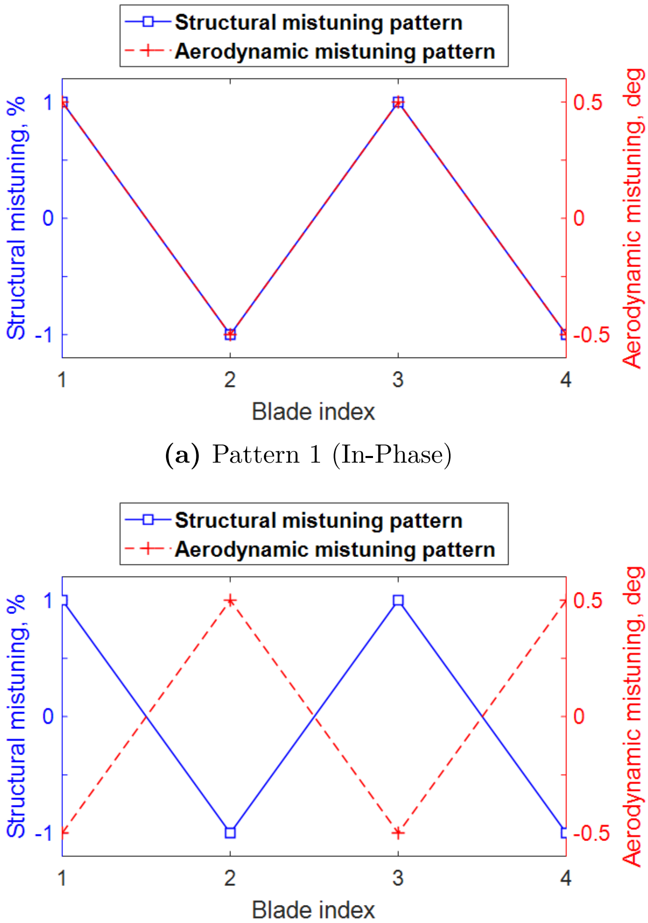

(a) Pattern 1 (In-Phase)

(b) Pattern 2 (Out-Phase)

Figure 6.6: Alternating concurrent mistuning patterns.

Figure 6.7 compares the aerodynamic damping of the concurrently mistuned configurations. It can be seen that the two patterns in Figure 6.6 induce different aeroelastic stability characteristics, although both configurations have higher values of the aerodynamic damping compared to the tuned cascade. The in-phase pattern is more favorable on the aeroelastic stability point of view with a higher aero-damping. The difference between two configurations is 16.2% compared to the tuned cascade level.

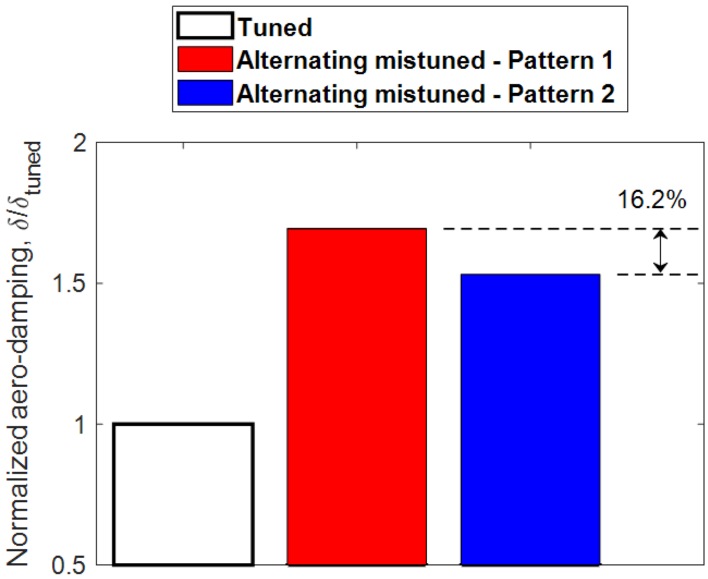

Figure 6.7: Alternating mistuned aerodynamic damping with different circumferential phasing.

6.3.2 Sinusoidal Mistuning

The sinusoidal mistuned configuration contains twelve different types of blade's characteristics. Figure 6.8 illustrates two possible ways the concurrently mistuned configuration can be set up. Figure 6.8a shows the situation where the structural mistuning pattern *leads* the aerodynamic mistuning pattern, and the circumferential phase difference between them is positive. On the other hand, Figure 6.8b illustrates an example where the structural mistuning *lags* the aerodynamic mistuning pattern, such that the circumferential phasing is negative. The structural mistuning has a sinusoidal variation of the blade eigen-frequency within the range $\pm 1\%$, whereas the aerodynamic mistuning has a sinusoidal variation of the blade stagger angle within the range $\pm 0.5^0$.

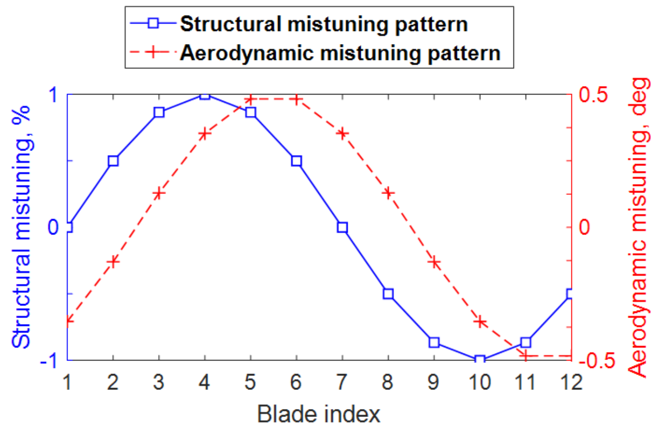

(a) Positive phase difference ($\theta = +45^0$)

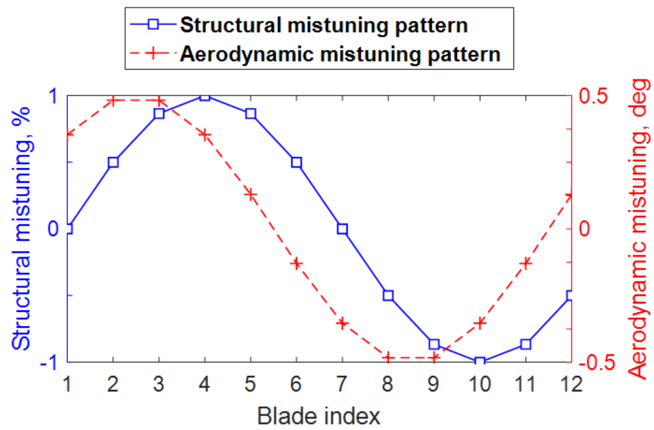

(b) Negative phase difference ($\theta = -45^0$)

Figure 6.8: Examples of sinusoidal concurrent mistuning.

Figure 6.9 compares the aerodynamic damping of the concurrently mistuned configurations with a sinusoidal variation. It is clear that the circumferential phasing of the concurrent mistuning pattern has a significant effect on the blade aeroelastic stability. Although all configurations of concurrent mistuning have higher values of the aerodynamic damping compared to the tuned cascade, there is a remarkable difference (up to 52.7% compared to the tuned level) between the best and the worst choice of the circumferential phasing. In addition, the negative circumferential phase difference configurations, where the structural mistuning lags the aerodynamic mistuning pattern, tend to have a better aeroelastic stability.

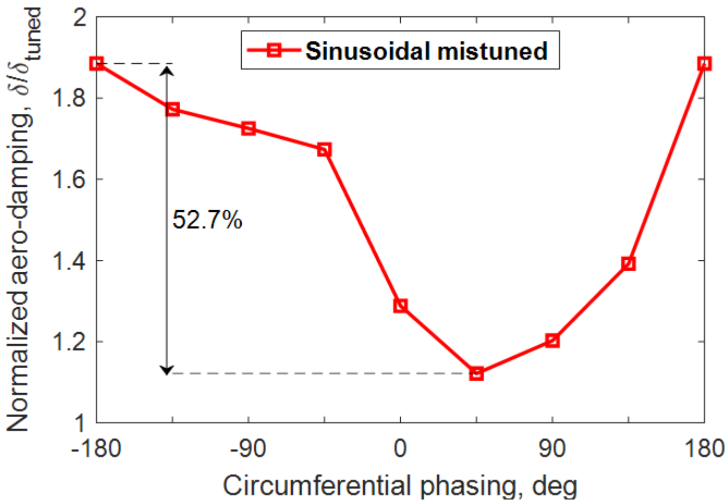

Figure 6.9: Sinusoidal mistuned normalised aerodynamic damping with different circumferential phasing.

6.3.3 Random Mistuning

The random mistuned configuration contains twelve unique values of blade's characteristics. Figure 6.10 illustrates two example setups of the concurrently mistuned configuration. It is obvious that there are N ways to perform the circumferential phasing for the blade row with N blades. The structural mistuning has a random variation of the blade eigen-frequency within the range $\pm 1\%$, whereas the aerodynamic mistuning has a random variation of the blade stagger angle within the range $\pm 0.5^0$.

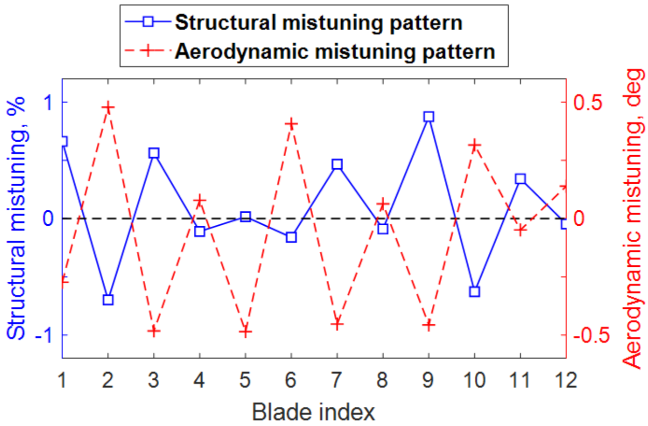

(a) Positive phase difference ($\theta = +150^0$)

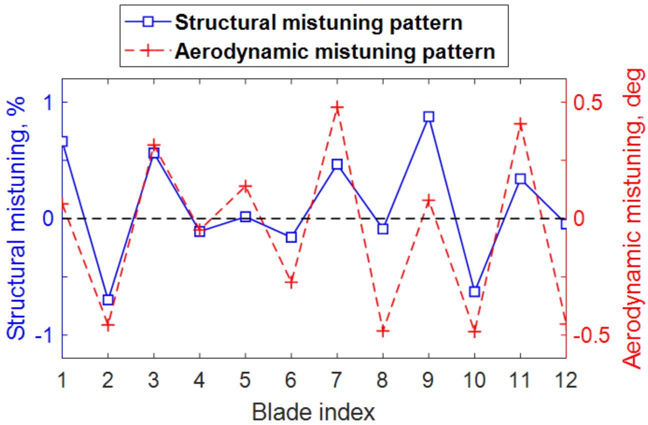

(b) Negative phase difference ($\theta = -60^0$)

Figure 6.10: Examples of random concurrent mistuning.

Figure 6.11 compares the aerodynamic damping of the concurrently mistuned configurations with a random variation. Although the circumferential phasing does have an effect on the aeroelastic stability, the difference between the best and the worst configuration is only 6.2% compared to the tuned cascade level.

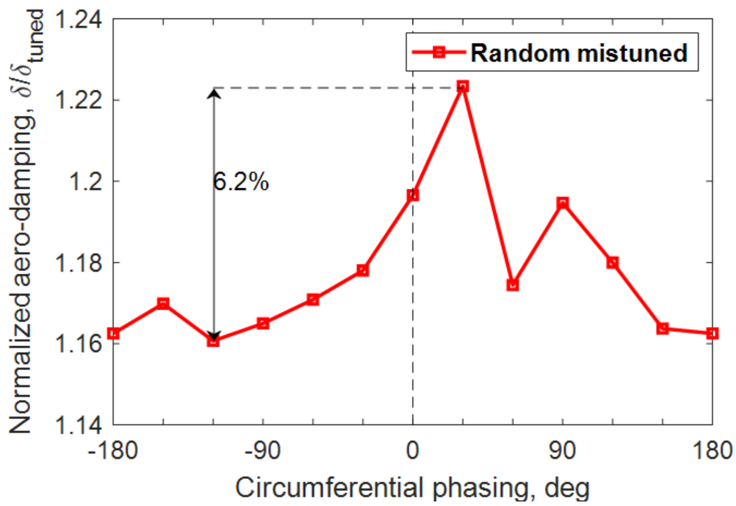

Figure 6.11: Random mistuned normalised aerodynamic damping with different circumferential phasing.

6.4 Impacts on Forced Response Characteristics

In this section, we will investigate the forced response vibration of the concurrent structural-aerodynamic mistuned cascade. Similarly to the previous section, the phasing effects between the structural and the aerodynamic circumferential mistuning pattern will be studied for three mistuning patterns.

6.4.1 Alternating Mistuning

Figure 6.12 compares the maximum response amplitude of the concurrently mistuned configurations of different circumferential phases. Both patterns of the alternating mistuned cascade have a forced response level much higher than that of the tuned cascade, which is known as the forced response amplification due to mistuning. Interestingly, there is a difference of 21.1% of the tuned response amplitude in the mistuned response of different patterns. The in-phase configuration (pattern 1) seems to be more favorable with a lower response amplification.

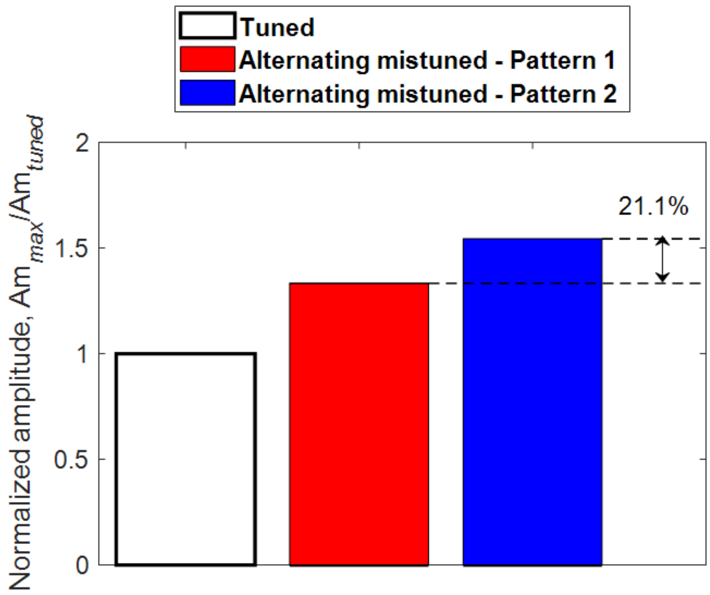

Figure 6.12: Alternating mistuned maximum forced response amplitude with different circumferential phasing.

Figure 6.13 shows the response amplitude of each blade in the concurrently mistuned cascade at the resonance peak. It can be observed that the even blades have the maximum response amplitude. If we consider the mistuning pattern illustrated in Figure 6.6, we can identify that the location of the maximum response amplitude coincides with the low eigen-frequency blades irrespective of the local mis-staggering values. Therefore, it can be concluded that the structural mistuning has a dominant effect on the forced response amplification. However, the aerodynamic mistuning also has considerable effects. In particular, the interaction between the structural mistuning and the aerodynamic mistuning can further impact the overall response, evidenced in the values of the maximum response amplitude observed by different circumferential mistuning phases.

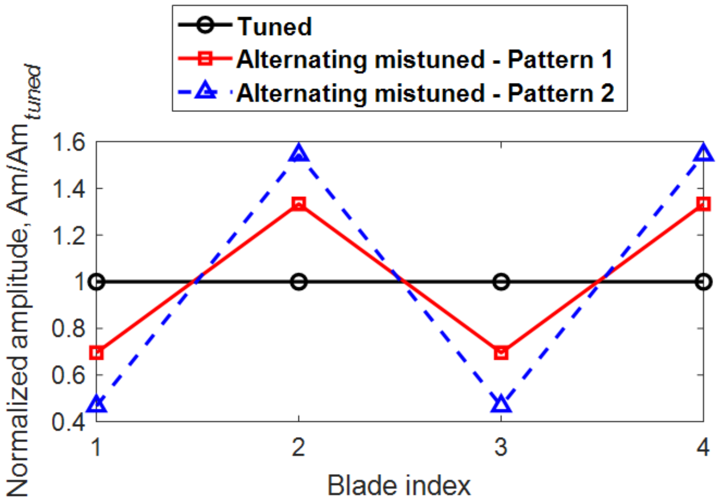

Figure 6.13: Alternating mistuned response amplitude distribution.

6.4.2 Sinusoidal Mistuning

Figure 6.14 compares the maximum response amplitude of the concurrently mistuned configurations of different circumferential phases with a sinusoidal variation. All mistuned configurations have a higher forced response level compared to that of the tuned cascade. The maximum response amplitude difference between the best and the worst configuration is 16% of the tuned response level. Interestingly, the configurations with negative circumferential phases seem to be more beneficial with lower response amplitudes.

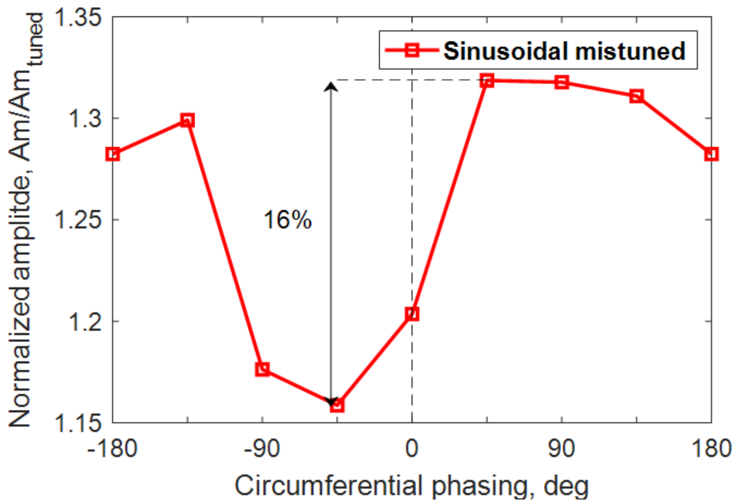

Figure 6.14: Sinusoidal mistuned maximum forced response amplitude with different circumferential phasing.

Figure 6.15 presents the response amplitude distribution of all blades at the resonance peak for the best (circumferential phase $\theta = -45^0$) and the worst (circumferential phase $\theta = +45^0$) mistuning pattern. Blade 10 produces the highest response amplitude in the best pattern, while it is blade 11 in the worst pattern. These blades share the common characteristics of low eigen-frequencies and negative mis-staggered angles. Again we observe that the circumferential mistuning phasing affects the maximum blade forced response level, which stems from the interaction between the structural mistuning and the aerodynamic mistuning.

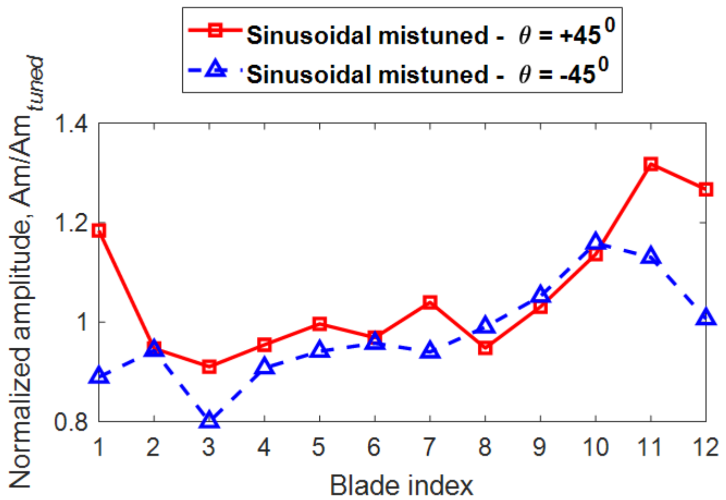

Figure 6.15: Sinusoidal mistuned response amplitude distribution.

6.4.3 Random Mistuning

Figure 6.16 compares the maximum response amplitude of the concurrently mistuned configurations of randomly varied circumferential phases. Again all mistuned configurations have a higher forced response level compared to that of the tuned cascade. An alternating-like trend in Figure 6.16 can be attributed to the near-alternating variation in the random mistuning pattern (see Figure 6.10). The maximum response amplitude difference between the best and the worst configuration is 31.6% of the tuned response level.

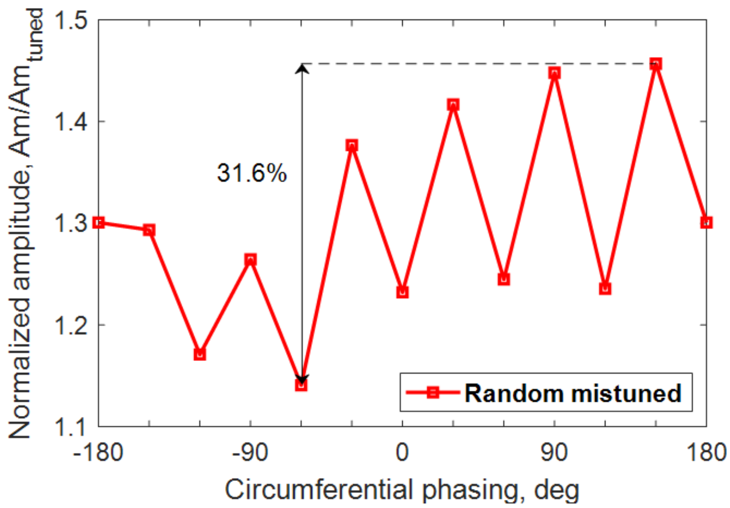

Figure 6.16: Random mistuned maximum forced response amplitude with different circumferential phasing.

Figure 6.17 presents the response amplitude distribution of all blades at the resonance peak for the best (circumferential phase $\theta = -60^0$ and the worst (circumferential phase $\theta = +150^0$) mistuning pattern. In general, the low eigenfrequency blades tend to have higher response amplitudes.

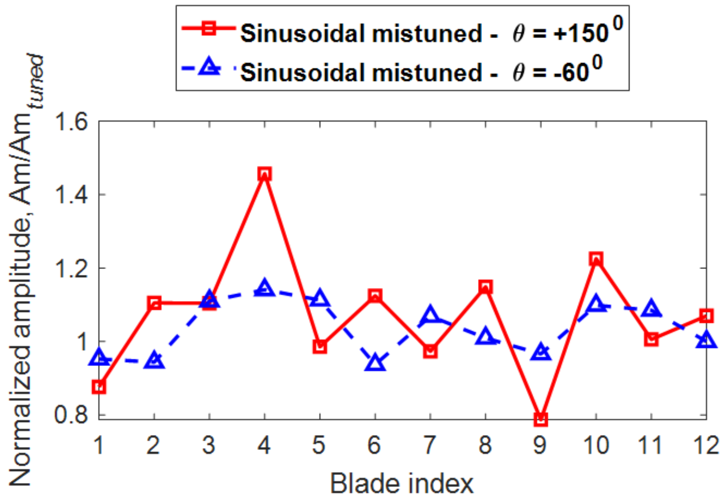

Figure 6.17: Random mistuned response amplitude distribution.

6.5 Superposability of Aerodynamic and Structural Mistuning Solutions

The results obtained in the previous sections suggest that the structural mistuning and the aerodynamic mistuning interact with each other. Since the fully-coupled fluid-structure simulation method is used to compute the forced response vibration, the nonlinear effects will be captured. On the other hand, the fully-coupled method is computationally expensive, particularly if applied to examine all possible phase angles between the two mistuning patterns. This raise a further research question: *are the nonlinear calculations necessary and is it possible to use the linear methods at least in the early design stage?* To answer the above research question, we will study the mistuning interaction in more detail, with an emphasis on the feasibility of using a simple linear superposition to construct all phasing solutions from two separately obtained solutions: one pure aerodynamic mistuning and the other pure structural mistuning.

More specifically we examine the linear superimposed solutions in comparison with the fully-coupled concurrent aero-structural solutions in terms of:

i Predicting the highest and the lowest maximum response of the blade row for all relative phasing angles considered, and further, ii Assessing if the simple linear theory predicts consistently the responses for all blades within the blade row at the two particular phasing angles of interest identified in i).

First of all, it would be useful to establish the linear superposition procedures mentioned above. The technique is merely a simple summation and post-processing of the two separate simulations of the pure structural mistuning and the pure aerodynamic mistuning respectively.

$$Am_{total}\left(m_{total}\right) = Am_{struct}\left(m_{struct}\right) + Am_{aero}\left(m_{aero}\right) \tag{6.3}$$

where $Am_{total}\left(m_{total}\right)$ is the response amplitude amplification for the concurrent mistuning of blade m_{total}; $Am_{struct}\left(m_{struct}\right)$ is the response amplitude amplification for the pure structural mistuning of blade m_{struct}; $Am_{aero}\left(m_{aero}\right)$ is the response amplitude amplification for the pure aerodynamic mistuning of blade m_{aero}.

The phasing between the aerodynamic mistuning and the structural mistuning can be obtained by simply varying the indices m_{aero} relative to m_{struct} in a postprocessing of the two solutions. Next, we will assess the validity of the linear superposition post-processing method compared against the full coupled nonlinear results including the two mistuning disturbances concurrently, for the random mistuning case.

Firstly, we will investigate the maximum response amplitudes variation with the mistuning circumferential phasing as in i) above. Figure 6.18 compares the maximum forced response amplitudes predicted by the fully-coupled and the linear superposition methods across the 360^0 range of possible circumferential phases. It is clear that the qualitative trend can be captured by the linear superposition approach. More interestingly, the best ($\theta = +150^0$) and the worst ($\theta = -60^0$) mistuning pattern are both predicted accurately in the qualitative manner. The differences between the fully-coupled and the linearly superposed indicate the nonlinear interaction between the structural and the aerodynamic mistuning as well as the capability of the fully-coupled fluid-structure simulation method for nonlinear studies.

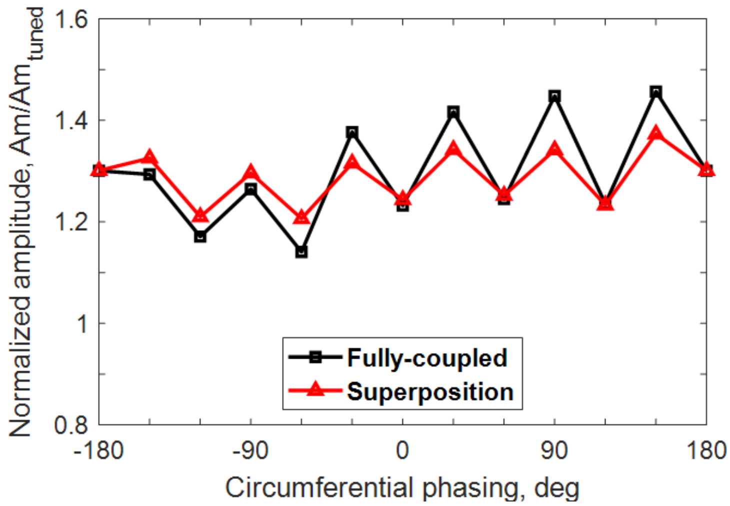

Figure 6.18: Comparison of maximum forced response amplitudes against circumferential phasing.

For ii) above, we then assess the local response amplitude distribution for two specific phasing values of interest, corresponding to the highest maximum response amplitude ($\theta = +150^0$) and the lowest maximum response amplitude ($\theta = -60^0$), as shown in Figure 6.18. Figure 6.19 presents the amplitude distributions for the best and the worst mistuning patterns as observed. It is apparent that the linear superposition can capture the variation of response amplitudes in the blade row. The superposition results are in good qualitative agreement with the fully-coupled results. Thus, it can be concluded that the linear superposition method is useful to obtain not only the global maximum response amplitude but also the local circumferential amplitude distribution of the concurrently mistuned blade row. If the structural and the aerodynamic perturbation strength is sufficiently small, the interaction can be deemed as linear. Although it has been shown in the present work that the concurrent mistuning interaction is nonlinear to a certain extent, the linear superposition has been proved to be useful to predict relatively the best or the worst combination of mistuning. Therefore, the linear superposition can act as a starting point for preliminary design considerations before the more expensive fully-coupled fluid-structure simulation method is used to assess more quantitatively the final design candidates.

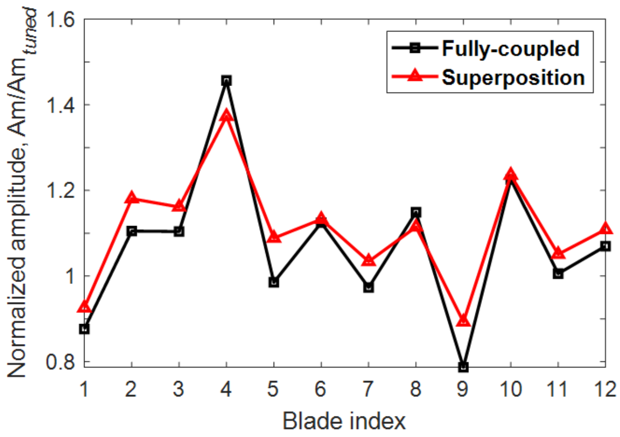

(a) Highest Maximum Response ($\theta = +150^0$)

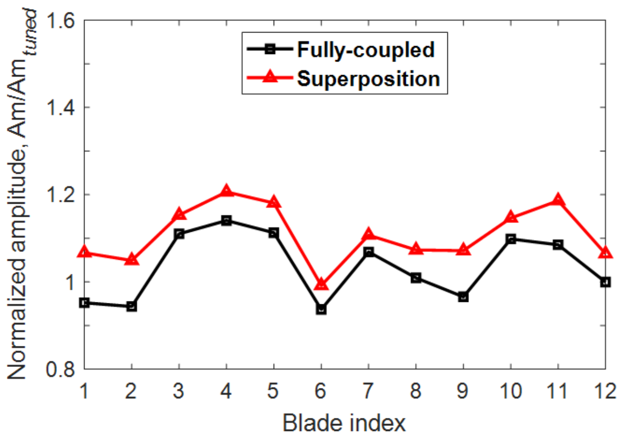

(b) Lowest Maximum Response ($\theta = -60^0$)

Figure 6.19: Comparison of forced response amplitude distributions between the fully-coupled and the superposed solutions.

6.6 Summary

For a turbomachinery bladerow, blade-to-blade variations in solid structure and fluid flow due to manufacturing and installation errors have long been a topic of wide relevance practically and academically. In the context of blade aeroelasticity, the blade-to-blade structural variation ('frequency mistuning') has been extensively studied for decades, and more recently attention has been increasingly drawn to its aerodynamic counterpart. However there seems lack of consistent and conclusive findings in relation to stabilizing or destabilizing effects and mechanisms of a mistuned blade row in general. In particular, there has been hardly any study in open literature on the characteristics of co-existent structural and aerodynamic mistuning (as well as their possible interactions), to the author's best knowledge.

In this chapter, the fully-coupled fluid-structure simulation method has been used to elucidate the vibration mechanisms of the concurrent structural-aerodynamic mistuning cascade. A fully-coupled time-domain nonlinear model is adopted intentionally so that observations can be free of the modelling assumptions commonly adopted previously.

The aerodynamic mistuning has been shown to have considerable effects on the flutter and forced response vibration characteristics of the turbomachinery blade row. More remarkably, the present work has consistently illustrated, believed to be for the first time, that the interaction between the structural and the aerodynamic mistuning would significantly alter the blade aeroelastic stability, both in the global extremes of a bladerow and in the local distributions within the bladerow. It is revealed that by the circumferential relative phasing between the two types of mistuning, one can achieve a considerably reduced forced response level or a very much enhanced aerodynamic damping for the most vulnerable blade. This effective aeroelastic control or leverage mechanism for a concurrently mistuned cascade is observed in all three mistuning patterns considered: the alternating, the sinusoidal, and the random. Table 6.1 summarizes the mistuning phasing effects between the best and the worst mistuning patterns in each aeroelastic performance category.

Table 6.1: Phasing structural-aerodynamic mistuning - Differences in response best and worst phasing.

Mistuning pattern	Flutter response (Aerodynamic damping)	Forced response (Amplitude amplification)
Alternating	16.2%	21.1%
Sinusoidal	52.7%	16%
Random	6.2%	31.6%

In addition, a further comparative study shows that the interaction between the structural and the aerodynamic mistuning exhibits some nonlinearities. However a simple linear superposition is shown to still be able to provide qualitatively consistent results in both capturing the global best and worst phasing as well as the local distribution within the blade row. Thus, a simple post-processing by superimposing two separate aerodynamic and structural mistuned solutions can still be very effectively utilised as a starting point for determining the optimum phasing.

In terms of a wider relevance, the present results suggest that the phasing between aerodynamic and structural mistuning can be utilized in a practical setting to effectively leverage aeroelastic performance. As a result, it may be used as a new design variable particularly in conjunction with certain intentional mistuning introduced in design. Furthermore the present first of the kind findings on the distinctive structural mistuning characteristics in an aerodynamically mistuned setting should also provide an extra avenue to understanding the inconclusiveness of previous observations related to the impact of frequency mistuning in more realistic configurations where aerodynamic mistuning (a blade-blade flow variation in general by design or by manufacturing tolerance) is almost inevitable.

7 Efficient Modelling for Arbitrarily Mis-Staggered Bladerow

Contents

In this chapter, the theoretical framework of the multi-scale method is extended to applications with unsteady flow and grid deformation for the first time. The newly developed method is applied to the modelling of an arbitrarily mis-staggered bladerow subject to both clean and distorted inflow conditions. Both the accuracy and the efficiency of the multi-scale method are compared against direct high-fidelity solutions.

7.1 Development of the Multi-Scale Method

7.1.1 Extended Formulation for Unsteady Flows

Unlike the steady Navier-Stokes equations in the basic form of the multi-scale method, the temporal terms are essential for the unsteady flow applications. The unsteady Navier-Stokes equations can be written in a semi-discrete form with the presence of the temporal derivative term:

$$\frac{\partial}{\partial t}\left(\boldsymbol{U}\right) + R\left(\boldsymbol{U}\right) = 0 \tag{7.1}$$

The conservative flow variable $\boldsymbol{U}$ is a seven-element vector for a three-dimensional unsteady flow with two-equation turbulence model, $\boldsymbol{U} = [\rho\ \rho u\ \rho v\ \rho w\ \rho E\ \rho k\ \rho\omega]^T$. $R\left(\boldsymbol{U}\right)$ is the lumped advection and diffusion terms.

We begin with the fine mesh simulation as in a conventional time-marching approach. If the simulation converges, the instantaneous governing equations are satisfied:

$$\frac{\partial}{\partial t}\left(\boldsymbol{U}_f\right) + R_f\left(\boldsymbol{U}_f\right) = 0 \tag{7.2}$$

Supposing the same flow domain is now discretized with a reduced spatial resolution. The poorly resolved but converged coarse mesh solution still satisfies the equations:

$$\frac{\partial}{\partial t}\left(\boldsymbol{U}_c\right) + R_c\left(\boldsymbol{U}_c\right) = 0 \tag{7.3}$$

The loss of solution accuracy when the mesh resolution reduces is obvious. Thus, in order to recover the fine mesh solution in the two-scale computation, the fine mesh solution needs to be projected to the coarse mesh discretization through volume-weighted averaging:

$$\boldsymbol{U}_{f\to c} = \frac{1}{\Delta V_c} \sum \boldsymbol{U}_f \Delta V_f \tag{7.4}$$

where the summation is taken for all the fine mesh cells of volume ΔV_f corresponding to a coarse mesh cell of ΔV_c.

The volume-weighted averaging solution $\boldsymbol{U}_{f\to c}$ to be recovered in the two-scale simulation must also satisfy Equation 7.1. However, due to the difference between the volume-averaged solution $\boldsymbol{U}_{f\to c}$ and the coarse mesh solution $\mathbf{U}_c$, the projected solution $\boldsymbol{U}_{f\to c}$ does not satisfy the discretized governing equations on the coarse mesh:

$$\frac{\partial}{\partial t}\left(\boldsymbol{U}_{f\to c}\right) + R_c\left(\boldsymbol{U}_{f\to c}\right) \neq 0 \tag{7.5}$$

Equation 7.5 can then only be balanced if a source term is introduced to the right-hand side of the equations [Ning and He, 2001]:

$$\frac{\partial}{\partial t}\left(\boldsymbol{U}_{f\to c}\right) + R_c\left(\boldsymbol{U}_{f\to c}\right) = \boldsymbol{UST} \tag{7.6}$$

where $\boldsymbol{UST}$ is the unsteady source term arisen due to the spatial resolution reduction. It is also a seven-element vector, where each entry is to balance its corresponding governing equations at anywhere in space and time.

As can be seen, the procedures are very similar to that of the baseline multi-scale method for unsteady flow. The only difference is that the discrepancy of the temporal derivative term among different scales is lumped to the source term on the right-hand side of the governing equations in addition to the existing source term to balance the $R\left(\boldsymbol{U}\right)$ term. Thus, the source term is time-varying and is denoted as the unsteady source term. It is clear now that the objective of the multi-scale approach is to introduce an appropriate spatial-temporal source term to recover the projected fine mesh solution on the coarse mesh discretization of the two-scale computation as can be seen from Equation 7.6. In the present framework, the required unsteady source term is proposed to be a summation of its elements to include effects due to multiple disturbances [L. He, 1992]. Thus, each individual constituent source term can be decoupled and pre-computed, which enables the required total source term to be estimated in an efficient manner:

$$\boldsymbol{UST}_{total} = \overline{\boldsymbol{UST}} + \sum_{i=1}^{N_d} \boldsymbol{UST}_i \tag{7.7}$$

where $\overline{\boldsymbol{UST}}$ is the time-averaged source term. $\boldsymbol{UST}_i$ is the varying source term due to each disturbance i. N_d is the number of disturbances that the flow field is subject to.

Because previous works on the multi-scale method only attempt to deal with a steady or time-averaged flow field, the method has been extended to deal with an unsteady flow as well as a grid perturbation in the current work. To the author's knowledge, this is the first time such capability of the multi-scale method has been proposed and also implemented in the framework of a commercial solver. In the current work, the disturbance can be arisen due to change in the blade stagger angle or due to the influence of external perturbation (e.g. inlet distortion). Calculation of each term in Equation 7.7 will be discussed in the next section.

7.1.2 Stagger Angle-Dependence Source Term

As outlined in the methodology chapter, the Influence Coefficient Method (ICM) [Hanamura et al., 1980] has become the most common method in getting equivalent tuned cascade data from experimental linear cascades and annular sector rigs with only one blade oscillating. Its classical use is to calculate the 1st harmonic unsteady pressure coefficient of the reference blade Cp_1 in a travelling wave mode by summing the unsteady pressure coefficients from the oscillating blade itself and its neighboring stationary blades, taking into account the constant inter-blade phase angle (IBPA):

$$Cp_1 = \sum_{m=-N/2}^{+N/2} Cp_1\,(m)\, e^{-im\sigma} \tag{7.8}$$

where m is the blade number index. N is the total number of blades in the whole annulus assembly. σ is the constant IBPA defined as positive for a forward travelling wave mode.

In our proposed approach, the unsteady source term due to blade re-staggering will be linearly superimposed in the similar manner to the classical ICM:

$$\mathbf{UST}_{stagger} = \sum_{m=-N/2}^{+N/2} \mathbf{UST}\,(m)\, e^{-i\sigma_m} \tag{7.9}$$

where $\boldsymbol{UST}\,(m)$ is the unsteady source term arisen in blade passage m due to the motion of the reference blade B0. σ_m is the relative IBPA between the blade $\mathrm{B_m}$ and the reference blade $\mathrm{B_0}$.

At the special conditions when the IBPA is constant throughout the bladerow, Equation 7.9 becomes similar to the original form of the classical ICM. The physical significance of the proposed approach is that the instantaneous response of the reference blade can be reconstructed using the known relative positions between the reference blade and its neighbors.

To calculate the staggering-dependence source term, the direct fine mesh solution of the ICM-based cascade needs to be calculated first. Similar to the classical ICM approach, only the middle blade is re-staggered, while the adjacent blades are kept stationary. Figure 7.1 shows the schematic illustration of the method with two adjacent blades retained on each side of the central blade. A five-blade configuration is usually deemed to be sufficient due to the convergence of influence coefficients away from the central blade. At each instantaneous re-staggering movement of the central blade, the effects on itself and on the adjacent blades are recorded (see Figure 7.1). The ICM-based fine mesh solution is projected onto the coarse mesh, thus enables the calculation of the source term $\boldsymbol{UST}\,(m)$ for each blade passage.

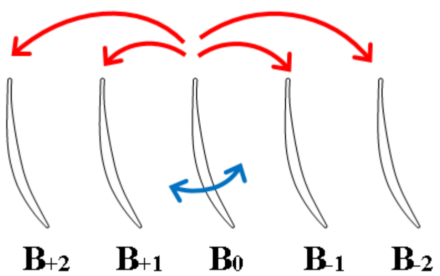

Figure 7.1: Illustration of the influence coefficient method for blade deformation.

Then in the whole annulus configuration, each blade can be re-staggered in any arbitrary way. The total source term applied to a reference passage $\boldsymbol{UST}_{stagger}$ is a linear superposition of each individual passage's source term (Equation 7.9). Figure 7.2 shows the illustration of the source term superposition technique. In this example, only effects of the two closest adjacent blades on each side are taken into account, in accordance with the way the source term is calculated in the pre-calculation phase.

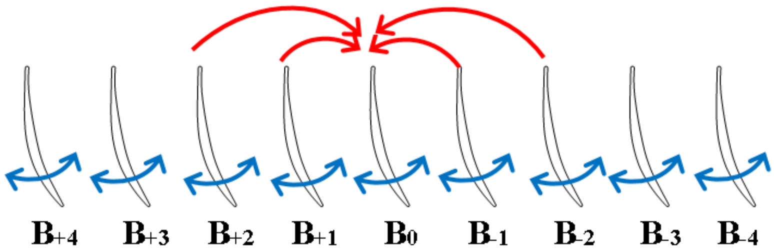

Figure 7.2: Illustration of source term superimposition in a mis-staggered bladerow.

Note that the uniformly staggered assembly does not necessarily mean each blade stagger angle must be exactly the same. Each blade can have a constant stagger angle change such that the whole bladerow is harmonically perturbed. This is then reduced to the conventional concept of travelling wave introduced by Lane [Lane, 1956] and can be solved efficiently using the common phase-shifted approach. The travelling wave tuned cascade will also be validated with the two-scale method and compared with the established tuned cascade simulation method.

7.1.3 Inlet Distortion-Dependence Source Term

The inlet distortion simulation represents the situation in which the bladerow is subject to a circumferentially non-uniform flow field. Because no blade-to-blade variation is considered in the pre-calculation of the inlet distortion-dependence source term, it can be solved using the phase-shift single-passage simulation or solved directly using the whole annulus simulation. In the former case, the source term can be calculated as in the temporal Fourier method, whereas the spatial Fourier transform method can be used in the latter case. Figure 7.3 presents the whole annulus uniformly staggered bladerow subject to a non-uniform circumferential inlet stagnation pressure P_0 with a wavelength of a whole circumference.

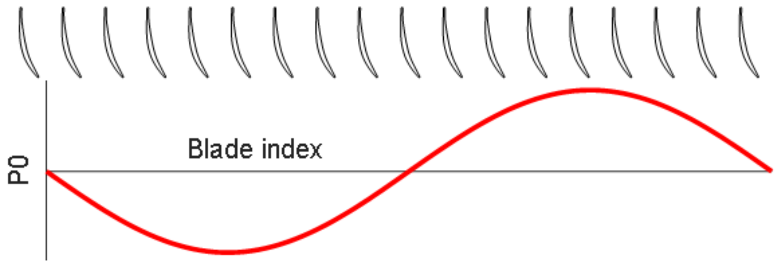

Figure 7.3: Bladerow under inlet distortion.

Performing discrete Fourier transform at any instantaneous time level, the inlet distortion-dependence source term can be calculated using the available circumferential positions:

$$\boldsymbol{UST}_{distortion} = \sum_{n=1}^{N_\theta} \left[A_{\boldsymbol{U},\theta} \cos(n\theta_m) + B_{\boldsymbol{U},\theta} \sin(n\theta_m) \right] \tag{7.10}$$

where $\theta_m = 2\pi(m-1)/N$. Note that N_θ is the number of retained spatial harmonics and $2N_\theta + 1 \leq N$.

7.1.4 Unsteady Source Term Computation and Storage in the Frequency-Domain

At a physical time instant m, the unsteady source term comprises a time-averaged component $\overline{\boldsymbol{UST}}$ and a fluctuating component $\boldsymbol{UST}'$:

$$\frac{\partial}{\partial t}(\boldsymbol{U}_m) + R(\boldsymbol{U}_m) = \overline{\boldsymbol{UST}} + \boldsymbol{UST}' \tag{7.11}$$

The temporal derivative is calculated using the second-order backward Euler approach:

$$\frac{\partial}{\partial t}(\boldsymbol{U}_m) = \frac{1}{\Delta t}(1.5\boldsymbol{U}_m - 2\boldsymbol{U}_{m-1} + 0.5\boldsymbol{U}_{m-2}) \tag{7.12}$$

where Δt is the physical timestep.

The fluctuating component of the unsteady source term is then converted from the time-domain to the frequency-domain by Fast Fourier Transform following the work of He [1990]:

$$\boldsymbol{UST}' = \sum_{n=1}^{N_f} \left[A_{\boldsymbol{U}} \cos(n\omega t) + B_{\boldsymbol{U}} \sin(n\omega t) \right] \tag{7.13}$$

where N_f is the number of Fourier harmonics retained of the considered disturbance; ω_i is the disturbance angular frequency.

Thus, the source term due to each disturbance can be efficiently represented by a Fourier series of sufficiently high number of harmonics as in Equation 7.13. Mostly the 1st harmonic of the source term has been used in the current work. An assessment on the influence of high-harmonic terms will be conducted in a later part.

7.1.5 Practical Implementation

The central idea of the two-scale method is around the use of two disparate mesh resolutions. In the current implementation, the boundary layer region is chosen as the region of interest due to the typical requirement of sufficiently fine mesh to resolve the boundary layer on the blade surfaces. Figure 7.4a shows the fine mesh resolution used in the direct fine mesh computation. Figure 7.4b presents the coarse mesh resolution used in the two-scale method computation. The mesh has about 90k nodes for each 2D single passage fine mesh domain, whereas this is about 30k for each 2D single passage coarse mesh domain. In Figure 7.4, the mesh resolution near the blade surfaces can be clearly contrasted between the two domain discretization. The fine mesh in the boundary layer region ($y^+ < 1$) allows the boundary layer to be resolved directly. However, the coarse mesh with a few elements in the boundary layer region would utilise the wall function model and deteriorate the results.

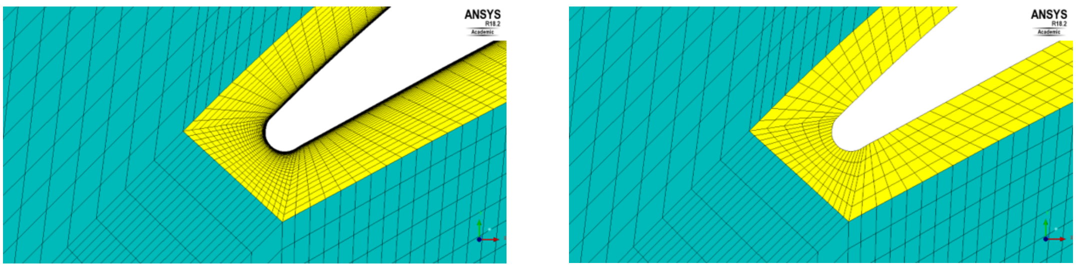

(a) Fine mesh **(b)** Coarse (also multi-scale) mesh

Figure 7.4: Mesh resolution in the boundary layer region of configurations with different scales.

7.2 Case 1 - Uniformly Staggered Cascade

7.2.1 Validation of Steady/Time-Averaged Source Term

The laminar bubble separation was reported to appear on the compressor blade suction surface in the experiment [Yang and He, 2004] at a low Reynolds number testing condition. In the previous chapter, it was also shown that the two-equation $\gamma - \theta$ transition correlation coupled with the SST model [Menter et al., 2004] is also able to predict the formation of separation bubble. The ability to calculate the steady source term and use it in the two-scale simulation to recover the fine mesh solution needs to be assessed. The total source term now only includes the steady component:

$$\boldsymbol{UST}_{total} = \boldsymbol{UST}_0 \tag{7.14}$$

Figure 7.5a shows the comparison of mid-span steady pressure distribution between the direct fine mesh solution and the two-scale method with the fully turbulent model, whereas Figure 7.5b presents the same comparison with the transitional model. For both turbulence models, the two-scale method shows excellent agreement with the fine mesh. For fully turbulent solution in Figure 7.5a, the mesh resolution does not take an important role. The coarse mesh solution mildly deviates from the fine mesh solution, with the largest difference in the front part of the suction surface. In contrast, mesh resolution plays a pivotal role in the prediction of transitional flow. From Figure 7.5b, the suction surface pressure distribution is distinctively different between the fine mesh and coarse mesh solution.

The axial velocity contours between the fine mesh and coarse mesh solution with transitional model are presented in Figure 7.6. While fine mesh solution predicts a rather small separation bubble, the coarse mesh solution predicts a much bigger separation bubble and a more downstream transition onset. This is in agreement with the observed pressure distribution in Figure 7.5b and in line with the requirement of sufficient mesh resolution by the $\gamma - \theta$ transitional model [Menter et al., 2004].

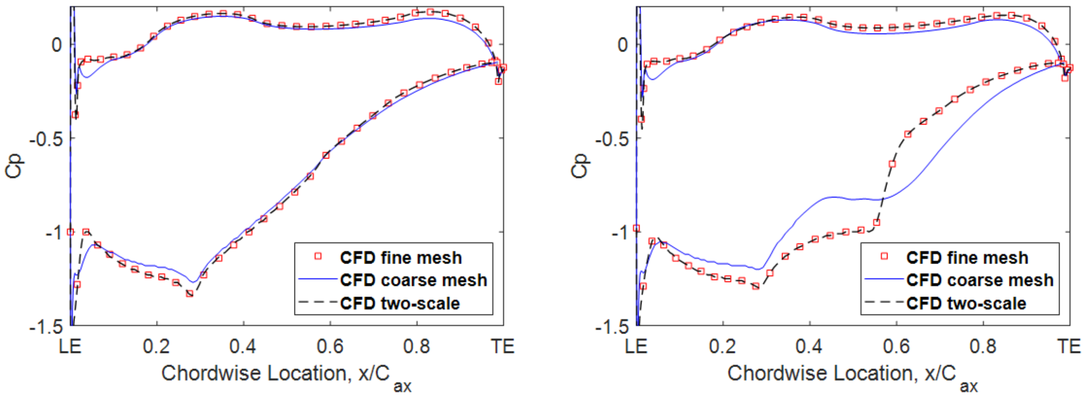

(a) Fully-turbulent (b) Transitional

Figure 7.5: Mid-span static pressure distribution of different configurations.

(a) Fully-turbulent

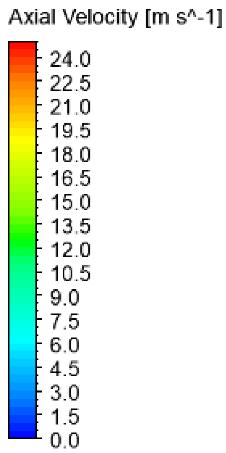

(b) Transitional

Figure 7.6: Mid-span static pressure distribution of different configurations.

7.2.2 Validation of Source Term Superimposition

The linear superposition validity as in the classical ICM has been studied experimentally and numerically extensively and will not be a subject of interest of the current work. In the current implementation, we propose an approach to use the ICM to perform linear superimposition on the source term in an attempt to reconstruct a flow field of an arbitrarily mis-staggered bladerow. Because this is the first time such approach is used, validation works need to be done. Firstly, the two-scale solutions of finite-cascade ICM will be evaluated. The source term $\boldsymbol{UST}_m$ for each blade m is reconstructed based on the desired maximum number of harmonics N_f:

$$\boldsymbol{UST}_m = \sum_{n=1}^{N_f} \left[A_{\mathbf{U},m} \cos\left(n\omega_i t\right) + B_{\mathbf{U},m} \sin\left(n\omega_i t\right)\right] \tag{7.15}$$

The torsional mode is chosen to illustrate a strong dependency of aerodynamic damping on the mesh resolution, which will be discussed more in detail later. Another modeling interest is the assessment on the number of harmonics of the source term. The transitional model is adopted in this part to compare the 1st and 2nd harmonic unsteady flow responses.

Figure 7.7 presents the overall damping curve for different configurations at the oscillating reduced frequency $k = 0.8$. A drastic difference between the predictions of fine mesh and coarse mesh solution can clearly be observed. Although not presented here, the strong dependency of flutter susceptibility on the mesh resolution has been confirmed with a fully coupled fluid-structure interaction model. On the other hand, two-scale solutions greatly improve aero-damping prediction for all IBPAs. With the use of 2nd harmonic source term, the overall aero-damping prediction does not change. This behaviour will be examined more closely with the tuned cascade configuration.

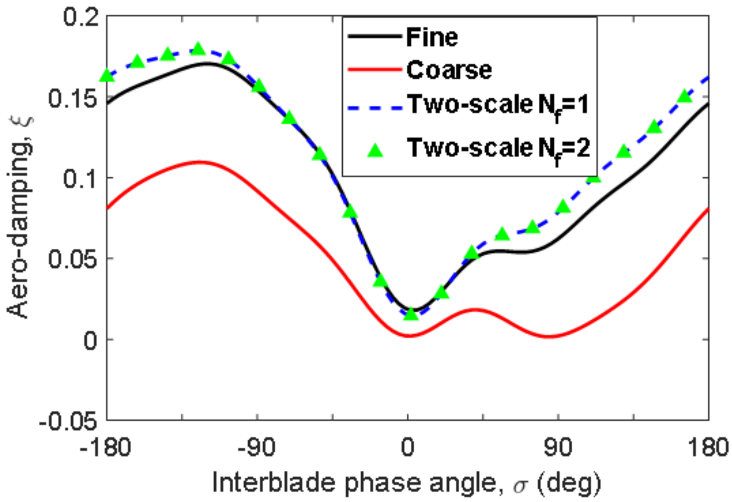

Figure 7.7: Overall aerodynamic damping of different models at $k = 0.8$.

Next, the tuned cascade is considered, such that all blades are uniformly staggered with a constant IBPA. The total source term applicable to a reference blade passage now has the form:

$$\boldsymbol{UST}_{total} = \overline{\boldsymbol{UST}} + \sum_{m=-2}^{+2} \boldsymbol{UST}\,(m)\, e^{-im\sigma} \tag{7.16}$$

The total source term applied into each passage is thus constant with a phase shift equal to the IBPA. Figure 7.8 presents the 1st harmonic response of the unsteady pressures at the reference blade. From Figure 7.8, the majority of discrepancy among investigated configurations exists on the blade suction surface. The coarse mesh predicts an erroneous trend of aero-damping distribution compared to that predicted by the fine mesh. On the other hand, the two-scale solution with 2nd harmonic source term ($N_f = 2$) is identical to that with only the 1st harmonic source term ($N_f = 1$).

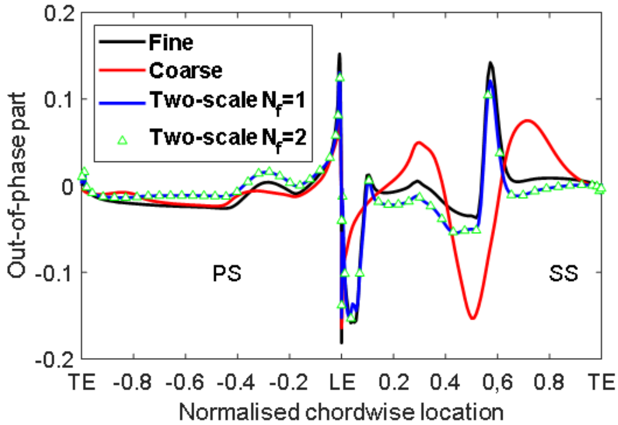

(a) Out-of-phase component

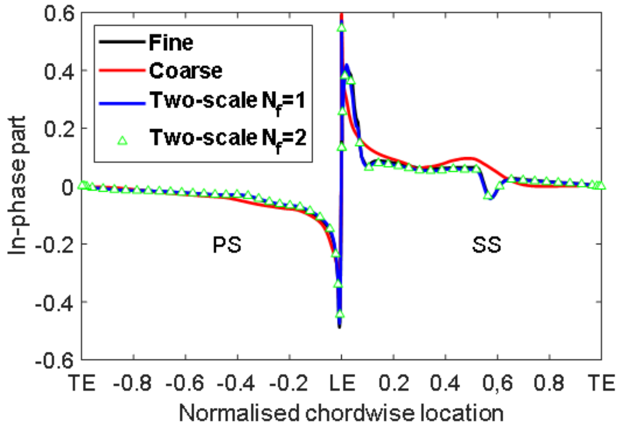

(b) In-phase component

Figure 7.8: 1st harmonic unsteady pressure responses.

Figure 7.9 presents the 2nd harmonic response of the unsteady pressures at the reference blade. It can be seen that using the 1st harmonic source term ($N_f = 1$) is no longer sufficient in this case, although its prediction is already a great improvement compared to the direct coarse mesh simulation. With the addition of 2nd harmonic source term ($N_f = 2$), the 2nd harmonic response comparable to that of the fine mesh is recovered by the two-scale solution. However, it can be shown that high-harmonic unsteady pressures do not contribute to the overall aero-damping, which is also evidenced from the aero-damping curve (Figure 7.7). In addition, the investigated flow field is predominantly linear even with the separation bubble such that the high-harmonic terms do not significantly influence the fundamental harmonic term. Thus, it can be concluded that the use of 1st harmonic source term is sufficient for aero-damping calculation, at least for this test case. If one wish to include high-harmonic effects, the high harmonic source terms might be used for an improved prediction.

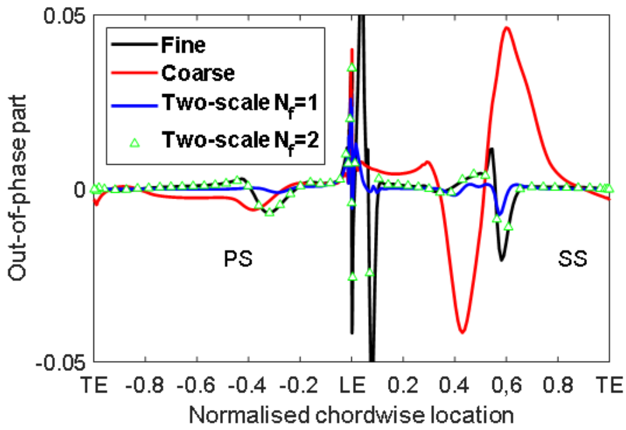

(a) Out-of-phase component

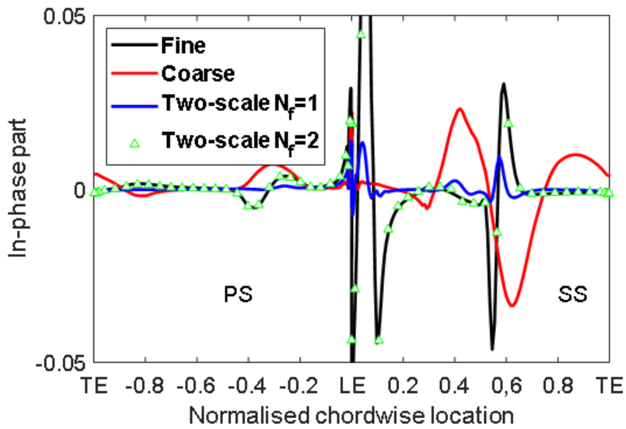

(b) In-phase component

Figure 7.9: 2nd harmonic unsteady pressure responses.

7.3 Case 2 - Arbitrarily Mis-Staggered Bladerow (Clean Inlet Flow)

In this example, the compressor bladerow comprised of 18 blades is arbitrarily mis-staggered from the nominal position by a random pattern. Figure 7.10 presents the mis-staggering pattern for each individual blade. The nominal stagger angle for the uniform bladerow is 14.2^0. Each blade is re-staggered randomly within the maximum range of $\pm 1^0$ deviated from the nominal position. The amplitude of mis-staggering is within the typical range of that used in the literature [Lu et al., 2019; Wilson et al., 2007]. Figure 7.11 shows the schematic illustration of the mis-staggering pattern in the whole-annulus bladerow with an amplification factor of 10 to emphasize the random difference between the mis-staggered blades and their uniform counterpart.

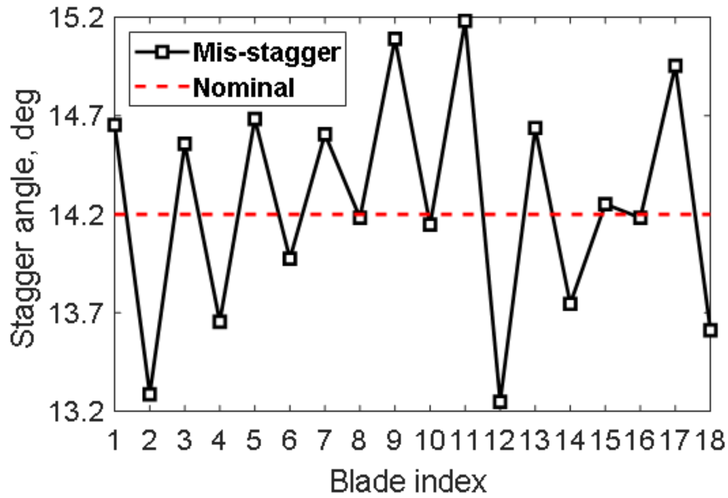

Figure 7.10: Stagger angle distribution in the arbitrarily mis-staggered bladerow.

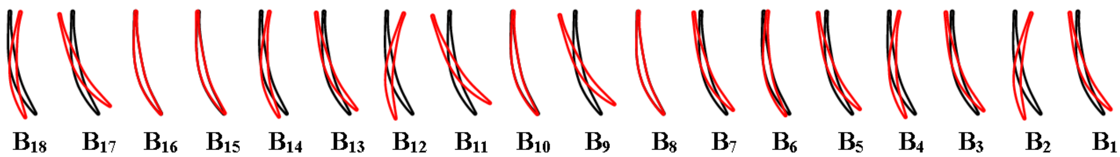

Figure 7.11: Arbitrarily mis-staggered bladerow pattern with an amplification factor of 10.

The total source term used in the two-scale method now has two constituent terms as shown in Equation 7.17. The first term is the averaged source term, while the second term is associated with the change in stagger angle. The second term is evaluated using the source term superimposition method described in the method formulation section for an arbitrarily mis-staggered assembly.

$$\boldsymbol{UST}_{total} = \overline{\boldsymbol{UST}} + \boldsymbol{UST}_{stagger} \tag{7.17}$$

Figure 7.12 presents the steady lift force generated by all blades in the arbitrarily mis-staggered bladerow by simulations with different mesh resolution compared to that predicted by the two-scale method. The lift force for the uniform bladerow is also plotted to study the influence of stagger angle variation itself on the aerodynamics quantity of interest. The steady blade force is normalized by the isentropic exit dynamic head and the blade chord length.

$$F = \frac{\int_A p \, dA}{(P_{01} - P_2)\, C^2} \tag{7.18}$$

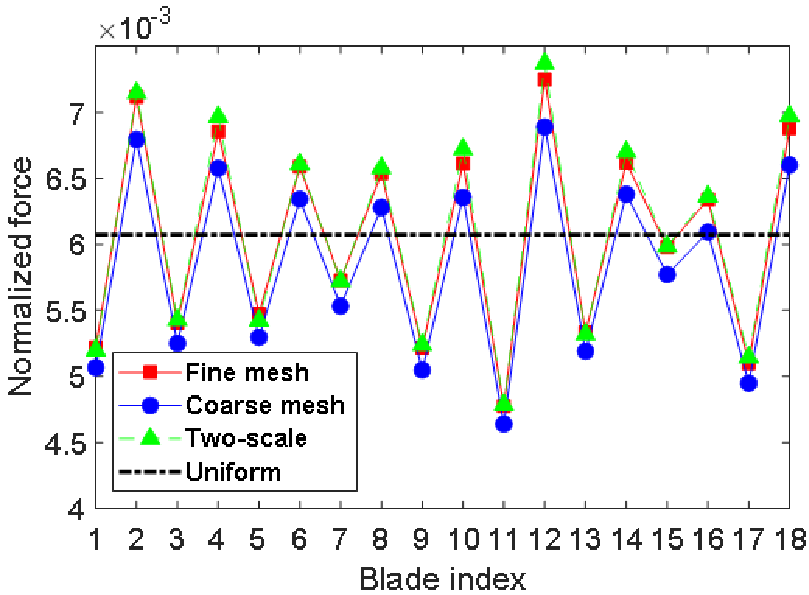

Figure 7.12: Steady lift force distribution in the arbitrarily mis-staggered bladerow.

Each individual blade lift force is seen to diverge from their nominal value in the uniform bladerow. Their alternating fluctuation distributions from the nominal values can be attributed to the near-alternating stagger variation pattern (see Figure 11 and 12), which suggests that the influence of on-itself component is dominant. Thus, the change in steady lift force of a reference blade can be easily related to the effects of quasi-steady change in incidence angle of itself. When the stagger angle increases (e.g. Blade 9, Blade 11), the blade is subject to a negative incidence leading to a lower lift force. Vice versa, when the stagger angle decreases (e.g. Blade 4, Blade 12), the blade is subject to a positive incidence leading to a higher lift force. Another interesting point can be made based on the observation of those blades with small deviation from the nominal position (e.g. Blade 10, Blade 15, Blade 16). Although the difference between their relative stagger angles with the nominal position is rather small (less than 0.4%), their blade forces vary much more significantly (e.g. up to 9% for Blade 10). Blade 10 and Blade 15 also have two contrasting variation trends compared to their counterpart in the uniform bladerow. This finding confirms that the influence of a mis-staggered blade can propagate throughout the bladerow and affect their neighbors. Thus, it is important that sufficient neighboring blades have to be taken into account to reconstruct the response of the reference blade.

Although the maximum mis-staggering amplitude is only 1 degrees, the computation of mis-staggered bladerow reveals that the individual blade lift force can be drastically increased or reduced. For example, Blade 11 reduces 21.4% of its blade force compared to the uniform bladerow, while Blade 12 increases by 19.3%. The remaining blades have their increase or reduction percentage fluctuated in the range $\pm 10 - 15\%$.

Regarding the main interest of the current study on the accuracy of the proposed two-scale method, it can be seen that the use of two-scale method greatly improves the prediction accuracy of the direct coarse mesh solution. The solution of two-scale method usually differs from the direct fine mesh solution by less than 1% in the current computational example. Thus, the applicability of the source term superimposition method has been validated to be suitable for an arbitrarily mis-staggered bladerow subject to the clean inflow condition.

7.4 Case 3 - Uniformly Staggered Bladerow (With Inflow Distortion)

7.4.1 Quasi-Steady Rotating Inlet Distortion

In this example, the compressor bladerow with uniform stagger angle distribution is subject to the stagnation pressure inlet distortion with the wavelength equal to the bladerow circumference (e.g. Figure 6.1). Equation 7.19 shows the formula for the inlet stagnation pressure distortion:

$$P_{01} = P_{01,uniform} + \Delta P_{01} \sin(\omega t + \theta_i) \tag{7.19}$$

where $P_{01,uniform}$ is the inlet total pressure at clean inflow condition. ΔP_{01} is the amplitude of the distortion perturbation, which is taken to be equal to 30% of the inlet stagnation pressure at clean inflow condition. θ_i is the relative phase angle between the i^{th} and the first pitchwise grid line.

The total source term used in the two-scale method now has two constituent terms as shown in Equation 7.20. The first term is the averaged source term, while the second term is associated with the change in inlet stagnation pressure due to inlet distortion. The second term is evaluated using the spatial Fourier transform method described in the method formulation section.

$$\boldsymbol{UST}_{total} = \overline{\boldsymbol{UST}} + \boldsymbol{UST}_{distortion} \tag{7.20}$$

Figure 7.13 shows the instantaneous lift force evolution of the reference blade during one passing period of the inlet distortion. Because the bladerow is uniformly staggered, all blades are subject to the same force with a constant phase shift. It is observed in this case that the blade force can change drastically by ±30% the value of its nominal force in the clean inflow condition. Thus, the induced dynamic stress arisen will be significantly affect the blade durability during its service life, possibly leading to a premature failure with High Cycle Fatigue if no counter-measure would be taken. On the other hand, it is noted that the predicted averaged blade force during the inlet distortion period is similar to that predicted earlier by the computation with clean inflow condition. This finding suggests that the non-linearity in the computed case is low, even when subject to a large disturbance amplitude of 30% of the inlet stagnation pressure at clean inflow condition. Under the influence of the inlet distortion, the two-scale method still shows its applicability to improve the prediction accuracy using a coarse mesh computation to less than 1% compared to the direct fine mesh solution.

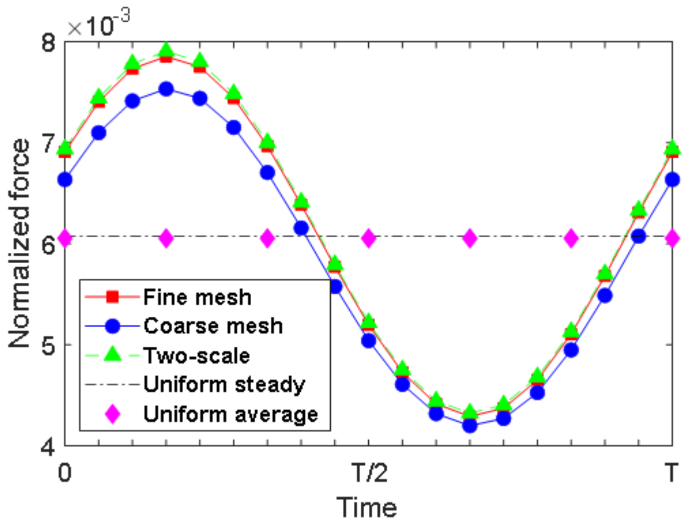

Figure 7.13: Unsteady lift force evolution during one period of quasi-steady inlet distortion in the uniformly staggered bladerow.

7.4.2 Unsteady Rotating Inlet Distortion

Here the inlet distortion is moved with a high reduced frequency $k = 0.5$ calculated based on the reference isentropic outlet velocity V_{ref} in the clean inflow condition. This is the representative case of a rotor bladerow subject to the inlet distortion. The total source term used in this example is still in the form of Equation 7.20. However, due to a highly unsteady effect, the temporal term $\frac{\partial}{\partial t}(\boldsymbol{U})$ has a bigger influence in the governing equations. In contrast, if the flow can be regarded as steady or quasi-steady, the temporal term will vanish and the governing equations reduce to:

$$R(\boldsymbol{U}) = 0 \tag{7.21}$$

Since this is the first time the multiscale method has been extended to consider the unsteady flow effects in the framework of a commercial solver, the capability to calculate such term needs to be validated. Figure 7.14 shows the instantaneous lift force evolution of the reference blade during one passing period of the inlet distortion with high reduced frequency $k = 0.5$.

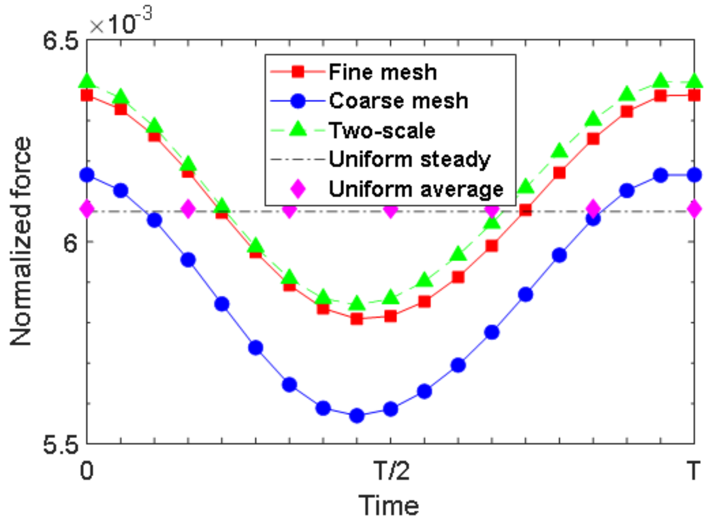

Figure 7.14: Unsteady lift force evolution during one period of inlet distortion at $k = 0.5$ in the uniformly staggered bladerow.

It can be observed in this case that the peak-to-peak force during one period is smaller compared to the case with quasi-steady inlet distortion (Figure 7.14 vs Figure 7.13). The maximum unsteady force amplitude is reduced to within the range $\pm 5\%$ the value of its nominal force in the clean inflow condition. Note that the unsteady inlet distortion amplitude is still comparable to the quasi-steady inlet distortion case (30% amplitude of clean inflow stagnation pressure). Under the high frequency inlet distortion, the distortion passes through the compressor bladerow with the attenuated distortion strength. In the literature, this phenomena is known as stagnation pressure attenuation when the distortion pattern travels downstream the compressor bladerow [Fidalgo et al., 2012; Plourde and Stenning, 1968; Yao et al., 2010]. On the other hand, the high similarity between the steady and time-averaged blade force confirms the predominant linearity of the problem, even with the high reduced frequency and the high distortion amplitude. Moreover, the two-scale method still shows its capability to improve the prediction accuracy using a coarse mesh computation to less than 1% compared to the direct fine mesh solution.

7.5 Case 4 - Arbitrarily Mis-Staggered Bladerow With Inflow Distortion

In this example, the arbitrarily mis-staggered compressor bladerow is subject to the rotating inlet distortion with the wavelength equal to the bladerow circumference (similar to that in Case 3). The mis-staggering pattern is the same as that used in the previous example (similar to that used in Case 2, e.g. Figure 7.10). The inlet stagnation pressure distortion formula is also similar to the previous examples. The total source term used in the two-scale method now has three constituent terms as shown in Equation 7.22. The first term is the averaged source term, the second term is related to the change in stagger angle, and the third term is associated with the change in inlet stagnation pressure.

$$\boldsymbol{UST}_{total} = \overline{\boldsymbol{UST}} + \boldsymbol{UST}_{stagger} + \boldsymbol{UST}_{distortion} \tag{7.22}$$

Figure 7.15 shows the instantaneous lift force evolution of Blade 11 and Blade 12 in the mis-staggered bladerow during one passing period of the inlet distortion with high reduced frequency $k = 0.5$. It is observed that the time-averaged blade forces in the mis-staggered bladerow are markedly different from that in the uniformly staggered bladerow. Two consecutive Blade 11 and Blade 12 even show a qualitatively different trend in the time-averaged force. Although mis-staggering effect induces a reduction in the time-averaged blade force in Blade 11, there is an increase in the time-averaged blade force in Blade 12 due to mis-staggering. It has been confirmed from the previous computational examples that the nonlinearity in the currently investigated bladerow is small, thus we would expect a slight difference between the steady and time-averaged flow prediction. Recall the distribution of blade forces in the mis-staggered bladerow at the steady flow environment (see Figure 13), it is clear that the steady blade force of Blade 11 and Blade 12 also show the same trend in blade force deviation from the nominal uniformly staggered bladerow.

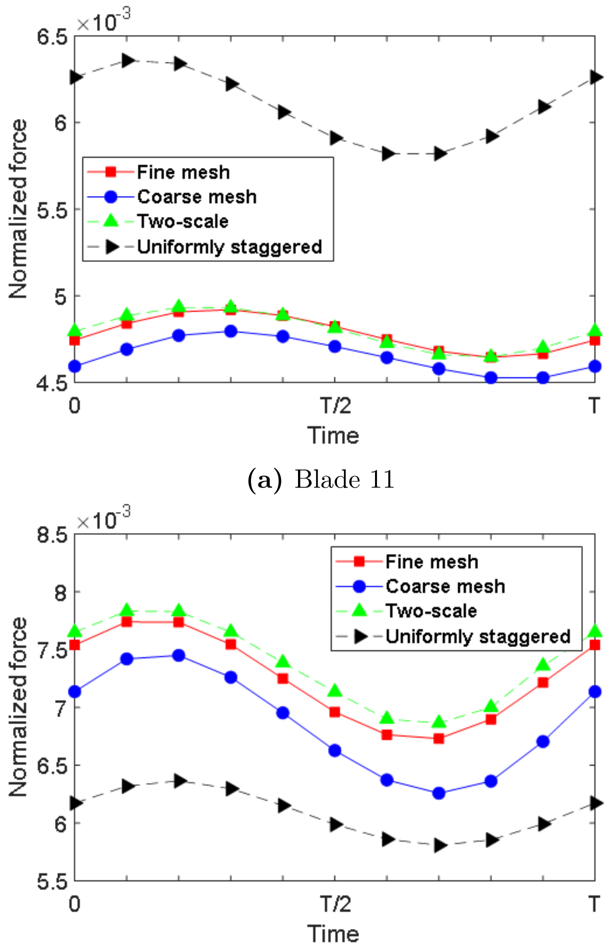

(a) Blade 11

(b) Blade 12

Figure 7.15: Unsteady lift force evolution during one period of inlet distortion at k=0.5 in the mis-staggered bladerow.

On the unsteady blade force distribution, it is interesting to note that the unsteady evolution is also qualitatively different between the mis-staggered and the uniformly staggered bladerow. The blade dynamic response (phase change) can be seen from Blade 11 (Figure 7.15a) in contrast to Blade 12 (Figure 7.15b) by examining the locations of blade force peak and trough with respect to their uniform counterpart.

The comparison between the two-scale method and the direct solution again shows the highly accurate prediction capability of the two-scale method. The time-averaged and the unsteady blade force is comparable to that predicted by the direct fine mesh solution, whereas the direct coarse mesh solution is clearly lack of the quantitative agreement with the fine mesh solution. To illustrate the capability of the two-scale method on the whole flow field prediction, Figure 7.16 shows the instantaneous static pressure discrepancy ΔP between the coarse mesh and the two-scale method in comparison with the direct fine mesh solution.

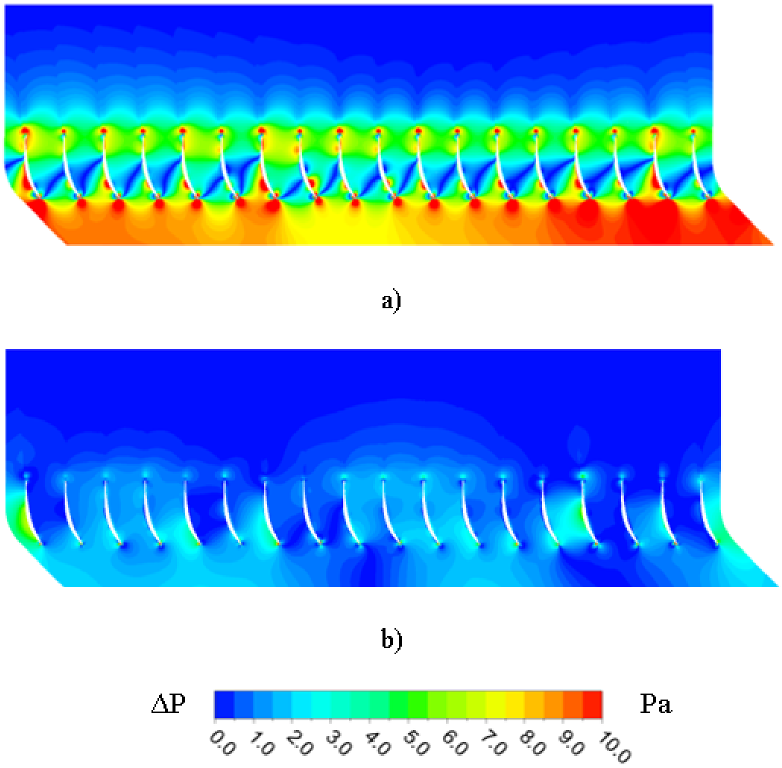

Figure 7.16: Instantaneous static pressure discrepancy from a direct fine mesh solution for: a) coarse mesh and b) two-scale solution.

It is clearly observed that the coarse mesh has a higher discrepancy to the fine mesh solution (Figure 7.16a against Figure 7.16b), in agreement with the results presented in previous discussions. The majority of static pressure discrepancy clusters around the blade region as well as upstream of the bladerow. This high discrepancy reflects that the blade-to-blade aerodynamic coupling is poorly predicted in the direct coarse mesh solution. This poor prediction stems from the poorly resolved boundary layer region, then propagates upstream (where the same mesh resolution is used for all simulation setup), and then deteriorates the whole flow field prediction.

7.6 Further Discussions on Computational Gains

The objective of the proposed method is to predict the steady and unsteady flow field more accurately and more efficiently. The accuracy has been investigated in various computational examples including the uniformly staggered and the arbitrarily mis-staggered bladerow subject to clean inflow condition as well as inlet distortion. In all cases, the method has been shown to improve the quantitative prediction of the direct coarse mesh simulation. The accuracy is almost comparable to the direct fine mesh solution as if the whole annulus of the arbitrarily mis-staggered bladerow is solved using a high-resolution spatial discretization.

Regarding the computational efficiency of the proposed method, it is clear that the memory and CPU time would be smaller than that used by the direct fine mesh simulation because of the reduction in mesh count used by the two-scale method. Furthermore, in the current implementation, it has also been observed that the computational saving can be potentially increased due to a faster convergence rate with the coarse mesh discretization. As a result, the total computational saving factor achieved is between 6 to 15 compared to the direct fine mesh simulation; whereas the memory saving is a factor of 3 thanks to the mesh count reduction brought in by the coarse mesh discretization.

7.7 Summary

Accurate and efficient modeling of a bladerow with random blade-to-blade variations subject to either clean inflow conditions or inlet distortion has continuously been a challenge for turbomachinery CFD. The current work addresses this challenge by developing an approach based on the multiscale principle in the framework of a commercial solver.

The method relies on balancing the governing equations with an appropriate spatial-temporal source term to compensate the error arisen due to spatial averaging and projection of the targeted fine mesh solution on the coarse mesh discretization. In the current framework, we propose that the source term can be a summation of the constituent source terms corresponding to each flow perturbation. The source term corresponding to blade staggering is a linear superimposition of the source terms from the current blade passage and from its neighbors, based on the use of Influence Coefficient Method. On the other hand, the source term corresponding to inlet distortion is related to spatial Fourier transform of the whole annulus bladerow.

The key enabler is that the source term only needs to be computed using a small training set of identical blade passages. For the staggering-dependence source term, a high-resolution five-passage configuration with the re-staggered middle blade needs to be calculated. For the inlet distortion-dependence source term, a full annulus configuration or a phase-shifted single passage configuration subject to the inlet distortion has to be computed. Using the source terms calculated from an identical passage configuration, the total applicable source terms are then superimposed and reconstructed at each known spatial and temporal location for any arbitrarily mis-staggered bladerow subject to inlet distortion at the expense of little extra cost. Thus, the steady and unsteady flow field of the mis-staggered bladerow subject to inlet distortion can be efficiently computed.

The summative capability of the source term is validated with the computational examples including the uniformly staggered, and the arbitrarily mis-staggered bladerows subject to either a clean inflow condition or an inlet distortion. The computational results of the two-scale method are in a quantitative agreement with the direct fine-mesh solution, with a clear accuracy improvement compared to the base coarse mesh simulation. The fundamental harmonic source term has been shown to be sufficient for an aero-damping calculation. The high harmonic source terms can be easily included, should one wish to improve unsteady flow field prediction.

The results also reveal marked differences in steady and unsteady flow response between the uniformly staggered and the randomly mis-staggered bladerow, thus reinforce the need to study the inlet distortion effects in the presence of the stochastic blade-to-blade variations. Some qualitative and quantitative comparisons are summarized here to highlight the effects of the mis-staggering:

1. There are $\pm 20\%$ differences in the steady/time-averaged blade forces between the uniformly staggered and the mis-staggered bladerow at clean inflow condition. Either a reduction or an increase in steady/time-averaged blade force can be present in the mis-staggered bladerow depending on the local stagger angle of each individual blade.

2. At a high reduced frequency of inlet distortion, the amplitude of unsteady blade force is reduced. For example, blade force unsteady amplitude decreases to 5% from 30% of the nominal value if the reduced frequency increases to 0.5 in comparison with the quasi-steady inlet distortion (at the same inlet distortion strength). In addition, the mis-staggering also induces a variation in the blade dynamic response (phase change) if the bladerow is subject to the inlet distortion.

On the computational efficiency of the two-scale method, it has been shown that the computation gain comes from the mesh reduction as well as the faster convergence rate. Consequently, the total computational saving in the current implementation of the two-scale method can be up to 15 times faster in comparison with the corresponding direct fine mesh solutions.

8

Efficient Modelling of Mistuned Blade Aeroelasticity Using Fully-Coupled Multi-Scale Method

Contents

In this chapter, the implementation of the multi-scale method is extended to the fully-coupled fluid-struture interaction simulation method. The newly developed method is applied to the forced response modelling of a fully-coupled mistuned bladerow under an inlet distortion. Both the accuracy and the efficiency of the multi-scale method are compared against direct high-fidelity solutions.

8.1 Development of the Multi-Scale Method for Fully-Coupled Fluid-Structure Simulations

The practical integration of the multi-scale method in the fully-coupled workflow is presented in Figure 8.1. Compared to the original workflow of the partitioned fluid-structure approach, the multi-scale method introduces the source terms to the fluid solver (highlighted in red). It can be noted that the vibration-independent and vibration-dependent source term are implemented at different stages of the workflow. The steady/time-average and the vibration-independent source term are implemented within the inner loop iteration. On the other hand, the vibration-dependent source term is implemented at the outer loop level. The underlying reason of this procedure is that the vibration-dependent source term will be updated based on the blade vibration characteristics (e.g. vibration frequency, amplitude, phase angle) after each physical time step. Typically this involves an embedded Fast Fourier Transform (FFT) operation after the outer loop iteration. Once the blade vibration characteristics are identified, the vibration-dependent source term can be scaled accordingly. The calculation procedures of vibration-independent and vibration-dependent source term will be presented in the next section.

Note that the influence coefficient truncated-domain direct simulation in the pre-computing stage has a prescribed oscillation with a known vibration amplitude and frequency. However, the fully-coupled solution would lead to vibration with a different amplitude (i.e. resonance against non-resonance) and frequency (i.e. frequency shift) at a different condition when the inlet distortion's frequency is swept through a potential range. To enable the application of the source term computed with the uncoupled influence coefficient cascade to the fully-coupled solutions without repeating many pre-computing simulations, certain assumptions are made:

i The source term coefficients are unchanged with vibration frequencies;

ii The source term coefficients scale linearly with the vibration amplitude.

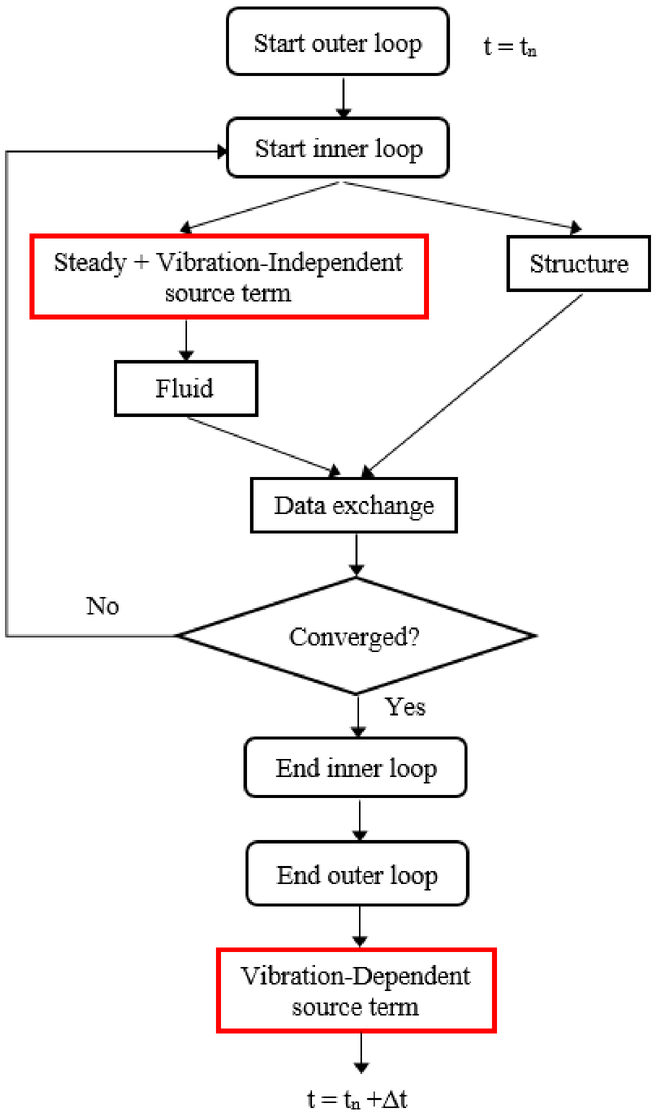

Figure 8.1: Flow chart of the fully-coupled multi-scale method.

The first assumption is valid because the frequency shift is typically small, thus the source term coefficients can be assumed to be constant with vibration frequency. The second assumption is justified because the response amplitudes are typically small enough to be within the linear range. It is imperative to realise that a new influence coefficient cascade with the prescribed value of amplitude and frequency of interest can be recomputed to obtain more accurate source terms. However, these two above assumptions enable an efficient modelling method using a limited number of data available during the pre-computing phase.

8.2 Simulation Setup

The fully-coupled multi-scale methodology is implemented in the commercial solver CFX. The simulation domain comprises of 12 blade passages. The boundary conditions are similar to the typical simulations as outlined in the methodology chapter. To enable the forced response calculation, a rotating inlet stagnation pressure distortion P_{01} with imposed distortion amplitude and frequency. The circumferential extent of one spatial period of inlet distortion covers 4 blade passages (i.e. a 12-passage domain has 3 periods of inlet distortion in the circumferential direction)

$$P_{01} = P_{01,uniform} + \Delta P_{01} \sin\left(\omega t + \theta_i\right) \tag{8.1}$$

where $P_{01,uniform}$ is the stagnation pressure at uniform inflow condition. ΔP_{01} is the distortion amplitude, which is taken to be equal to 10% of $P_{01,uniform}$. ω is the distortion rotating frequency and is swept near the blade natural frequency range to find its resonance response. θ_i is the relative phase angle between the i^{th} and the first pitchwise grid line.

In the current implementation, the boundary layer zone is chosen as the region of interest due to the typical requirement of sufficiently fine mesh to resolve the boundary layer on the blade surfaces. Figure 8.2 highlights the application zone of the multi-scale method. For the fine mesh computation, this boundary layer region is resolved for $y^+ < 1$. For the coarse and multi-scale computations, this zone is coarsened in the wall normal direction (by a factor of 20). The under-resolved coarse mesh with a few elements in the boundary layer region would need to use the wall function model to approximate the near-wall region. The uncalibrated empirical wall function model could lead to erroneous results depending on the flow conditions as well as the surface regularities. It will be shown in the present work that the coarse mesh over-predicts the chordwise extension of mid-span bubble separation, which results in erroneous predictions of the unsteady flow characteristics.

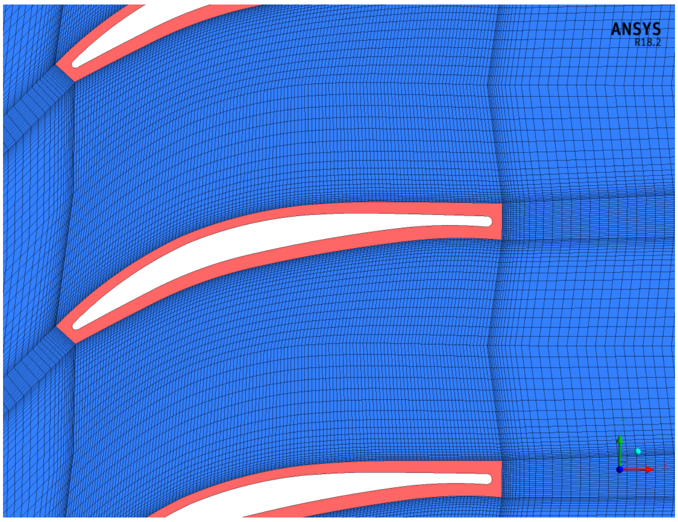

Figure 8.2: Mesh resolution of the multi-scale method applied to the boundary layer region.

8.3 Case 1 - Tuned Bladerow

The fully-coupled multi-scale method is first applied to the classical tuned cascade, in which all blades have the same eigen-frequency, amplitude, and interblade phase angle. The distortion frequency is swept in the range close to the blade eigen-frequency. Figure 8.3 shows the overall forced response curve of the tuned cascade.

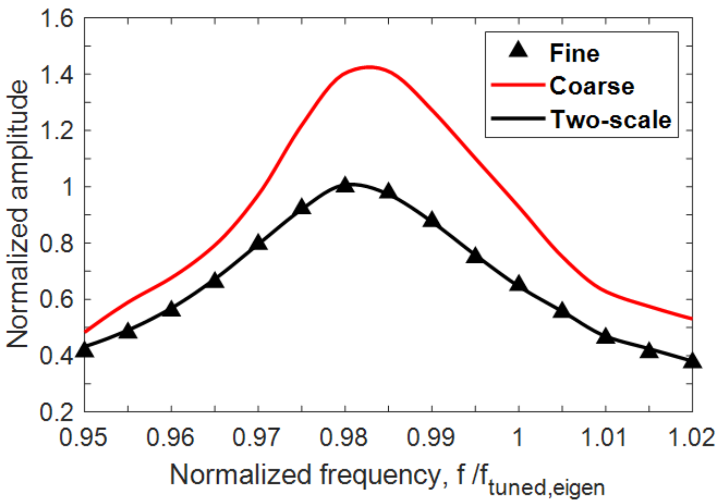

Figure 8.3: Overall forced response curve of the tuned bladerow.

The overall forced response curve has a bell shape, which indicates that the response amplitudes are higher near the resonance peak and getting smaller as moving away from the resonance. The x-axis in Figure 8.3 represents the distortion frequency normalised to the eigen-frequency of the tuned cascade. It can be seen that the resonance peak does not take place at unity normalised frequency but at a slightly different frequency. This difference is known as the frequency shift, which is related to the fluid-structure coupling effects [Moffatt and He, 2005; Chahine et al., 2019]. Regarding the prediction of forced response amplitude, the y-axis in Figure 8.3 is normalised by the maximum amplitude predicted by the fine mesh simulation of the tuned cascade. The base coarse mesh simulation predicts a 50% higher amplitude response at the resonance peak compared to the fine mesh simulation. On the other hand, the newly developed multi-scale method prediction is in good quantitative agreement with the fine mesh simulation for the whole forced response curve. The location and amplitude of the resonant peak are well-predicted by the fully-coupled multi-scale method.

Figure 8.4 shows the detailed unsteady pressure distribution on the blade surfaces at the resonance peak. Figure 8.4a presents the out-of-phase component, while Figure 8.4b presents the in-phase component of the 1st harmonic unsteady pressure. It is clear that the multi-scale method predictions closely resemble that of the direct fine mesh simulation, whereas the coarse mesh predicts a qualitatively erroneous result in the mid-chord suction surface region. Thus, it can be said that the dynamic effects of the separation bubble can lead to over-prediction of the forced response amplitude.

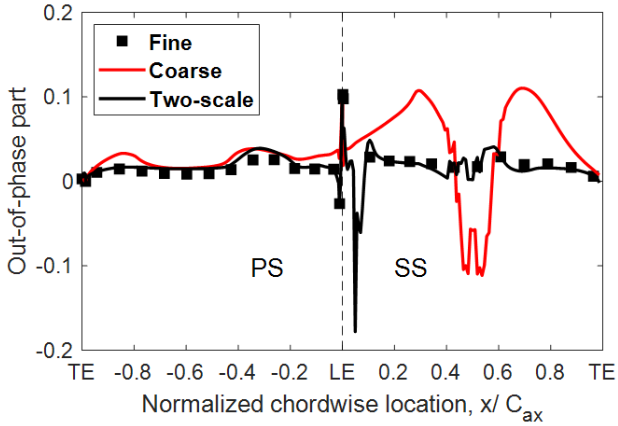

(a) Out-of-phase component

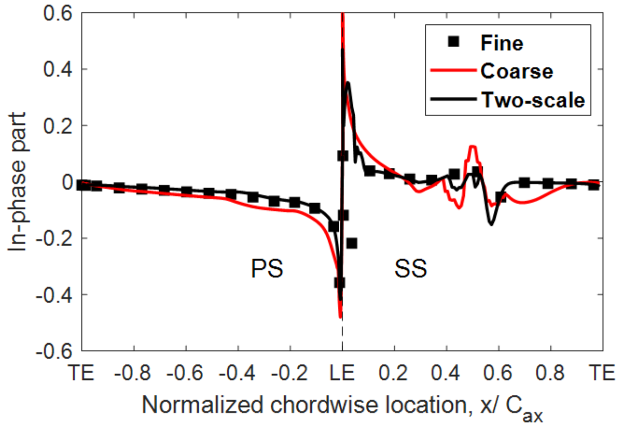

(b) In-phase component

Figure 8.4: 1st harmonic unsteady pressure responses on the blade surfaces of the tuned bladerow.

8.4 Case 2 - Alternatingly Mistuned Bladerow

In this section, we start to investigate the mistuned bladerow, which is the main focus of the thesis. In case 2, an alternating pattern of mistuning is used. This is the representative configuration of the intentional mistuning pattern for passive flutter alleviation [Corral et al., 2018. Figure 8.5 shows the alternating mistuning pattern in comparison with its tuned counterpart. The mistuned eigen-frequency is within the range of ±1% deviated from that of tuned of bladerow.

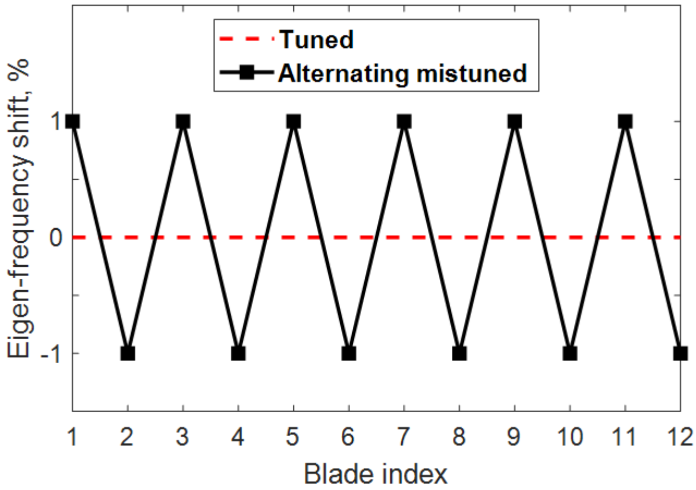

Figure 8.5: Pattern of the alternating frequency mistuned bladerow.

First, we'll explore what one would expect to observe in the forced response curve of the mistuned cascade. Figure 8.6 shows the overall forced response curve of the alternating mistuned cascade. Since there are only two blade configurations of high and low eigen-frequency, we can clearly identify two separate curves corresponding to each blade. The first thing to note in Figure 8.6 is the shift of resonance peaks. Odd-numbered blade has a higher eigen-frequency (see Figure 8.5) and thus reaching a resonance peak at higher frequency compared to the tuned cascade (Figure 8.6 vs Figure **??**). A similar observation can be made for the even-numbered blade with lower eigen-frequency. Moreover, since the peak amplitude is of interest in the forced-response problems, we begin to turn our attention to the y-value of the curves. The mistuned response amplitude is normalised by the maximum tuned response amplitude. Therefore, a normalized amplitude higher than unity indicates an amplitude amplification factor, which represents the adverse effects of the mode localization phenomenon. The amplitude amplification can be seen around the peak responses of the mistuned blades, which reaches up to 20% higher than the tuned response for the current test case condition. Note that the amplification factor can be much higher depending on the mistuning level as well as the blade-to-blade coupling strength as shown in chapter 5.

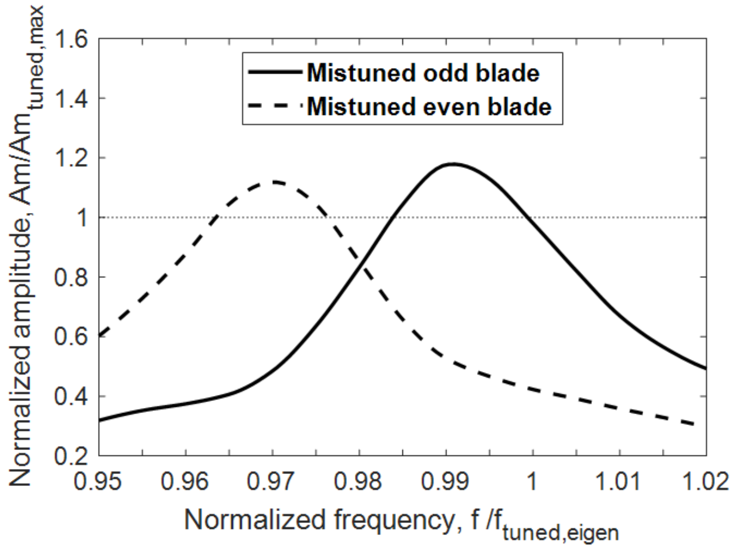

Figure 8.6: Overall forced response curve of the alternating frequency mistuned bladerow.

Figure 8.7 shows the comparisons of overall forced response curves predicted with different modeling fidelities. Figure 8.7a is the set of curves corresponding the odd-numbered blade, while Figure 8.7 represents that of the even-numbered blade. It can be seen that the fully-coupled multi-scale method can significantly improve the response prediction compared to the base coarse mesh. The base coarse mesh predicts a fairly good response far away from the resonance peak. However, at vicinity of the resonance peak, the coarse mesh solution is highly erroneous with the response amplitude few times larger than that predicted by the fine mesh solution (up to 4 for the even-numbered blade).

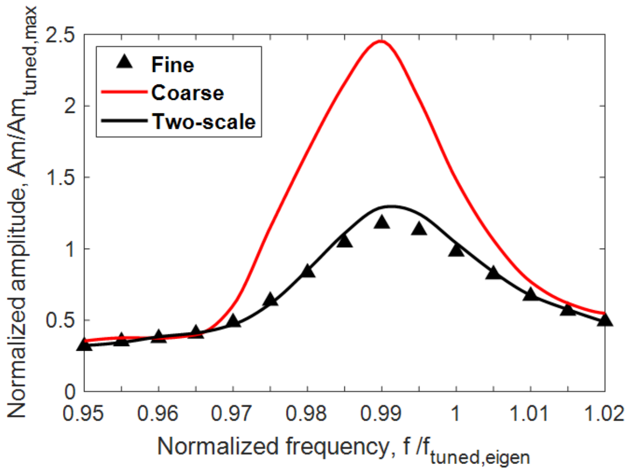

(a) Odd-numbered blade

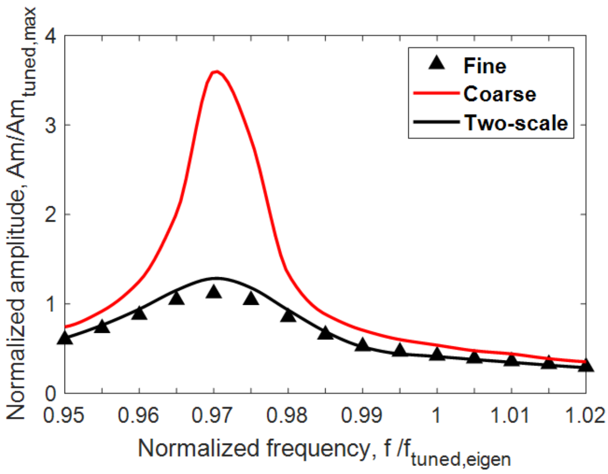

(b) Even-numbered blade

Figure 8.7: Overall forced response curves of the alternating frequency mistuned bladerow predicted by different fidelities.

Figure 8.8 and Figure 8.9 show the detailed unsteady pressure distribution on the blade surfaces at 97% normalized frequency for the odd-numbered and even-numbered blade, respectively. This is the condition where the even-numbered blade reaches it resonance peak. It can be observed that the fully-coupled multi-scale method can improve the local unsteady pressure distribution greatly for both cases. Unlike the case of tuned bladerow, this time the discrepancies exist all over the entire blade surfaces.

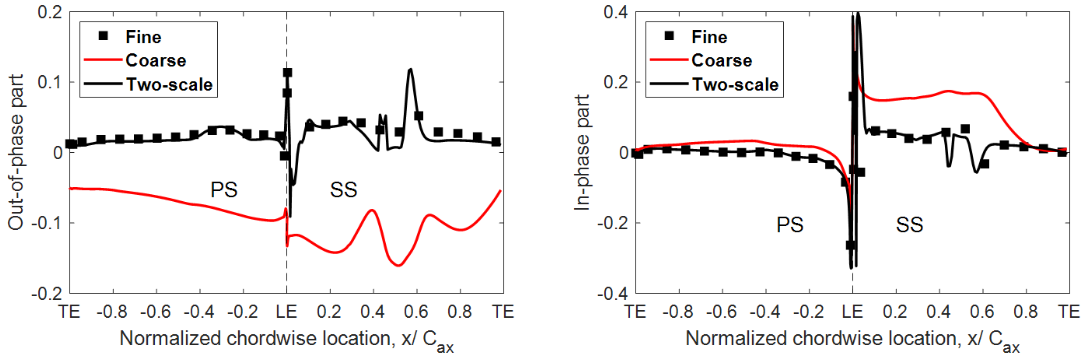

(a) Out-of-phase component **(b)** In-phase component

Figure 8.8: 1st harmonic pressure responses on the odd-numbered blade surfaces of the alternating frequency mistuned bladerow.

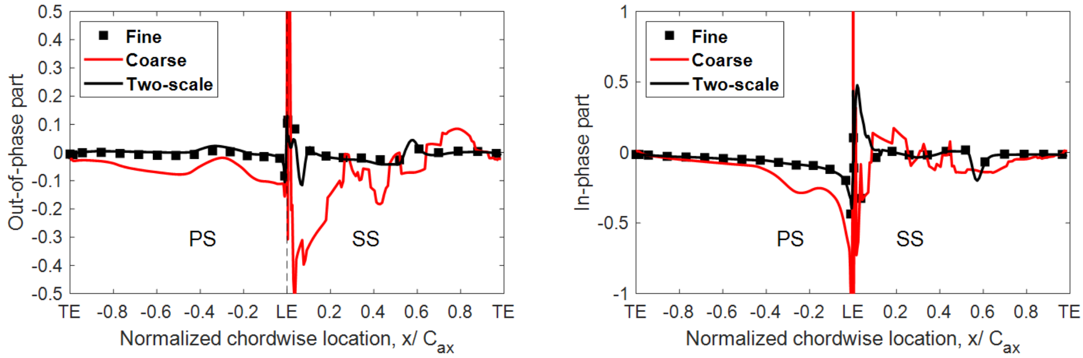

(a) Out-of-phase component **(b)** In-phase component

Figure 8.9: 1st harmonic pressure responses on the even-numbered blade surfaces of the alternating frequency mistuned bladerow.

8.5 Case 3 - Randomly Mistuned Bladerow

Finally, we'll apply the fully-coupled multi-scale method on the randomly mistuned bladerow. This is a more realistic scenario because of the probabilistic nature of mistuning. Figure 8.10 shows the pattern of the random frequency mistuning used in case 3. The randomly mistuned eigen-frequency is assumed to lie within the range of $\pm 1\%$ deviated from that of tuned of bladerow.

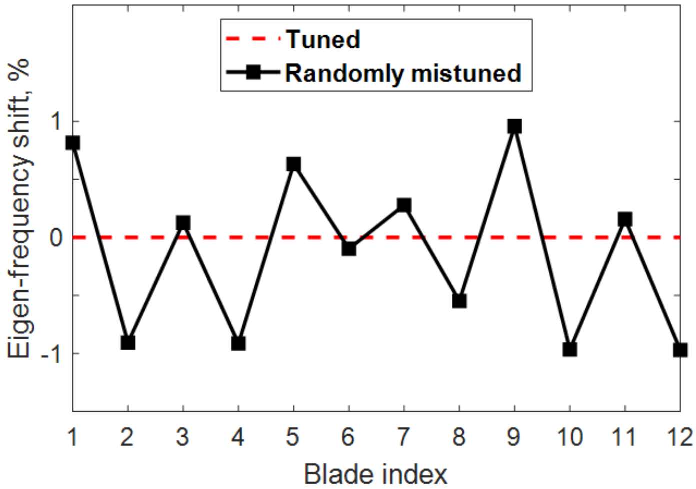

Figure 8.10: Pattern of the random frequency mistuning case.

Figure 8.11 shows the overall forced response curve of the randomly mistuned cascade bounded by the maximum amplitude at each respective frequency. The fully-coupled multi-scale method is shown to improve the prediction accuracy significantly compared to the base coarse mesh. The coarse mesh predicts high vibration amplitudes up to 5 times different from what would be expected from the direct fine mesh solution. On the other hand, the multi-scale method has a comparable accuracy to the fine mesh solution.

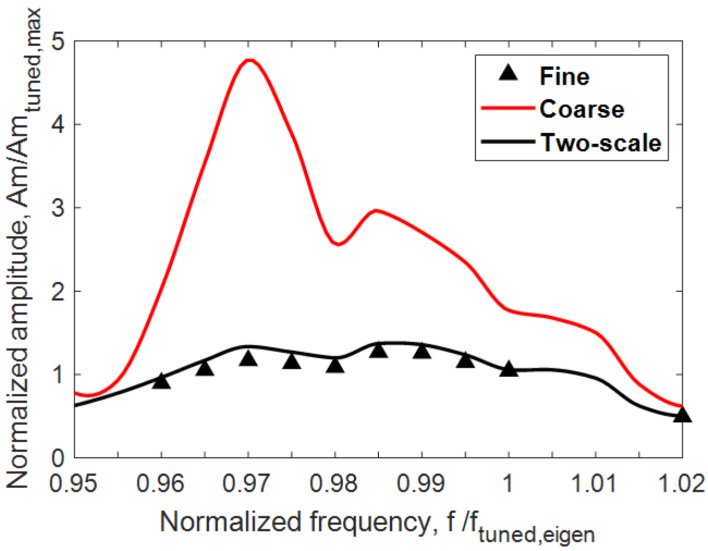

Figure 8.11: Overall forced response curves of the random frequency mistuned bladerow predicted by different fidelities.

To further investigate the vibration kinematics of the random mistuning case, we shall look at each individual blade's dynamic as shown in Figure 8.12. First thing to note is that the forced response level of the randomly mistuned bladerow is amplified up to the factor of 1.5 compared to the tuned bladerow. Secondly, the individual blade's response largely split into two main groups: one with higher eigen-frequencies and the other with lower eigen-frequencies compared to the tuned bladerow. The high-frequency group clusters on the right side of Figure 8.12, while the low-frequency group clusters on the left side. This is in agreement with the observation in the alternatingly mistuned case, where the frequency mistuning scatters the blade responses according to their eigen-frequencies. It can also be seen that most of the blades have higher amplitude responses than the tuned blade.

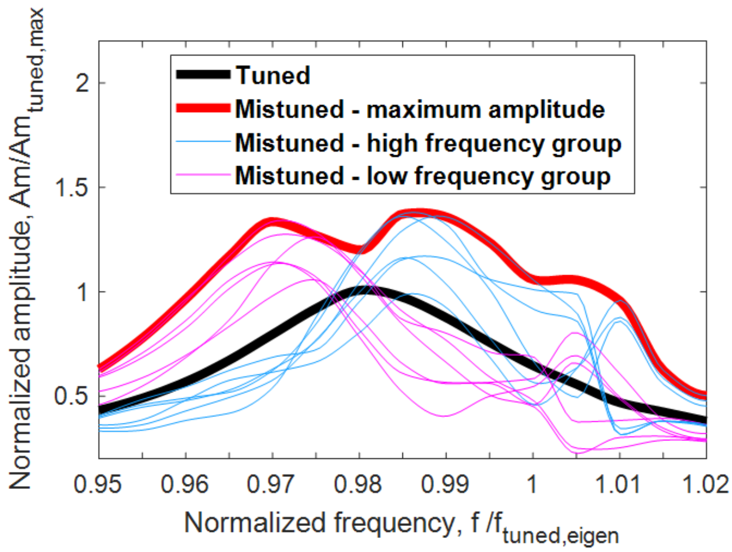

Figure 8.12: Overall forced response curves of the random frequency mistuned bladerow.

Figure 8.13 shows the detailed unsteady pressure distribution on the blade surfaces at the resonance peak. Figure 8.13a presents the out-of-phase component, while Figure 8.13b presents the in-phase component of the 1st harmonic unsteady pressure. Apparently the multi-scale method predictions are in good agreement with the direct fine mesh simulation. On the other hand, the coarse mesh simulation predicts a substantially different result, particularly on the blade suction surface. These local differences add up to produce a much larger amplitude response in the coarse mesh.

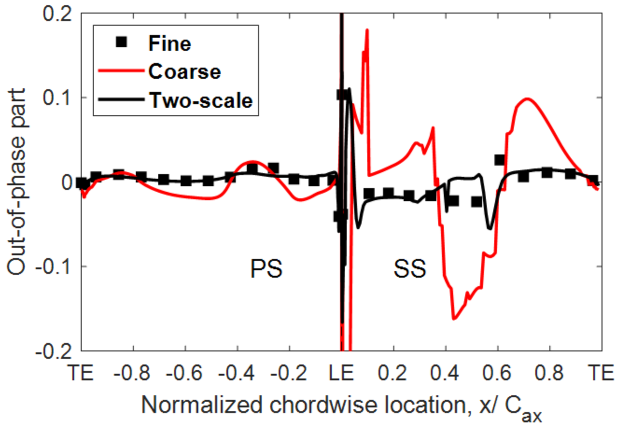

(a) Out-of-phase component

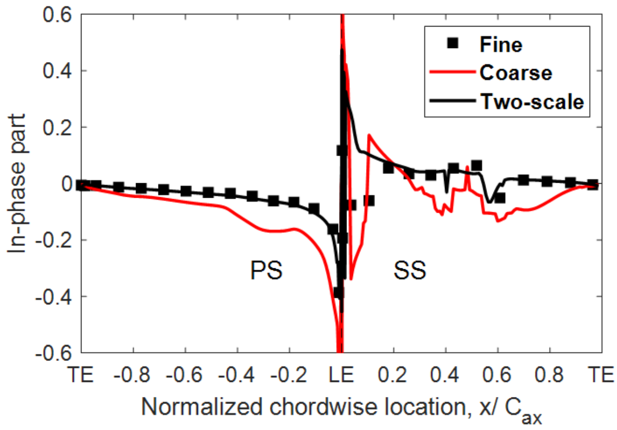

(b) In-phase component

Figure 8.13: 1st harmonic pressure responses on the max-amplitude blade surfaces of the randomly mistuned bladerow.

Figure 8.14 compares the instantaneous entropy function contour predicted by different modeling fidelities. Three high entropy peaks and troughs can be observed passing through the bladerow, in agreement with the imposed inlet distortion pattern. Although the overall entropy distribution of the direct coarse mesh simulation looks qualitatively similar to that of the fine mesh, we pay attention to some notable discrepancies. Firstly, the wakes predicted by the coarse mesh are significantly thicker than that of the direct fine mesh. Note that the mesh resolution in the wake regions are the same for all modeling configurations. The disparate mesh resolution is only applied to the boundary layer zone (see Figure 8.2). Thus, it can be deduced that the near-wall coarsen boundary layer region does not only deteriorate the blade loading but also propagate errors downstream, further into the wake mixing region. This observation somewhat agrees with the previous finding using the uncoupled method, in which the coarse mesh's static pressure errors were seen to propagate both upstream and downstream of the bladerow. For this particular test case and condition, this discrepancy stems from the over-prediction of the bubble separation size in the coarse mesh simulation, thus creating a large low-momentum region on the blade suction surface that leaves the trailing edge and thickens the wake. Secondly, the coarse mesh simulation predicts an asymmetric wake mixing pattern, highlighted by the circle near the bladerow exit. This asymmetric distribution is produced by the interaction between the passing entropy waves and the blade wakes (thus also the blade vibrations). Remarkably, both two aforementioned discrepancies between the fine and coarse mesh simulations do not exist for the fully-coupled multi-scale method. This finding suggests that the new method has corrected the error in the base coarse mesh computation. Moreover, the interactions between the inlet distortion and the blade vibration can be reproduced by the multi-scale method despite of its uncoupled approach to determine separately the source term attributed to each flow disturbance.

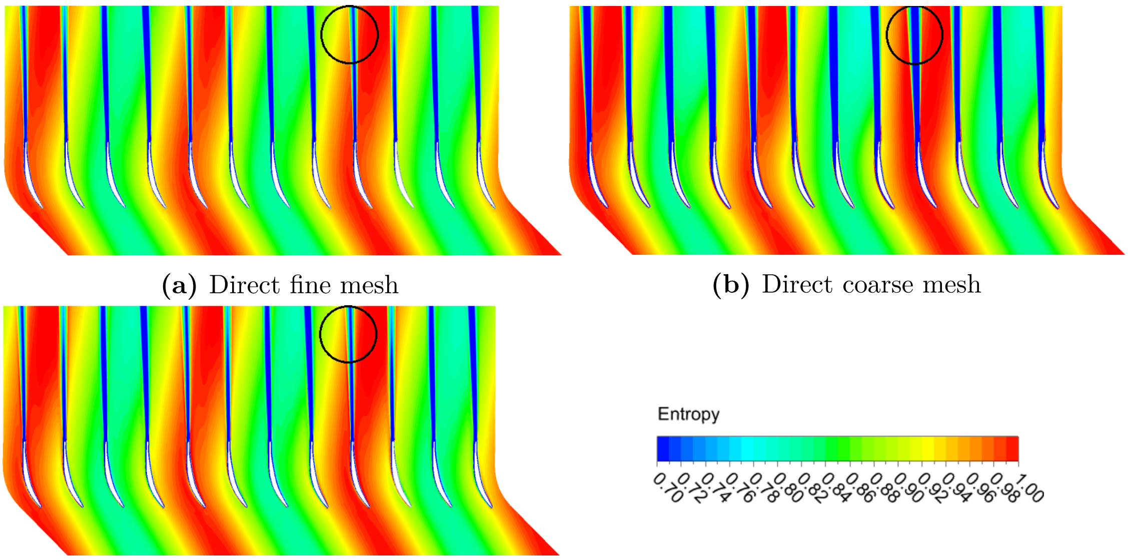

(a) Direct fine mesh

(b) Direct coarse mesh

(c) Fully-coupled multi-scale

Figure 8.14: Instantaneous entropy function $e^{-\Delta s/R}$ contour of different modeling fidelities for the randomly mistuned bladerow.

Figure 8.15 shows the comparison of the instantaneous static pressure distribution for different blades. Figure 8.15a presents the results for the blade subject to the minimum entropy wake (trough), while Figure 8.15b shows that for the blade immersed in the maximum entropy wake (peak). For both blades, the multi-scale method can be seen to be in excellent agreement with the direct fine mesh solution. The coarse mesh solution for Blade 2 over-predicts the size of bubble separation. On the other hand, the blade loading of Blade 4 significantly under-predicted by the coarse mesh simulation.

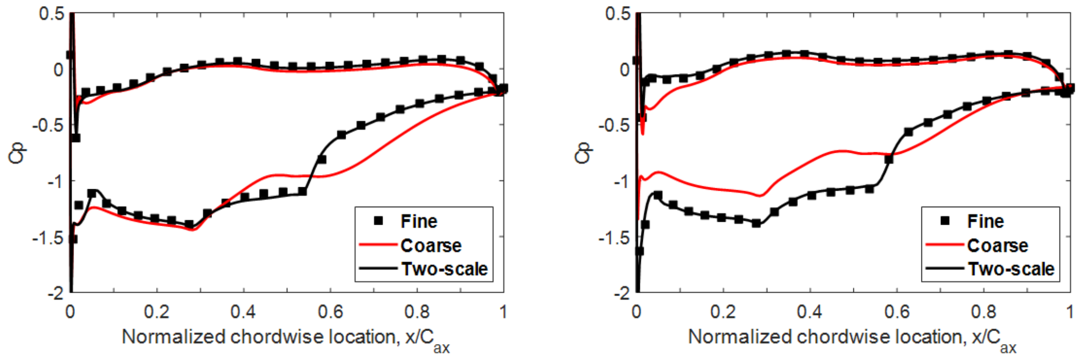

(a) Blade 2 – minimum entropy wake **(b)** Blade 4 – maximum entropy wake

Figure 8.15: Instantaneous blade static pressure distribution for the forced response of the randomly mistuned bladerow.

Figure 8.16 shows the instantaneous wake traverse at $x/C_{ax} = 1.7$. The peak entropy loss in the wake region is over-predicted by the coarse mesh simulation, while the fully-coupled multi-scale method are in excellent agreement with the fine mesh solution. This result supports the analysis of the wake mixing in the above discussion. This finding suggests that the fully-coupled multi-scale method is not only useful for aeroelastic but also for aerodynamic analyses, where the entropy loss is of interest to understand the loss mechanism [Denton, 2010].

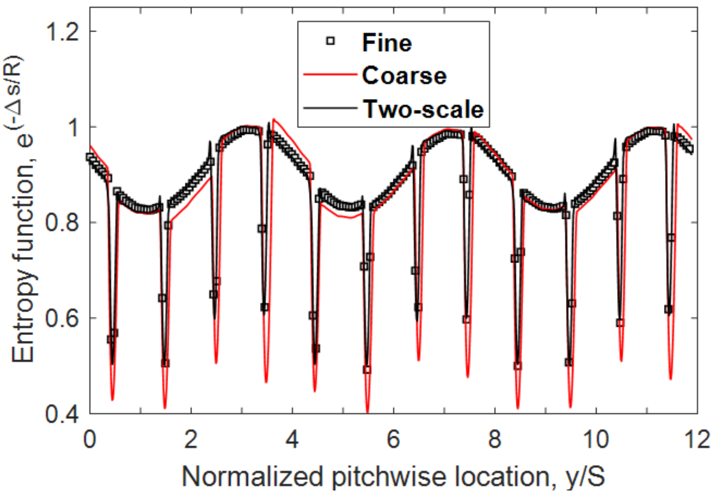

Figure 8.16: Entropy function $e^{-\Delta s/R})$ distribution at the wake traverse $x/C_{ax} = 1.7$.

8.6 Summary

In this chapter, a new method is developed and implemented to predict the aeroelastic performance of a mistuned bladerow using the fully-coupled method. The multi-scale approach is embedded in the fully-coupled simulation procedures, resulting in an efficient and accurate methodology. The validity and effectiveness of the method is examined through the case studies for a forced response bladerow. The new method has the following features:

1. Only a single unsteady forcing simulation with stationary blades and a single influence coefficient truncated-domain simulation (with only one blade vibrating) for a tuned bladerow, are required to generate the source terms.

2. The whole forced response characteristics for different frequencies, amplitudes, and mistuning patterns can then be simulated efficiently with the superimposed source terms.

3. The fluid-structure interaction effects are taken into account by the fully-coupled method.

The proposed method has been validated against the direct fully coupled fine mesh solutions in test cases including tuned, alternatingly mistuned, and randomly mistuned bladerows. It is shown that the present fully-coupled multi-scale method has a good accuracy both qualitatively and quantitatively compared to the direct baseline fine-mesh solutions, while being up to one order of magnitude faster. Although the pre-computed source terms are sampled at a particular frequency and amplitude, the procedure is shown to work effectively for a range of frequencies and amplitudes encountered during the frequency sweeping process. In addition, the new method is also shown to be able to capture the interactions between the inlet distortion and the blade vibration, although the source terms are determined in an uncoupled manner.

The forced response behaviour predicted by the present fully coupled approach shows that the frequency shift from the eigenfrequency at resonance depends on the amount of frequency mistuning. In addition, the alternating and random mistuning patterns examined in the present work are shown to amplify the forced response levels up to 20% and 50% respectively compared to that of a baseline tuned bladerow.

9
Conclusions

Contents

In this thesis, the effects of the structural mistuning and the aerodynamic mistuning on the aeroelastic performance of a bladerow have been investigated using the fully-coupled fluid-structure interaction simulation method. Especially, the thesis has contributed to the understanding of the interactions between the two types of mistuning, which has been lacking in the past literatures. An innovative design concept has been proposed by utilising the circumferential phasing between the structural mistuning and the aerodynamic mistuning to leverage the bladerow's aeroelastic performance. In order to make more frequent use of the high-fidelity simulations in early design and analysis of a mistuned bladerow, a new method has been developed and implemented in the commercial solver framework. The newly developed simulation methodology is built upon the multi-scale approach and the influence coefficient method. Various cases have been tested within this thesis and the results suggest the high accuracy and efficiency of the new method against the direct high-fidelity simulations.

9.1 Aeroelastic Effects of Structural and Aerodynamic Mistuning

The standalone structural mistuning always has a stabilising impact on the flutter stability. The degree of stabilisation strongly depends on the aeroelastic coupling and the strength of mistuning. The standalone aerodynamic mistuning has a non-monotonic trend on the flutter stability, i.e. it has a stabilising effect with a small amount of mistuning but a destabilising effect with a large amount of mistuning. There is no significant effect induced by different levels of the aeroelastic coupling for the standalone aerodynamic mistuned configurations. An aero-mistuning induced flutter phenomena has been reported, believed to be the first time. It has been shown that an aerodynamic mistuning can lead to flutter at a condition where the tuned cascade remains stable. The concurrent structural-aerodynamic mistuning shows a distinctive nonlinear interaction between the two types of mistuning. Particularly, the flutter stability of the unstable aero-mistuned cascade maybe improved with a small additional structural mistuning, but degraded remarkably with a larger value of additional structural mistuning.

For the forced response problems, both the structural mistuning and the aerodynamic mistuning induce vibration amplitude amplification compared to the tuned bladerow, at least for the test case and conditions investigated within the thesis. The aerodynamic mistuning has a significant effect on the response amplitudes, in contrast to previous understanding. The concurrent structural-aerodnamic mistuning shows remarkable interaction effects on the response amplitudes, particularly with different circumferential phasing between the two types of mistuning.

9.2 Structural-Aerodynamic Mistuning Circumferential Phasing Design Concept

Based on the fundamental understanding of the mistuned vibration mechanisms gained from high-fidelity fully-coupled simulations, an innovative design concept has been proposed with the potential to leverage the bladerow's aeroelastic performance. The proposed mistuning design concept introduces a new design variable, denoted as the mistuning circumferential phasing. It is essentially the relative phasing between the structural mistuning pattern and the aerodynamic mistuning pattern in the circumferential direction. The high-fidelity fully-coupled simulation methods are used to demonstrate its potential in improving the bladerow's aeroelastic performance. The results suggest that the new design concept can have significant impacts on both the flutter and forced response characteristics of a mistuned bladerow. The new mistuning design concept opens a new design space particularly in conjunction with certain intentional mistuning. The findings may also have some bearing in helping understand the inconclusiveness of previous observations related to the impact of mistuning, and thus help better understand this seemingly complex topic.

9.3 Multi-Scale Method For Mistuning Simulations

Although the fully-coupled fluid-structure simulation method is certainly useful for the design and analysis of the aeroelastic performance induced by mistuning, it is not often used due to expensive computational resource requirements. This thesis proposed a new simulation methodology that has the potential to reduce the simulation time by at least an order of magnitude while retaining the accuracy comparable to the high-fidelity simulations. The newly developed method is built upon the bases of the multi-scale approach and the influence coefficient method. This is the first time the theoretical framework of the multi-scale method has been extended to accommodate unsteady flow and grid deformation effects. The applications of the multi-scale method on aeroelasticity problems are also the first of its kind. In addition, it has been implemented in the popular commercial CFD solver (ANSYS CFX), which demonstrates its generality as well as the potential to be effectively replicated by a wider group of CFD/FSI modelling practitioners. On the other hand, the new extended formulation as well as the novel application of the influence coefficient method has been made in the thesis. Combining with the multi-scale approach, it provides an efficient way to pre-compute a limited high-fidelity simulations and later reconstruct the necessary source terms for a large amount of mistuned configurations.

The new simulation methodology has been tested for various aeroelasticity problems of interest. Starting from the steady and the unsteady flow simulations of uncoupled configurations, it has gradually built up to the fully-coupled fluid-structure interaction cases. For all test cases, the accuracy and the efficiency of the new simulation methodology have been compared against direct high-fidelity simulations. The results confirm the effectiveness of the new method.

9.4 Suggested Future Works

The following recommendations can be made for future studies:

9.4.1 Further Investigation of Response Amplitude Reduction by Mistuning

Although the conventional understanding is that mistuning would always increase the response amplitudes, some past literature suggests that mistuning could be able to reduce the response amplitudes. The test case configurations and conditions used in this thesis (e.g. Chapter 5) do not produce this peculiar behaviours. It would be of interest if the response amplitude reduction phenomena can be demonstrated using the high-fidelity fully-coupled simulation method to improve the understanding on this vibration mechanism.

Subsequently, it would be of interest to study the interactions between the structural mistuning and the aerodynamic mistuning for configurations that show this response amplitude reduction phenomenon.

9.4.2 Further Investigation on the Aeroelastic Effects of Aerodynamic Mistuning

In Chapter 5, a non-monotonic variation of aerodynamic damping with increasing aerodynamic mistuning strength has been observed. In addition, the aerodynamic mistuning induced flutter has been demonstrated. On the other hand, Stapelfeldt and Vahdati (2018) reported different trends of aerodynamic damping variation with mis-staggering. The trend depends on the operating point on the compressor map. In the present thesis, the operating condition does not experience stall. It would be of interest to investigate the aeroelastic effects of aerodynamic mistuning at different operating points (e.g. near-stall, near-choked, etc.) by traversing along the characteristic line.

9.4.3 Further Investigation of Mistuning Phasing

In Chapter 6, the structural mistuning and the aerodynamic mistuning are assumed to be separated and independent from each other. This can be regarded as a simplified situation for research purposes to investigate each effect independently. For a more practical application, a change in one structural/aerodynamic characteristic can affect another. For example, blades with different structural properties can end up with different running aerodynamic shapes and positions. As a result, it would be of interest to investigate the mutual interaction and dependency of the structural and the aerodynamic mistuning.

Another issue of interest lies in the applicability of the mistuning superposition method for cases with supposedly stronger nonlinearities such as shockwaves and flow separations. Further investigations into the effectiveness of the mistuning phasing would improve its robustness paving a way for practical applications.

9.4.4 Further Applications of the Multi-Scale Method on Challenging Flow Field

Chapters 7 and 8 in this thesis has demonstrated great potential of the multi-scale method for aeroelasticity modelling problems for the first time. To improve the confidence on its effectiveness, efficiency, and reliability, it needs to be applied to various challenging flow fields and continuously validated against the experiment and/or high-fidelity simulation results.

Appendices

A

Hilbert Transform-Based Approach for Spatial-Temporal Analysis

Contents

A.1 Fundamental of Hilbert Transform

The integral Hilbert transform (HT) of a time-domain signal $y\left(t\right)$, denoted as $\tilde{y}\left(t\right)$, is defined as:

$$\tilde{y}\left(t\right) \equiv \mathrm{HT}\left[y\left(t\right)\right] = -\frac{1}{\pi}\mathrm{P.V.}\int_{-\infty}^{\infty}\frac{y\left(\tau\right)}{\tau - t}d\tau \tag{A.1}$$

where HT is the Hilbert operator and P.V. is the Cauchy principal value. A complex analytic signal can be formed whose real part is the original signal and the imaginary part is the Hilbert transform of the real part:

$$Y\left(t\right) = y\left(t\right) + i \cdot \tilde{y}\left(t\right) \tag{A.2}$$

The analytic signal can be represented in a trigonometric or exponential form:

$$Y(t) = |Y(t)| [\cos\phi(t) + i \cdot \sin\phi(t)] = A(t) e^{i\phi(t)} \tag{A.3}$$

where $A(t)$ is the instantaneous amplitude

$$A(t) = \sqrt{y(t)^2 + \tilde{y}(t)^2} \tag{A.4}$$

and $\phi(t)$ is the instantaneous phase angle

$$\phi(t) = \arctan\frac{\tilde{y}(t)}{y(t)} \tag{A.5}$$

For a more complete review on the basic of the Hilbert transform and its use in mechanical vibration analyses, one is recommended to read the tutorial in Ref. [Feldman, 2011].

A.2 Hilbert Transform-Based Flutter Analysis

Starting from the equation of motion:

$$m\ddot{q} + c\dot{q} + kq = f \tag{A.6}$$

where m is modal mass, $c = \bar{c}e^{i\gamma_c}$ is modal damping, $k = \bar{k}e^{i\gamma_k}$ is modal stiffness, and f is modal aerodynamic damping force. Note that the mass and stiffness retains its dependency on time, which can account for nonlinear responses to the blade motion. Substituting the polar form of the mass and stiffness to the equation of motion yields:

$$m\ddot{q} + \bar{c}e^{i\gamma_c}\dot{q} + k\bar{k}e^{i\gamma_k}q = f \tag{A.7}$$

In order to make use of the Hilbert transform-based approach, each term in Equation A.7 is replaced by its HT analytic representation:

$$m\ddot{Q} + \bar{c}e^{i\gamma_c}\dot{Q} + \bar{k}e^{i\gamma_k}Q = F \tag{A.8}$$

where $Q(t) = q(t) + i \cdot [HT]|q(t)| = \hat{q}e^{i\omega t}$

$F(t) = f(t) + i \cdot [HT]|f(t)| = \hat{f}e^{i\phi(t)}$ Substituting Q and its derivatives to Equation A.8 yields:

$$-m\omega^2\hat{q} + \bar{c}i\omega\hat{q}\left(\cos\gamma_c + i\cdot\sin\gamma_c\right) + \bar{k}i\omega\hat{q}\left(\cos\gamma_k + i\cdot\sin\gamma_k\right) = \hat{f}e^{i\phi}e^{-i\omega t} = \hat{f}e^{i\psi} \tag{A.9}$$

where $\psi = \phi - \omega t$ Equating the imaginary part of Equation A.9 gives:

$$\bar{c}\omega\hat{q}\cos\left(\gamma_c\right) + \bar{k}\omega\hat{q}\cos\left(\gamma_k\right) = \bar{c_{eq}}\omega\hat{q} = \hat{f}\sin\psi \tag{A.10}$$

where $\bar{c_{eq}} = \bar{c}\cos\gamma_c + \bar{k}\sin\gamma_k/\omega$ is the equivalent viscous damping. It can be seen that the equivalent viscous damping contains both the real part (cosine term) of the damping term and the imaginary part (sine term) of the stiffness term. If the nonlinearity of the damping and stiffness terms is neglected, those terms will be constant and the equivalent viscous damping $\bar{c_{eq}} = c$.

From the equivalent viscous damping, the instantaneous damping work can be calculated as:

$$\begin{aligned} W_d(t) &= \bar{c_{eq}}\mathrm{Re}\left(\dot{Q}\right)^2 \\ &= \frac{\hat{f}\sin\psi}{\omega\hat{q}}\cdot\left[-\omega^2\hat{q}^2\cos\left(\omega t\right)^2\right] \\ &= -\hat{f}\omega\hat{q}\cdot\sin\psi\cdot\cos\left(\omega t\right)^2 \end{aligned}$$

The instantaneous damping can be calculated as:

$$\Xi(t) = \frac{W_d(t)}{\left(P_{01} - P2\right)\hat{q_{tip}}^2} \tag{A.11}$$

It can be seen that the instantaneous aerodynamic damping is time-dependent. The time-averaged damping can be found from any time interval:

$$\Xi_{avg} = \int_{t_1}^{t_2} \Xi(t)\,dt \tag{A.12}$$

For practical calculation of the aerodynamic damping, the amplitudes and phases can be calculated from the original signals and their respective HTs:

$$\begin{aligned} \hat{f} &= \sqrt{f^2 + \tilde{f}^2} \\ \hat{q} &= \sqrt{q^2 + \tilde{q}^2} \\ \psi &= \arctan\left(\frac{q\tilde{f} - \tilde{q}f}{qf + \tilde{q}\tilde{f}}\right) \end{aligned}$$

A.3 Comparison to the Conventional Uncoupled Energy Method

If the vibration is periodic as in the decoupled method, it can be shown that the Hilbert transform-based aerodynamic damping can be simplified to an expression consistent to the conventional energy method.

Because the vibration is periodic, the phase difference ψ between the blade response and the blade motion can be regarded as a constant. The cycle-averaged work done during the period T becomes:

$$\begin{aligned} W_d &= \int_t^{t+T} W_d\left(t\right) dt \\ &= \int_t^{t+T} \hat{f}\omega\hat{q} \cdot \sin\psi \cdot \cos\left(\omega t\right)^2 dt \end{aligned}$$

We also note that $\int_t^{t+T} \cos\left(\omega t\right)^2 dt = \pi/\omega$. The cycle-averaged work done becomes:

$$W_d = -\pi\hat{f}\hat{q}\sin\psi \tag{A.13}$$

The cycle-averaged aerodynamic damping can be calculated as below, which is consistent with the conventional energy method:

$$\begin{aligned} \Xi &= \frac{-\pi\hat{f}\hat{q} \cdot \sin\psi}{\left(P_{01} - P_2\right) \hat{q_{tip}}^2} \\ &= \frac{1}{C}\int_S \frac{-\pi\hat{p}\hat{q} \cdot \sin\psi ds}{\left(P_{01} - P_2\right) \hat{q_{tip}}^2} \end{aligned}$$

A.4 Application of the Hilbert Transform-Based Approach

The Hilbert transformed based analysis approach presented above is applied in the present thesis. A specific example of the approach is shown for the analysis of the random concurrent mistuned cascade in Figure [5.25b].

Figure A.1a shows the raw vibration histories obtained from the fully-coupled fluid-structure interaction simulation of the random concurrent mistuned cascade during roughly 200 vibration cycles. Figure A.1b shows the raw data of first 20 vibration cycles. It can be seen that only blade 1 starts initially with high kinetic energy. The energy then spreads out to other blades in the cascade. After several vibration cycles, a limit-cycle oscillatory behaviour is observed in blade 4 (also denoted as the most unstable blade). On the other hand, Figure A.2 shows the post-processed vibration signals using the Hilbert transform-based approach. The post-processed amplitude $\hat{q}$ in Figure A.2 is calculated as:

$$\hat{q} = \sqrt{q^2 + \tilde{q}^2} \tag{A.14}$$

Comparison between Figure A.1a and Figure A.2 shows that the post-processing method could help one to identify the oscillatory behaviours easier than the raw signal.

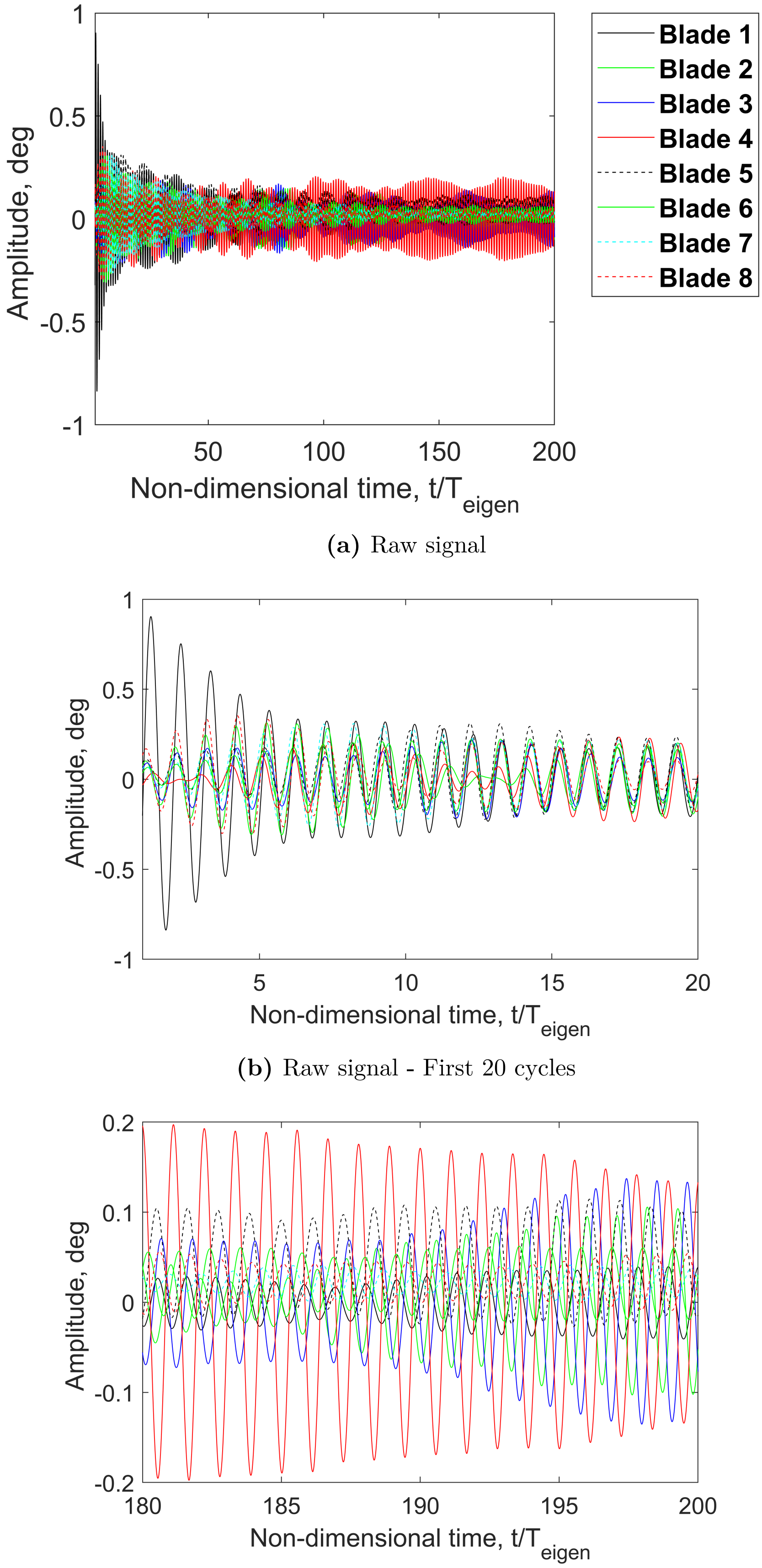

(a) Raw signal

(b) Raw signal - First 20 cycles

(c) Raw signal - Last 20 cycles

Figure A.1: Raw signal of the amplitude evolution of the random concurrent mistuned cascade.

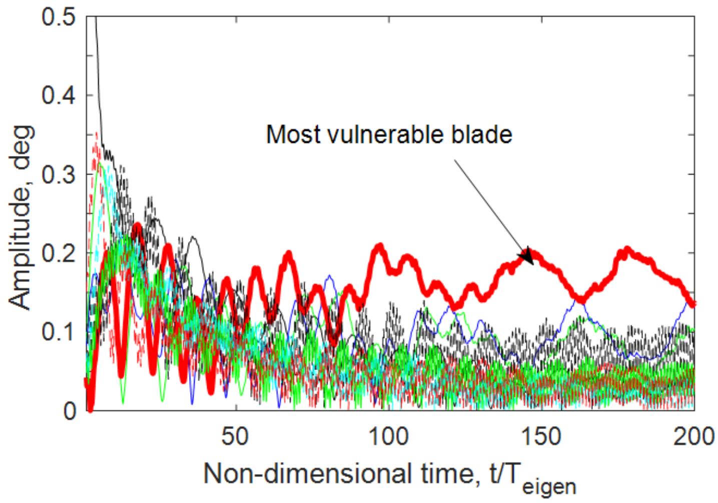

Figure A.2: Post-processed signal using the Hilbert transform based analysis of the amplitude evolution of the random concurrent mistuned cascade.

References

Barth, T., & Jespersen, D. (1989). The Design and Application of Upwind Schemes on Unstructured Meshes. *27th Aerospace Sciences Meeting*, AIAA 89–0366.

Beirow, B., Figaschewsky, F., Kühhorn, A., & Bornhorn, A. (2019). Vibration Analysis of an Axial Turbine Blisk with Optimized Intentional Mistuning Pattern. *Journal of Sound and Vibration*, *442*, 11–27.

Beirow, B., Kühhorn, A., Figaschewsky, F., Bornhorn, A., & Repetckii, O. V. (2019). Forced Response Reduction of a Blisk by Means of Intentional Mistuning. *Journal of Engineering for Gas Turbines and Power*, *141*(1), 011008.

Bell, D. L., & He, L. (2000). Three-Dimensional Unsteady Flow for an Oscillating Turbine Blade and the Influence of Tip Leakage. *Journal of Turbomachinery*, *122*(1), 93–101.

Bendiksen, O. O. (2000). Localization Phenomena in Structural Dynamics. *Chaos, Solitions and Fractals*, *11*(10), 1621–1660.

Besem, F. M., & Kielb, R. E. (2017). Influence of the Tip Clearance on a Compressor Blade Aerodynamic Damping. *Journal of Propulsion and Power*, *33*(1), 227–233.

Besem, F. M., Kielb, R. E., & Key, N. L. (2016). Forced Response Sensitivity of a Mistuned Rotor from an Embedded Compressor Stage. *Journal of Turbomachinery*, *138*(3), 031002.

Biesinger, T., Cornelius, C., Rube, C., Braune, A., Campregher, R., Godin, P. G., Schmid, G., & Zori, L. (2010). Unsteady CFD Methods in a Commercial Solver for Turbomachinery Applications. *Proceedings of the ASME Turbo Expo 2010: Power for Land, Sea, and Air. Volume 7: Turbomachinery, Parts A, B, and C*, GT2010–22762.

Bölcs, A., & Fransson, T. H. (1986). *Aeroelasticity in Turbomachines. Comparison of Theoretical and Experimental Cascade Results.* ECOLE POLYTECHNIQUE FEDERALE DE LAUSANNE (SWITZERLAND) LAB DE THERMIQUE APPLIQUEE.

Brandstetter, C., Duquesne, P., Paoletti, B., Aubert, S., & Ottavy, X. (2019). Project PHARE-2—A High-Speed UHBR Fan Test Facility for a New Open-Test Case. *Journal of Turbomachinery*, *141*(10), 101004.

Buchwald, P., Farahmand, A., & Vogt, D. M. (2019). On the Influence of Blade Aspect Ratio on Aerodynamic Damping. *Journal of Turbomachinery*, *141*(10), 101007.

Buffum, D. H., & Fleeter, S. (1990). Oscillating Cascade Aerodynamics by an Experimental Influence Coefficient Technique. *Journal of Propulsion and Power*, *6*(5), 612–620.

Burgos, M. A., Contreras, J., & Corral, R. (2011). Efficient Edge-Based Rotor/Stator Interaction Method. *AIAA Journal*, *49*(1), 19–31.

Camp, T. R., & Day, I. J. (1997). A Study of Spike and Modal Stall Phenomena in a Low-Speed Axial Compressor. *Proceedings of the ASME 1997 International Gas*

Turbine and Aeroengine Congress and Exhibition. Volume 1: Aircraft Engine; Marine; Turbomachinery; Microturbines and Small Turbomachinery, 97-GT–526.

Carstens, V., & Belz, J. (2001). Numerical Investigation of Nonlinear Fluid-Structure Interaction in Vibrating Compressor Blades. *Journal of Turbomachinery*, *123*(2), 402–408.

Carstens, V., Kemme, R., & Schmitt, S. (2003). Coupled Simulation of Flow-Structure Interaction in Turbomachinery. *Aerospace Science and Technology*, *7*(4), 298–306.

Carta, F. O. (1967). Coupled Blade-Disk-Shroud Flutter Instabilities in Turbojet Engine Rotors. *Journal of Engineering for Gas Turbines and Power*, *89*(3), 419–426.

Castanier, M. P., & Pierre, C. (2002). Using Intentional Mistuning in the Design of Turbomachinery Totors. *AIAA Journal*, *40*(10), 2077–2086.

Castanier, M. P., & Pierre, C. (2006). Modeling and Analysis of Mistuned Bladed Disk Vibration – Current Status and Emerging Directions. *Journal of Propulsion and Power*, *22*(2), 384–396.

Chahine, C., Verstraete, T., & He, L. (2019). A Comparative Study of Coupled and Decoupled Fan Flutter Prediction Methods Under Variation of Mass Ratio and Blade Stiffness. *Journal of Fluids and Structures*, *85*, 110–125.

Chen, T., Vasanthakumar, P., & He, L. (2001). Analysis of Unsteady Blade Row Interaction Using Nonlinear Harmonic Approach. *Journal of Propulsion and Power*, *17*(3), 651–658.

Chen, Y., Wu, H., Zhai, J., Chen, H., Zhu, Q., & Han, Q. (2019). Vibration Reduction of the Blisk by Damping Hard Coating and Its Intentional Mistuning Design. *Aerospace Science and Technology*, *84*, 1049–1058.

Choi, B. K., Lentz, J., Rivas-Guerra, A. J., & Mignolet, M. P. (2003). Optimization of Intentional Mistuning Patterns for the Reduction of the Forced Response Effects of Unintentional Mistuning: Formulation and Assessment. *Journal of Engineering for Gas Turbines and Power*, *125*(1), 131–140.

Connell, S., Braaten, M., Zori, L., Steed, R., Hutchinson, B., & Cox, G. (2011). A Comparison of Advanced Numerical Techniques to Model Transient Flow in Turbomachinery Blade Rows. *Proceedings of the ASME 2011 Turbo Expo: Turbine Technical Conference and Exposition. Volume 7: Turbomachinery, Parts A, B, and C*, GT2011–45820.

Connell, S., Hutchinson, B., Galpin, P., Campregher, R., & Godin, P. (2012). The Efficient Computation of Transient Flow in Turbine Blade Rows Using Transformation Methods. *Proceedings of the ASME Turbo Expo 2012: Turbine Technical Conference and Exposition. Volume 8: Turbomachinery, Parts A, B, and C*, GT2012–69019.

Corral, R., Beloki, J., Calza, P., & Elliott, R. (2019). Flutter Generation and Control Using Mistuning in a Turbine Rotating Rig. *AIAA Journal*, *57*(2), 782–795.

Corral, R., & Gallardo, J. M. (2014). Nonlinear Dynamics of Bladed Disks with Multiple Unstable Modes. *AIAA Journal*, *52*(6), 1124–1132.

Corral, R., Khemiri, O., & Martel, C. (2018). Design of Mistuning Patterns to Control the Vibration Amplitude of Unstable Rotor Blades. *Aerospace Science and Technology*, *80*, 20–28.

Crespo, J., Corral, R., & Pueblas, J. (2016). An Implicit Harmonic Balance Method in Graphics Processing Units for Oscillating Blade. *Journal of Turbomachinery*, *138*(3), 031001.

Cumpsty, N. A., Dong, Y., & Li, Y. S. (1995). Compressor Blade Boundary Layers in the Presence of Wakes. *Proceedings of the ASME 1995 International Gas Turbine and Aeroengine Congress and Exposition. Volume 1: Turbomachinery*, 95-GT–443.

Denton, J. D. (2010). Some Limitations of Turbomachinery CFD. *Proceedings of the ASME Turbo Expo 2010: Power for Land, Sea, and Air. Volume 7: Turbomachinery, Parts A, B, and C*, GT2010–22540.

Doi, H., & Alonso, J. J. (2002). Fluid/Structure Coupled Aeroelastic Computations for Transonic Flows in Turbomachinery. *Proceedings of the ASME Turbo Expo 2002: Power for Land, Sea, and Air. Volume 4: Turbo Expo 2002, Parts A and B*, GT2002–30313.

Dong, X., Zhang, Y., Zhang, Z., Lu, X., & Zhang, Y. (2020). Effect of Tip Clearance on the Aeroelastic Stability of a Wide-Chord Fan Rotor. *Journal of Engineering for Gas Turbines and Power*, *142*(9), 091010.

Dong, Y., & Cumpsty, N. A. (1990). Compressor Blade Boundary Layers: Part 2—Measurements With Incident Wakes. *Journal of Turbomachinery*, *112*(2), 231–240.

Duan, P. H., & He, L. (2020). Application of Multiscale Methodology for Transonic Turbine Blade Tip Cooling Design. *Journal of Turbomachinery*, *142*(8), 081011.

Ekici, K., Kielb, R. E., & Hall, K. C. (2010). Aerodynamic Assymetry Analysis of Unsteady Flows in Turbomachinery. *Journal of Turbomachinery*, *132*(1), 011006.

Ekici, K., Kielb, R. E., & Hall, K. C. (2013). The Effect of Aerodynamic Asymmetries on Turbomachinery Flutter. *Journal of Fluids and Structures*, *36*, 1–17.

Elazar, Y., & Shreeve, R. P. (1990). Viscous Flow in a Controlled Diffusion Compressor Cascade With Increasing Incidence. *Journal of Turbomachinery*, *112*(2), 256–265.

Epureanu, B. I., Hall, K. C., & Dowell, E. H. (2001). Reduced-Order Models of Unsteady Viscous Flows in Turbomachinery Using Viscous–Inviscid Coupling. *Journal of Fluids and Structures*, *15*(2), 255–273.

Erdos, J. I., Alzner, E., & McNally, W. (1977). Numerical Simulation of Periodic Transonic Flow Through a Fan Stage. *AIAA Journal*, *15*(11), 1559–1568.

Ewins, D. J. (1969). The Effects of Detuning Upon the Forced Vibrations of Bladed Disks. *Journal of Sound and Vibration*, *9*(1), 65–79.

Ewins, D. J., & Henry, R. (1987). *Structural Dynamic Characteristics of Individual Blades*. AGARD Manual on Aeroelasticity in Axial-Flow Turbomachines Volume 2: Structural Dynamics; Aeroelasticity.

Feiner, D. M., & Griffin, J. H. (2002). A Fundamental Model of Mistuning for a Single Family of Modes. *Journal of Turbomachinery*, *124*(4), 597–605.

Feldman, M. (2011). Hilbert Transform in Vibration Analysis. *Mechanical Systems and Signal Processing*, *25*(3), 735–802.

Fidalgo, V. J., Hall, C. A., & Colin, Y. (2012). A Study of Fan-Distortion Interaction Within the NASA Rotor 67 Transonic Stage. *Journal of Turbomachinery*, *134*(5), 051011.

Figaschewsky, F., Kühhorn, A., Beirow, B., Nipkau, J., Giersch, T., & Power, B. (2017). Design and Analysis of an Intentional Mistuning Experiment Reducing Flutter Susceptibility and Minimizing Forced Response of a Jet Engine Fan. *Proceedings of the ASME Turbo Expo 2017: Turbomachinery Technical Conference and Exposition. Volume 7B: Structures and Dynamics*, GT2017–64621.

Frey, C., Ashcroft, G., Kersken, H., & Voigt, C. (2014). A Harmonic Balance Technique for Multistage Turbomachinery Applications. *Proceedings of the ASME Turbo*

Expo 2014: Turbine Technical Conference and Exposition. Volume 2B: Turbomachinery, GT2014–25230.

Frey, C., & Kersken, H.-P. (2016). On the Regularisation of Non-Reflecting Boundary Conditions Near Acoustic Resonances. *ECCOMAS Congress 2016 VII European Congress on Computational Methods in Applied Sciences and Engineering.*

Fu, Z., Wang, Y., Jiang, X., & Wei, D. (2015). Tip Clearance Effects on Aero-Elastic Stability of Axial Compressor Blades. *Journal of Engineering for Gas Turbines and Power*, *137*(1), 012501.

Galpin, P. F., Broberg, R. B., & Hutchinson, B. R. (1995). Three-Dimensional Navier Stokes Predictions of Steady State Rotor/Stator Interaction With Pitch Change. *Proceedings of 3rd Annual Conference of the CFD Society of Canada*, 305–319.

Gan, J., Im, H., Espinal, D., Lefebvre, A., & Zha, G. (2014). Investigation of a Compressor Rotor Non-Synchronous Vibration With and Without Fluid-Structure Interaction. *Proceedings of the ASME Turbo Expo 2014: Turbine Technical Conference and Exposition. Volume 7B: Structures and Dynamics*, GT2014–26478.

Gan, J., Watanabe, T., & Himeno, T. (2022). Effect of Shock Wave Behavior on Unsteady Aerodynamic Characteristics of Oscillating Transonic Compressor Cascade. *Journal of Engineering for Gas Turbines and Power*, *144*(1), 011025.

Gao, J., Gao, Y., Yan, X., Jiang, J., Xu, K., & Sun, W. (2020). Damping Mistuning Effect of the Hard-Coating-Based Intentional Mistuning Techniques on Mistuned Blisks and Its Mechanism. *Aerospace Science and Technology*, *101*, 105848.

Gerolymos, G. A., Michon, G. J., & Neubauer, J. (2002). Analysis and Application of Chorochronic Periodicity in Turbomachinery Rotor/Stator Interaction Computations. *Journal of Propulsion and Power*, *18*(6), 1139–1152.

Giles, M. B. (1988). Calculation of Unsteady Wake/Rotor Interaction. *Journal of Propulsion and Power*, *4*(4), 356–362.

Giles, M. B. (1990). Stator/Rotor Interaction in a Transonic Turbine. *Journal of Propulsion and Power*, *6*(5), 621–627.

Hall, K. C., Thomas, J. P., & Clark, W. S. (2002). Computation of Unsteady Nonlinear Flows in Cascades Using a Harmonic Balance Technique. *AIAA Journal*, *40*(5), 879–886.

Halliwell, D. G., Newton, S. G., & Lit, K. S. (1984). A Study of Unsteady Pressures Near the Tip of a Transonic Fan in Unstalled Supersonic Flutter. *Journal of Vibration, Acoustics, Stress, and Reliability in Design*, *106*(2), 198–203.

Halstead, D. E., Wisler, D. C., Okiishi, T. H., Walker, G. J., Hodson, H. P., & Shin, H. (1997). Boundary Layer Development in Axial Compressors and Turbines: Part 2 of 4—Compressors. *Journal of Turbomachinery*, *119*(3), 426–444.

Han, Y., Murthy, R., Mignolet, M. P., & Lentz, J. (2014). Optimization of Intentional Mistuning Patterns for the Mitigation of the Effects of Random Mistuning. *Journal of Engineering for Gas Turbines and Power*, *136*(6), 062505.

Hanamura, Y., Tanaka, H., & Yamaguchi, K. (1980). A Simplified Method to Measure Unsteady Forces Acting on the Vibrating Blades in Cascade. *Bulletin of JSME*, *23*(180), 880–887.

Hayford, R. K., & Ford, S. J. (2020). *Mistuned concentric airfoil assembly and method of mistuning same* (US 10,767,486 B2). https://patents.google.com/patent/US10767486B2

He, L. (1990). An Euler Solution for Unsteady Flows Around Oscillating Blades. *Journal of Turbomachinery*, *112*(4), 714–722.

He, L. (1992). Method of Simulating Unsteady Turbomachinery Flows with Multiple Perturbations. *AIAA Journal*, *30*(11), 2730–2735.

He, L. (1994). Integration of 2-D Fluid/Structure Coupled System for Calculations of Turbomachinery Aerodynamic/Aeroelastic Instabilities. *International Journal of Computational Fluid Dynamics*, *3*(3-4), 217–231.

He, L. (1998a). Unsteady Flow in Oscillating Turbine Cascades: Part 1—Linear Cascade Experiment. *Journal of Turbomachinery*, *120*(2), 262–268.

He, L. (1998b). Unsteady Flow in Oscillating Turbine Cascades: Part 2—Computational Study. *Journal of Turbomachinery*, *120*(2), 269–275.

He, L. (2010). Fourier methods for turbomachinery applications. *Progress in Aerospace Sciences*, *46*(8), 329–341.

He, L. (2013a). Block-Spectral Mapping for Multi-Scale Solution. *Journal of Computational Physics*, *250*, 13–26.

He, L. (2013b). Fourier Spectral Modelling for Multi-Scale Aero-Thermal Analysis. *International Journal of Computational Fluid Dynamics*, *27*(2), 118–129.

He, L. (2018). Multiscale Block Spectral Solution for Unsteady Flows. *International Journal for Numerical Methods in Fluids*, *86*(10), 655–678.

He, L., & Ning, W. (1998). Efficient Approach for Analysis of Unsteady Viscous Flows in Turbomachines. *AIAA Journal*, *36*(11), 2005–2012.

He, L., & Yi, J. (2017). Two-Scale Methodology for URANS/Large Eddy Simulation Solutions of Unsteady Turbomachinery Flows. *Journal of Turbomachinery*, *139*(10), 101012.

He, Z., Epureanu, B. I., & Pierre, C. (2007). Fluid-Structural Coupling Effects on the Dynamics of Mistuned Bladed Disks. *AIAA Journal*, *45*(3), 552–561.

Hoyniak, D., & Fleeter, S. (1986). The Effect of Circumferential Aerodynamic Detuning on Coupled Bending-Torsion Unstalled Supersonic Flutter. *Journal of Turbomachinery*, *108*(2), 253–260.

Huang, X. Q., He, L., & Bell, D. L. (2008). Effects of Tip Clearance on Aerodynamic Damping in a Linear Turbine Cascade. *Journal of Propulsion and Power*, *24*(1), 26–33.

Huang, X. Q., He, L., & Bell, D. L. (2009). Experimental and Computational Study of Oscillating Turbine Cascade and Influence of Part-Span Shrouds. *Journal of Fluids Engineering*, *131*(5), 051102.

Hurty, W. C. (1965). Dynamic Analysis of Structural Systems Using Component Modes. *AIAA Journal*, *3*(4), 678–685.

Im, H., & Zha, G. (2012). Simulation of Non-Synchronous Blade Vibration of an Axial Compressor Using a Fully Coupled Fluid/Structure Interaction. *Proceedings of the ASME Turbo Expo 2012: Turbine Technical Conference and Exposition. Volume 7: Structures and Dynamics, Parts A and B*, GT2012–68150.

Irretier, H. (1983). *Spectral Analysis of Mistuned Bladed Disk Assemblies by Component Mode Synthesis*. Vibrations of Bladed Disk Assemblies.

Kamakoti, R., & Shyy, W. (2004). Fluid–Structure Interaction for Aeroelastic Applications. *Progress in Aerospace Sciences*, *40*(8), 535–558.

Kapsis, M., He, L., Li, Y. S., Valero, O., Wells, R. G., Krishnababu, S., Gupta, G., Kapat, J., & Schaenzer, M. (2020). Multiscale Parallelized Computational Fluid

Dynamics Modeling Toward Resolving Manufacturable Roughness. *Journal of Engineering for Gas Turbines and Power*, *142*(2), 021001.

Kaza, K. R. V., & Kielb, R. E. (1982). Flutter and Forced Response of a Mistuned Cascade in Incompressible Flow. *AIAA Journal*, *20*(8), 1120–1127.

Kelly, F., Heikurinen, K., Fazari, E., & Wu, Y. (2010). *Intentionally mistuned integrally bladed rotor* (US 2010/0247310 A1). https://patents.google.com/patent/US20100247310

Lane, F. (1956). System Mode Shapes in the Flutter of Compressor Blade Rows. *Journal of the Aeronautical Sciences*, *23*(1), 54–66.

Launder, B. E., & Spalding, D. B. (1983). *Numerical Prediction of Flow, Heat Transfer, Turbulence and Combustion* (pp. 96–116). Pergamon.

Lee, S. Y., Castanier, M., & Pierre, C. (2005). Assessment of Probabilistic Methods for Mistuned Bladed Disk Vibration. *46th AIAA/ASME/ASCE/AHS/ASC Structures, Structural Dynamics and Materials Conference*, AIAA 2005–1990.

Leng, Y., & Key, N. L. (2020). Effects of Nonuniform Blade Spacing on Compressor Rotor Forced Response and Aeroacoustics. *Journal of Propulsion and Power*, *36*(5), 721–731.

Leng, Y., & Key, N. L. (2021). Effects of Nonuniform Blade Spacing on Compressor Rotor Flutter Stability. *Journal of Propulsion and Power*, *37*(5), 682–692.

Lim, S. H., Bladh, R., Castanier, M. P., & Pierre, C. (2007). Compact, Generalized Component ModeMistuning Representation For Modeling Bladed Disk Vibration. *AIAA Journal*, *45*(9), 2285–2298.

Lu, Y., Green, J., Stapelfeldt, S. C., & Vahdati, M. (2019). Effect of Geometric Variability on Running Shape and Performance of a Transonic Fan. *Journal of Turbomachinery*, *141*(10), 101012.

Ma, H., Jin, C., & Wei, W. (2017). Experimental Investigation of Effects of Suction Side Squealer Tip on The Aeroelastic Stability of a Linear Oscillating Compressor Cascade. *Proceedings of the Institution of Mechanical Engineers, Part G: Journal of Aerospace Engineering*, *231*(11), 2120–2131.

Malzacher, L., Schwarze, C., Motta, V., & Peitsch, D. (2019). Experimental Investigation of an Aerodynamically Mistuned Oscillating Compressor Cascade. *Journal of Turbomachinery*, *141*(7), 071012.

Marshall, J. G., & Imregun, M. (1996). A Review of Aeroelasticity Methods with Emphasis on Turbomachinery Applications. *Journal of Fluids and Structures*, *10*(3), 237–267.

Martel, C., & Sanchez-Alvarez, J. J. (2018). Intentional Mistuning Effect in the Forced Response of Rotors with Aerodynamic Damping. *Journal of Sound and Vibration*, *433*, 212–229.

Mayorca, M. A., De Andrade, J. A., Vogt, D. M., Mårtensson, H., & Fransson, T. H. (2011). Effect of Scaling of Blade Row Sectors on the Prediction of Aerodynamic Forcing in a Highly Loaded Transonic Compressor Stage. *Journal of Turbomachinery*, *133*(2), 021013.

McMullen, M. S., & Jameson, A. (2006). The Computational Efficiency of Non-Linear Frequency Domain Methods. *Journal of Computational Physics*, *212*(2), 637–661.

Menter, F. R., Langtry, R. B., Likki, S. R., Suzen, Y. B., Huang, P. G., & Völker, S. (2004). A Correlation-Based Transition Model Using Local Variables—Part I: Model Formulation. *Journal of Turbomachinery*, *128*(3), 413–422.

Miyakozawa, T., Kielb, R. E., & Hall, K. C. (2009). The Effects of Aerodynamic Asymmetric Perturbations on Forced Response of Bladed Disks. *Journal of Turbomachinery*, *131*(4), 041008.

Moffatt, S., & He, L. (2005). On Decoupled and Fully-Coupled Methods for Blade Forced Response Prediction. *Journal of Fluids and Structures*, *20*(2), 217–234.

Moffatt, S., Ning, W., Li, Y., Wells, R. G., & He, L. (2005). Blade Forced Response Prediction for Industrial Gas Turbines. *Journal of Propulsion and Power*, *21*(4), 707–714.

Mueller, T. R., Vogt, D. M., Fischer, M., & Phillipsen, B. A. (2021). On the Far-Field Boundary Condition Treatment in the Framework of Aeromechanical Computations Using ANSYS CFX. *Proceedings of the Institution of Mechanical Engineers, Part A: Journal of Power and Energy*, *235*(5), 1103–1118.

Ning, W., & He, L. (2001). Some Modeling Issues on Trailing-Edge Vortex Shedding. *AIAA Journal*, *39*(5), 787–793.

Ottarsson, G. S. (1994). *Dynamic modeling and vibration analysis of mistuned bladed disks* (Doctoral dissertation). University of Michigan. United States.

Petrov, E. P. (2010). A Method for Forced Response Analysis of Mistuned Bladed Disks with Aerodynamic Effects Included. *Journal of Engineering for Gas Turbines and Power*, *132*(6), 062502.

Petrov, E. P. (2011). Reduction of Forced Response Levels for Bladed Disks by Mistuning: Overview of the Phenomenon. *Journal of Engineering for Gas Turbines and Power*, *133*(7), 072501.

Phan, H. M. (2021). A Spatial-Temporal Analysis Approach for Flutter Predictions Using Decoupled and Fully-Coupled Methods. *Journal of Fluids and Structures*, *107*, 103412.

Phan, H. M., & He, L. (2018). Validation Study of 3D Oscillating Compressor Cascade. *Proceedings of the 15th International Symposium on Unsteady Aerodynamics, Aeroacoustics & Aeroelasticity of Turbomachines*, ISUAAAT15–027.

Phan, H. M., & He, L. (2019). Validation Studies of Linear Oscillating Compressor Cascade and Use of Influence Coefficient Method. *Proceedings of the ASME Turbo Expo 2019: Turbomachinery Technical Conference and Exposition. Volume 7A: Structures and Dynamics*, GT2019–90941.

Phan, H. M., & He, L. (2020a). Efficient Steady and Unsteady Flow Modeling for Arbitrarily Mis-Staggered Bladerow Under Influence of Inlet Distortion. *Proceedings of the ASME Turbo Expo 2020: Turbomachinery Technical Conference and Exposition. Volume 10A: Structures and Dynamics*, GT2020–16204.

Phan, H. M., & He, L. (2020b). Validation Studies of Linear Oscillating Compressor Cascade and Use of Influence Coefficient Method. *Journal of Turbomachinery*, *142*(5), 051005.

Phan, H. M., & He, L. (2021a). Analysis Of Structurally and Aerodynamically Mistuned Oscillating Bladerow Using Fully-Coupled Method. *Proceedings of Global Power and Propulsion Society*, GPPS-TC-2021–330.

Phan, H. M., & He, L. (2021b). Efficient Steady and Unsteady Flow Modeling for Arbitrarily Mis-Staggered Bladerow Under Influence of Inlet Distortion. *Journal of Engineering for Gas Turbines and Power*, *143*(7), 071009.

Phan, H. M., & He, L. (2021c). Investigation of Mistuned Oscillating Cascade Using Fully-Coupled Method. *Proceedings of the ASME Turbo Expo 2021: Turbomachinery Technical Conference and Exposition. Volume 9A: Structures and*

Dynamics — Aerodynamics Excitation and Damping; Bearing and Seal Dynamics; Emerging Methods in Design and Engineering, GT2021–59124.

Phan, H. M., & He, L. (2022). Investigation of Structurally and Aerodynamically Mistuned Oscillating Cascade Using Fully Coupled Method. *Journal of Engineering for Gas Turbines and Power*, *144*(3), 031009.

Plourde, G. A., & Stenning, A. H. (1968). Attenuation of Circumferential Inlet Distortion in Multistage Axial Compressors. *Journal of Aircraft*, *5*(3), 236–242.

Provenza, A. J., Duffy, K. P., & Bakhle, M. A. (2019). Aeromechanical Response of a Distortion-Tolerant Boundary Layer Ingesting Fan. *Journal of Engineering for Gas Turbines and Power*, *141*(1), 011011.

Rendu, Q., Aubert, S., & Ferrand, P. (2020). Numerical Identification of Mechanisms Triggering 2D Choke Flutter in Transonic Fan. *Journal of Fluids and Structures*, *97*, 102879.

Sadeghi, M., & Liu, F. (2005). Computation of Cascade Flutter by Uncoupled and Coupled Methods. *International Journal of Computational Fluid Dynamics*, *19*(8), 559–569.

Sadeghi, M., & Liu, F. (2007). Investigation of Mistuning Effects on Cascade Flutter Using a Coupled Method. *Journal of Propulsion and Power*, *23*(2), 266–272.

Salles, L., & Vahdati, M. (2016). Comparison of Two Numerical Algorithms for Computing the Effects of Mistuning of Fan Flutter. *Proceedings of the ASME Turbo Expo 2016: Turbomachinery Technical Conference and Exposition. Volume 7B: Structures and Dynamics*, GT2016–57324.

Schmitt, S., Nürnberger, D., & Carstens, V. (2003). Evaluation of the Principle of Aerodynamic Superposition in Forced Response Calculations. *Tenth International Symposium on Unsteady Aerodynamics and Aeroelasticity of Turbomachines Symposium*, 133–144.

Schoenenborn, H. (2017). *Array of flow-directing elements for a gas turbine compressor* (US 9,835,166 B2). https://patents.google.com/patent/US9835166B2

Shadmani, M., Tikani, R., & Ziaei-Rad, S. (2019). On Using a Distributed-Parameter Model for Modal Analysis of a Mistuned Bladed Disk Rotor and Extracting the Statistical Properties of Its In-Plane Natural Frequencies. *Journal of Sound and Vibration*, *438*, 324–343.

Sicot, F., Dufour, G., & Gourdain, N. (2011). A Time-Domain Harmonic Balance Method for Rotor/Stator Interactions. *Journal of Turbomachinery*, *134*(1), 011001.

Sisto, F. (1987). *Introduction and Overview.* AGARD Manual on Aeroelasticity in Axial-Flow Turbomachines Volume 1: Unsteady Turbomachinery Aerodynamics.

Sjolander, S. A. (1997). *Secondary and Tip-Clearance Flows in Axial Turbines.* VKI Lecture Series 1.

Sladojevic, I., Petrov, E. P., Imregun, M., & Sayma, A. I. (2006). Forced Response Variation of Aerodynamically and Structurally Mistuned Turbo-Machinery Rotors. *Proceedings of the ASME Turbo Expo 2006: Power for Land, Sea, and Air. Volume 5: Marine; Microturbines and Small Turbomachinery; Oil and Gas Applications; Structures and Dynamics, Parts A and B*, GT2006–90948.

Sladojevic, I., Sayma, A. I., & Imregun, M. (2007). Influence of Stagger Angle Variation on Aerodynamic Damping and Frequency Shifts. *Proceedings of the ASME Turbo Expo 2007: Power for Land, Sea, and Air. Volume 5: Turbo Expo 2007*, GT2007–28166.

Srinivasan, A. V. (1997). Flutter and Resonant Vibration Characteristics of Engine Blades. *Journal of Engineering for Gas Turbines and Power*, *119*(4), 742–775.

Stapelfeldt, S., & Brandstetter, C. (2021). Suppression of Nonsynchronous Vibration Through Intentional Aerodynamic and Structural Mistuning. *Journal of Turbomachinery*, *144*(2), 021008.

Stapelfeldt, S., & Vahdati, M. (2018). On the Importance of Engine-Representative Models for Fan Flutter Predictions. *Journal of Turbomachinery*, *140*(8), 081005.

Stapelfeldt, S. C., & Di Mare, L. (2015). Reduced Passage Method for Multirow Forced Response Computations. *AIAA Journal*, *53*(10), 3049–3062.

Stapelfeldt, S. C., Parry, A. B., & Vahdati, M. (2016). Investigation of Flutter Mechanisms of a Contra-Rotating Open Rotor. *Journal of Turbomachinery*, *138*(5), 051009.

Stargardter, H. (1977). Optical Determination of Rotating Fan Blade Deflections. *Journal of Engineering for Power*, *99*(2), 204–209.

Storer, J. A., & Cumpsty, N. A. (1991). Tip Leakage Flow in Axial Compressors. *Journal of Turbomachinery*, *113*(2), 252–259.

Tian, S., Petrie-Repar, P., Glodic, N., & Sun, T. (2019). CFD-Aided Design of a Transonic Aeroelastic Compressor Rig. *Journal of Turbomachinery*, *141*(10), 101003.

Tran, D. M., Liauzun, C., & Labaste, C. (2003). Methods of Fluid–Structure Coupling in Frequency and Time Domains Using Linearized Aerodynamics for Turbomachinery. *Journal of Fluids and Structures*, *17*(8), 1161–1180.

Vahdati, M., Simpson, G., & Imregun, M. (2011). Mechanisms for Wide-Chord Fan Blade Flutter. *Journal of Turbomachinery*, *133*(4), 041029.

Vargiu, P., Firrone, C. M., Zucca, S., & Gola, M. M. (2011). A Reduced Order Model Based on Sector Mistuning for the Dynamic Analysis of Mistuned Bladed Disks. *International Journal of Mechanical Sciences*, *53*(8), 639–646.

Vilmin, S., Lorrain, E., Hirsch, C., & Swoboda, M. (2006). Unsteady Flow Modeling Across the Rotor/Stator Interface Using the Nonlinear Harmonic Method. *Proceedings of the ASME Turbo Expo 2006: Power for Land, Sea, and Air. Volume 6: Turbomachinery, Parts A and B*, GT2006–90210.

Vogt, D. M., & Fransson, T. H. (2007). Experimental Investigation of Mode Shape Sensitivity of an Oscillating Low-Pressure Turbine Cascade at Design and Off-Design Conditions. *Journal of Engineering for Gas Turbines and Power*, *129*(2), 530–541.

Wang, D., & Huang, X. (2017). A Complete Rotor–Stator Coupling Method for Frequency Domain Analysis of Turbomachinery Unsteady Flow. *Aerospace Science and Technology*, *70*, 367–377.

Watanabe, T., Azuma, T., Uzawa, S., Himeno, T., & Inoue, C. (2018). Unsteady Pressure Measurement on Oscillating Blade in Transonic Flow Using Fast-Response Pressure-Sensitive Paint. *Journal of Turbomachinery*, *140*(6), 061003.

Whitehead, D. S. (1966). Effect of Mistuning on the Vibration of Turbo-machine Blades Induced by Wakes. *Journal of Mechanical Engineering Science*, *8*(1), 15–21.

Whitehead, D. S. (1987). *Classical Two-Dimensional Methods.* AGARD Manual on Aeroelasticity in Axial-Flow Turbomachines.

Willcox, K., & Peraire, J. (2002). Application of Reduced-Order Aerodynamic Modeling to the Analysis of Structural Uncertainty in Bladed Disks. *Proceedings of the*

ASME Turbo Expo 2002: Power for Land, Sea, and Air. Volume 5: Turbo Expo 2002, Parts A and B, GT2002–30680.

Williams, R., Gregory-Smith, D., He, L., & Ingram, G. (2010). Experiments and Computations on Large Tip Clearance Effects in a Linear Cascade. *Journal of Turbomachinery*, *132*(2), 021018.

Wilson, M. J., Imregun, M., & Sayma, A. I. (2007). The Effect of Stagger Variability in Gas Turbine Fan Assemblies. *Journal of Turbomachinery*, *129*(2), 404–411.

Yang, H. (2004). *3d unsteady flow in oscillating compressor cascade* (Doctoral dissertation). Durham University. United Kingdom.

Yang, H., & He, L. (2004). Experimental Study on Linear Compressor Cascade With Three-Dimensional Blade Oscillation. *Journal of Propulsion and Power*, *20*(1), 180–188.

Yao, G., J., E., S., & Wadia, A. R. (2010). High-Fidelity Numerical Analysis of Per-Rev-Type Inlet Distortion Transfer in Multistage Fans – Part I: Simulations with Selected Blade Rows. *Journal of Turbomachinery*, *132*(4), 041014.

Yuan, J., Allegri, G., Scarpa, F., Rajasekaran, R., & Patsias, S. (2015). Novel Parametric Reduced Order Model for Aeroengine Blade Dynamics. *Mechanical Systems and Signal Processing*, *62*, 235–25.

Yuan, J., Scarpa, F., Titurus, B., Allegri, G., Patsias, S., & Rajasekaran, R. (2017). Novel Frame Model for Mistuning Analysis of Bladed Disk Systems. *Journal of Vibration and Acoustics*, *139*(3), 031016.

Zhai, Y., Bladh, R., & Dyverfeldt, G. (2012). Aeroelastic Stability Assessment of an Industrial Compressor Blade Including Mistuning Effects. *Journal of Turbomachinery*, *134*(6), 060903.

Zhang, Q., He, L., & Rawlinson, A. (2014). Effects of Inlet Turbulence and End-Wall Boundary Layer on Aerothermal Performance of a Transonic Turbine Blade Tip. *Journal of Engineering for Gas Turbines and Power*, *136*(5), 052603.